Development of a magneto-optical trap for CaF molecules

Moritz Hambach

submitted in partial fulfilment of the requirements
for the degree of Doctor of Philosophy in Physics

Centre for Cold Matter, Department of Physics
Imperial College London

October 2017

Imperial College
London

Declaration

I hereby declare that this thesis is my own work. Wherever the work of others is used, the sources are appropriately referenced and acknowledged.

Abstract

Laser cooling and trapping in a magneto-optical trap (MOT) have been essential to the success of cold atom physics in the last decades. Recently, the application of the same techniques to molecules has begun. The complexity of even a simple diatomic molecule makes laser cooling difficult, but promises new applications in many areas of research.

In this thesis I describe the development of the first three-dimensional MOT of calcium fluoride (CaF) molecules. First, a cryogenic buffer gas source was set up, producing a pulsed beam of $(9.3 \pm 0.5) \times 10^{10}$ molecules per steradian per pulse with forward velocities around 170 m/s. A similar source for very large molecules was set up during a 5 month internship at the University of Vienna. Next, the molecular pulse was slowed down to the capture velocity of a MOT using chirped laser slowing, resulting in about 7×10^5 CaF molecules passing through the typical MOT volume of 1 cm^3 at velocities of 15 ± 5 m/s. A new deceleration method, called Zeeman-Sisyphus deceleration, was also investigated. In this method molecules move through a spatially varying magnetic field and are optically pumped between low- and high-field seeking states in such as a way that they are always losing kinetic energy. The method promises to deliver more slow molecules because the molecules are guided transversely as they are decelerated. A small prototype was built and the optical pumping step was tested successfully.

Finally, $(7.6 \pm 0.5) \times 10^3$ CaF molecules were trapped in a MOT and cooled to a temperature of 8.5 ± 1.0 mK. The radial trap frequency is $\omega_\rho = 2\pi \times (130 \pm 7)$ Hz and the damping constant is $\beta = (9.5 \pm 1.2) \times 10^2$ s^{-1}. The lifetime is about 100 ms and depends strongly on the scattering rate. This MOT is an an ideal starting point for a wide range of new experiments with ultracold molecules.

Citations to previously published work

Parts of this thesis have been or soon will be published in the following articles:

- S. Truppe, H. J. Williams, N. J. Fitch, M. Hambach, T.E. Wall, E. A. Hinds, B. E. Sauer and M. R. Tarbutt. An intense, cold, velocity-controlled molecular beam by frequency-chirped laser slowing. *New Journal of Physics* **19**, 022001 (2017).

- S. Truppe, H. Williams, M. Hambach, L. Caldwell, N. J. Fitch, E. A. Hinds, B. E. Sauer and M. R. Tarbutt. Molecules Cooled below the Doppler Limit. Accepted for publication in *Nature Physics*. arXiv:1703.00580

- H. Williams, S. Truppe, M. Hambach, L. Caldwell, N. J. Fitch, E. A. Hinds, B. E. Sauer and M. R. Tarbutt. Characteristics of a magneto-optical trap of molecules. Accepted for publication in *New Journal of Physics*. arXiv:1706.07848

- S. Truppe, M. Hambach, S. M. Skoff, N. E. Bulleid, J. S. Bumby, R. J. Hendricks, E. A. Hinds, B. E. Sauer, M. R. Tarbutt. A buffer gas beam source for short, intense and slow molecular pulses. Accepted for publication in *Journal of Modern Optics*. arXiv:1707.06291

Acknowledgements

Three years is a long time and there are a lot of people that have helped me during this PhD. First of all I would like to thank my supervisors, Ben and Mike. Thanks for giving me the opportunity of working on such an exciting experiment, and for all the support. Thanks Ben for your patience and help in the lab. Special thanks goes to Mike for correcting my thesis, I learned a lot from this, and from the weekly meetings.

A big thanks goes to the mechanical workshop. Jon, Steve and Gio, we couldn't have built this experiment without you. Thanks to Val for the electronics support. I would also like to thank the administration, Sanja, Judith and Marcia, for helping organise everything with a smile on the face. Thanks Doug, for mentoring your sheeple.

Thanks to the CaF team: Stefan, Hannah, Noah, Thom and Anne. I learned a lot from my postdocs, especially Stefan, and the mix of ambitious drive and perseverance when things don't work as planned was perfect. Cheers to our neighbours in bay three, Jack and Izzie, for always being helpful. I'll miss the whole group: the frisbee sessions, friday pub nights and 5-a-side football (defend the title, Noah!).

Thanks to my friends, at uni and outside of it, for making this time in London so enjoyable. Thanks, Haidee, for the patience with me writing day and night.

Finally I want to thank my family for supporting me during my PhD, like they always have.

"What do we mean by understanding something? We can imagine that this complicated array of moving things which constitutes the world is something like a great chess game being played by the gods, and we are observers of the game. We do not know what the rules of the game are; all we are allowed to do is to watch the playing. Of course, if we watch long enough, we may eventually catch on to a few of the rules. The rules of the game are what we mean by fundamental physics. Even if we knew every rule, however, we might not be able to understand why a particular move is made in the game, merely because it is too complicated and our minds are limited (...). We must, therefore, limit ourselves to the more basic question of the rules of the game. If we know the rules, we consider that we understand the world."

Richard Feynman

Contents

List of Figures

List of Tables

Chapter 1

Introduction

This PhD thesis describes the cooling and trapping of molecules with laser light. In this chapter I will motivate my research and give an overview over the various approaches to cool molecules down to the milikelvin (mK) regime, and their limitations.

1.1 Motivation: Applications of ultracold molecules

The challenge of trapping large numbers of polar molecules and cooling them to the mK regime and below has received more and more attention in the last decades. Because of their rotational and vibrational degrees of freedom, molecules possess a rich internal structure which can't be found in atoms. Unfortunately this complexity makes it harder to find a closed transition[1] for the laser cooling technique.
An important feature of polar molecules is their strong permanent dipole moment on the order of a few Debye, which makes them sensitive to their environment (e.g. external electric fields, dipole-dipole interactions with other molecules). This opens possibilities for new applications, some of which will be discussed here.

1.1.1 Quantum Information

It has been proposed to use the orientation of the dipole moment of trapped single molecules as bits in a quantum computer [1]. Here, the long range dipole-dipole

[1] A closed transition is one where there are no losses (e.g. spontaneous decays) into levels that are not addressed by lasers.

interactions would provide a coupling between quantum bits, which is necessary to perform multi-qubit operations. Achieving similarly strong interactions between atoms usually requires exciting them to high lying Rydberg states. A two-qubit quantum gate was demonstrated using Rydberg atoms [2]. Ions on the other hand show strong interactions via the Coulomb force and multi-qubit quantum gates have been demonstrated [3], but scaling up the number of trapped ions is a great challenge. Molecules combine the scalability of atomic systems with a built-in long range interaction, which makes them a promising candidate for quantum computation.

1.1.2 Quantum Simulation

Another field that would benefit from ultracold molecules is quantum many body physics. The interaction of molecules placed in traps and manipulated by light fields is believed to give rise to new quantum phase transitions and could be used to simulate solid state systems. For example, dipolar bosons in an optical lattice are predicted to show the checkerboard, collapse or supersolid phases in addition to the usual Mott insulator and superfluid phases that are known from atoms [4]. Loading these traps usually requires molecules at microkelvin (μK) temperatures, which could be provided by a molecule MOT, possibly with additional evaporative or sympathetic cooling steps [5, 6].

1.1.3 High precision tests of fundamental physics

A very interesting application is precision measurements to test fundamental physics. There exist theories predicting the dependence of "constants", like the fine structure constant α, on time or density of mass. Comparing spectroscopic measurements of molecular transitions in the lab with those from telescopes looking at light from stars far away (hence emitted long time ago), it is possible to put constraints on these variations $\Delta\alpha/\alpha$ [7, 8]. Tests done entirely in the laboratory over the course of a few years can also constrain these theories, if the measurements are precise enough, and for this it is best to use ultracold molecules.

Another application is the measurement of the electron's electric dipole moment, realized (among others) in our group at Imperial College [9]. The experiment relies

on a Ramsey-type interferometer using Ytterbium Fluoride (YbF) molecules from a supersonic beam. The precision of the measurement is proportional to the free evolution time of the interferometer. It has been proposed to use a "fountain" of laser cooled YbF molecules being accelerated upwards out of an optical molasses [10]. This could increase the free evolution time from milliseconds to seconds, leading to an improvement of three orders of magnitude in precision.

1.1.4 Ultracold chemistry

Finally, the quantum properties of ultracold molecules could be used for ultracold chemistry [11]. Since chemical reactions depend on collisions between the reaction partners, cooling the particles can change chemical reaction rates and allow precise control over a reaction. First of all, cooling a particle from thermal to ultracold temperatures (< 1 mK) increases its de Broglie wavelength $\lambda_{DB} = h/\sqrt{2\pi m k_B T}$ by many orders of magnitude, so that it can become larger than the size of the molecule. In this case we expect quantum behaviour to play a role in the collision, for example quantum mechanical tunnelling through energy barriers [12].
Another effect observed in ultracold collisions is related to the *centrifugal barrier*, which is an energy barrier due to the long-range repulsive centrifugal potential $V_c(R) = \frac{l(l+1)}{2\mu R^2}$. Here μ is the reduced mass and l is the total angular momentum of the two particles. Since l is conserved in a collision of two particles, the process can be separated into different contributions of the conserved angular momentum, called partial waves and labelled as *s-wave, p-wave* etc.. In a thermal gas, the kinetic energies of the particles are much larger than the centrifugal barrier, so a lot of partial waves contribute to the scattering process. At ultracold temperatures however, the kinetic energy can be insufficient to overcome the centrifugal barrier of even a single unit of angular momentum. In this case the collision will be dominated entirely by the s-wave behaviour, which can lead to the suppression of inelastic collisions [6].

1.2 Methods to produce cold molecules

There are two different approaches for producing cold molecules. One could either start with hot molecules and cool them down (here called the *direct method*), or one

starts by cooling atoms, usually in a magneto-optical trap, which are then combined into a cold molecule.

1.2.1 Assembly from cold atoms

The main methods for assembly of molecules from cold atoms are photo-association [13, 14] and magneto-association via Feshbach resonances [15, 16]. Both techniques have the disadvantage of producing weakly bound molecules in highly excited vibrational states close to the dissociation threshold. The population transfer to a lower lying state by a STIRAP [17] (stimulated Raman adiabatic passage) process has been demonstrated on several molecules, including KRb[18], RbCs[19], NaK[20], NaRb[21] and NaLi[22]. The results are summarised in table 1.1. In the case of KRb, more than 10^4 ground state molecules at 350 nK translational temperature were produced with a peak density of $10^{12}/\mathrm{cm}^3$ [23]. Nevertheless, the overall complexity of the production chain calls for a simpler solution. Another drawback is that this method can only produce molecules that consist of atoms that can be laser cooled (mostly alkali atoms).

1.2.2 Direct cooling methods

Supersonic expansion

There are several approaches to directly produce cold molecules. A common method is the supersonic beam, where a gas expands from a high pressure container into low pressure environment through a small aperture [24]. In this process the particle collisions convert the thermal energy of the molecules into forward motion, leading to a beam of low translational temperature (typically a few Kelvin), but high velocity (typically 300-1200 m/s). The vibrational and rotational temperatures of the molecules are reduced by collisions as well, which can be further enhanced by injecting the molecules into an atomic gas beam [25].

Buffer gas cooling

Another approach is to extract kinetic energy by collisions with a different particle species that is already cold. The buffer gas beam source, pioneered by Doyle *et al*

[26], is the most prominent example of this and will be explained in detail in chapter 3. Here the species of interest thermalises with a buffer gas, usually He at 4 K, and can then be extracted as a cold and slow molecular beam (typically 100-150 m/s) with high beam intensities. This technique is applicable to a wide range of molecules but limited in the final temperature it can reach. It is often used as a starting point for cold molecule experiments.

Electro-optical cooling

Another interesting approach is optoelectrical cooling [27], which is based on a vibrational decay in a Sisyphus scheme in an electric trapping field. It is limited by slow vibrational decay rates, but applicable to a wide range of molecules and has produced molecules at sub-milikelvin temperatures [28].

Sympathetic cooling with cold atoms

Once they are confined in a trap, molecules could be cooled down to temperatures below 1 mK using sympathetic cooling with laser cooled atoms [6]. This method uses collisions between atoms and molecules, similar to the buffer gas method, but benefits from the well known techniques to cool down atoms such as Rubidium to sub-milikelvin temperatures. The challenge here is that inelastic collisions can change the internal state of the molecule from a weak-field seeking to a strong-field seeking state, which would no longer be trapped in a static electric or magnetic trap. An alternative approach, which is also pursued in our group at Imperial College, is the use of a microwave trap [29]. Here molecules can be trapped in their strong-field seeking ground state, while the energy of collisions is typically too small to excite them into a non-trapped weak-field seeking state.

Evaporation cooling

As a last step, trapped molecules could be cooled by evaporation, a method well studied in the cold atom community that has been recently applied to molecules [5]. It works by removing only the hottest particles from the trap, usually via radio frequency waves, so that after re-thermalisation the temperature of the remaining

Method	Molecule	T (μK)	N	n (cm^{-3})	ρ
Feshbach resonance + STIRAP	KRb [18]	0.35	3×10^4	1×10^{12}	2×10^{-2}
	RbCs [19]	0.24	1×10^2		
	NaK [20]	0.5	5×10^3	2.5×10^{11}	7.7×10^{-3}
	NaRb [21]	0.72	8×10^3	$> 10^{11}$	$> 7.7 \times 10^{-4}$
	NaLi [22]	3	3×10^4	5×10^{10}	3×10^{-18}
Photo-association	RbCs [30]	100			
	KRb [31]	130	1×10^3	1×10^6	2.6×10^{-12}
	NaCs [32]	300			
	LiCs [33]	260			
	YbRb [34]	450			
	LiRb [35]				
rf MOT	SrF[36]	750	6×10^3	3×10^5	6×10^{-14}
dc MOT + gray molasses	CaF [37]	52	1.8×10^4	1.1×10^5	3.4×10^{-12}
Electro-optical cooling	H_2CO [28]	420	3×10^5	3×10^6	1×10^{-11}
Evaporative cooling (mag. trap)	OH [38]	5000	10^6	5×10^{10}	3×10^{-10}

Table 1.1: Summary of trapping and cooling methods for polar molecules and their results, including temperature T, molecule number N and peak number density n, at the highest observed phase-space density ρ.

ensemble is reduced. The loss of molecules means that it requires a reasonably high number of trapped molecules to begin with, but if this is provided it can increase the phase space density substantially.

Conclusion

All the presented methods have their limitations. We believe that laser cooling and trapping, possibly in combination with a Zeeman-Sisyphus decelerator (see chapter 6.3), is the most promising route to large dense samples of ultracold molecules, just like the magneto-optical trap is the usual starting point for ultracold atomic physics. Table 1.1 summarises the highest phase space densities of the discussed methods, including laser cooling in a magneto-optical trap (MOT), which will be explained in detail in the next section.

1.3 Laser cooling

In the following sections I will give a summary of the principle of the laser cooling technique and how it has been applied to atoms and molecules.

1.3.1 The principle

In the photon picture, light is interpreted as particles with an associated momentum $\vec{p}_{\mathrm{ph}} = \hbar\vec{k}$, where $\hbar = h/2\pi$ is the reduced Planck constant and $\vec{k}$ denotes the wave vector. When an atom or a molecule with initial momentum $\vec{p}_{\mathrm{i}}$ absorbs a photon, its momentum is changed to $\vec{p}_{\mathrm{f}} = \vec{p}_{\mathrm{i}} + \vec{p}_{\mathrm{ph}}$, which either increases or decreases its velocity depending on the relative direction of wave vector and particle motion. Maximum slowing occurs when photon and particle counter-propagate, while co-propagating photons accelerate the particle. The absorption of a photon is followed by its spontaneous emission[2], but since the emission happens in a random direction, on average this doesn't change the particle's momentum.

In order to cool a gas of particles, which are equally likely to move in any direction, we need to have them absorb more counter-propagating than co-propagating photons. This can be done using the Doppler effect, which states that the frequency of a wave is shifted to higher values when an object is moving towards the emitter and shifted to lower values when it moves away from it. If now the frequency of the laser is chosen lower than an atomic resonance ("red detuned"), particles counter-propagating to the laser beam will be Doppler-shifted back in resonance, which leads to an increased absorption probability. Co-propagating particles will instead be shifted further out of resonance and experience reduced radiative pressure. The velocity dependent net force can be used to create a so called 3D optical molasses of ultracold particles by overlapping counter-propagating laser beams in all three dimensions of space.

It is crucial for laser cooling experiments to have a (quasi) closed cycle of absorption and spontaneous emission (see figure 1.1), meaning that there are no decay channels to states that are not addressed by light fields. For example, a molecule like CaF with a mass of 59 amu (atomic mass units) at a velocity of 100 m/s needs to absorb about 10^4 photons of wavelength $\lambda \approx 600$ nm to be brought to rest. In reality, zero velocity is never reached due to heating by the recoil of the isotropic spontaneous emission that follows each absorption. Instead, the cooling is limited by the so called Doppler limit $T_{\mathrm{D}} = \hbar\Gamma/2k_{\mathrm{B}}$ of typically several hundred μK. There are however sub-

[2] absorption can also be followed by stimulated emission, but for a single laser this cycle has no net effect on the momentum

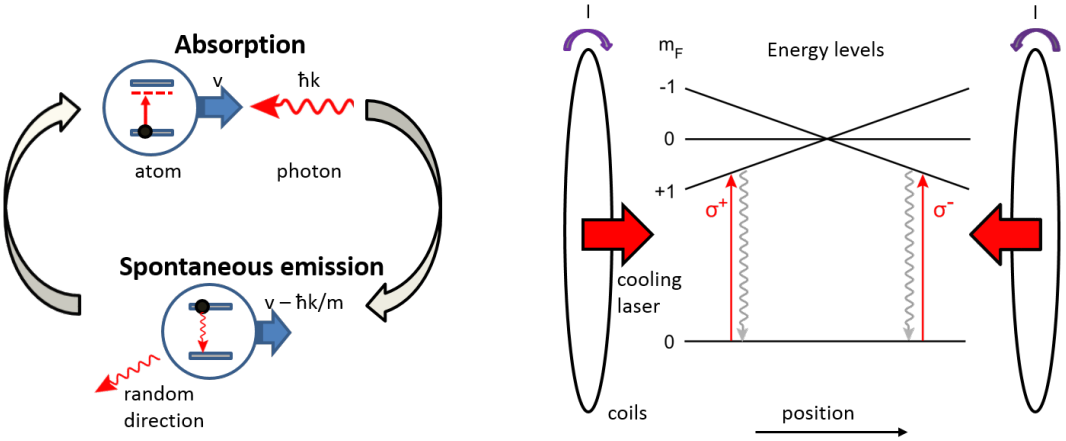

Figure 1.1: Left: Depiction of the laser cooling cycle of absorption and spontaneous emission of photons (see text). Right: Scheme for a magneto-optical trap (see text).

Doppler methods like the polarisation gradient cooling to reach temperatures even below T_{D} [39]. Rather than by the Doppler temperature, the cooling limit in this case is given by the recoil temperature $T_{\mathrm{R}} = \hbar^2 k^2 / 2 M k_{\mathrm{B}}$ with the atomic mass M.

So far the described forces are only velocity-dependent and not position-dependent, hence do not trap the particles. Actual trapping in space can be achieved by adding a magnetic quadrupole field to the molasses setup and choosing the laser beams to be circularly polarized (see figure 1.1). The magnetic field induces a position dependent Zeeman shift in the different magnetic sublevels while the opposing circular polarization of counter-propagating beams can be chosen so that the atom is always more likely to absorb a photon that pushes it towards the center of the trap. For example, for a particle in the ground state ($m_F = 0$) at positive position, the $m_F = -1$ excited level will be closer to resonance, which means it is more likely to absorb a photon of the counter-propagating σ^- laser field (see figure 1.1). At negative z-values the $m_F = 1$ excited state will be tuned into resonance with the σ^+ light. This results in a net force towards the center of the trap where the B-field is zero. This so called magneto-optical trap (MOT) is nowadays a standard setup in many atomic physics labs around the world and a starting point of more complex research activities.

1.3.2 Laser cooling atoms

As explained in the last section, laser cooling requires a repeated cycle of absorption and spontaneous emission, which is why a suitable atom should have a (practically) closed transition. This can easily be found in alkali atoms (e.g. Rb, Na, Cs) by driving the transition from the upper hyperfine level F' of the ground state to the $F'' = F' + 1$ level of the first excited state. Due to selection rule $\Delta F = 0, \pm 1$, the atom can only decay back to its initial state, where it will be excited by the cooling laser again. In experiments there is usually a small probability of exciting the $F'' = F'$ state, from which the atom can decay to the lower hyperfine level of the ground state and would be lost. This is solved by applying a *repump* laser, which optically pumps these populations back into the cooling cycle.

The first observation of radiation pressure on matter dates back to 1933, where an atomic beam of sodium was deflected by resonant light from a simple lamp [40]. With the first tunable quasi-monochromatic dye lasers becoming available in the 70's, in 1975 Haensch and Shawlow came up with the idea of laser cooling atomic vapour in free space [41], while Wineland and Dehmelt proposed similar methods for trapped ions. Since ions could be trapped in space by electric fields, they were easier to observe and manipulate. Hence, laser cooling was first demonstrated on Mg^{2+} ions in a Penning trap in 1978 [42], but three years later Andreev *et al.* achieved longitudinal cooling and slowing of a beam of sodium atoms as well [43].

In the 80's the research activities intensified. It was shown that atomic beams could be slowed down even further when the laser was kept in resonance with the atoms by chirping the laser frequency [44] or Zeeman-shifting the atomic energy levels by applying magnetic field gradients [45]. Both methods compensate for the decreasing Doppler-shift when the atom's velocity is reduced.

In 1985, the first three-dimensional optical molasses was achieved with sodium atoms [46]. It immediately reached a temperature of 240 μK, which corresponds to the Doppler temperature of the chosen species. Only later it was found that there is a second cooling effect in a molasses due to polarisation gradients, which allows reaching even lower temperatures [39].

After successfully cooling atoms, the only thing missing was a way to efficiently

trap them in space. There were different approaches using the induced electric or magnetic dipole moments to trap the atoms in local field extrema [47, 48], but they suffered from weak confinement strengths and therefore limited lifetimes due to background gas collisions. Finally, Dave Pritchard from MIT and Steve Chu from Stanford demonstrated the first magneto-optical trap in an experimental setup at Bell labs, following an idea of Jean Dalibard. In their 1987 paper they reported trapping sodium atoms for 2 minutes at a density of $10^{11}\mathrm{cm}^{-3}$ and temperatures below 1 mK at a trap depth of 400 mK [49]. The scheme was robust and insensitive to small changes in laser frequency, polarisation purity or magnetic field strength. It is still used nowadays in many research groups and can be combined with other techniques like evaporative cooling to reach temperatures in the nanokelvin regime [50]. In 1997, Steven Chu, Claude Cohen-Tannoudji and William D. Phillips were awarded the Nobel prize in physics "for development of methods to cool and trap atoms with laser light".

1.3.3 Laser cooling molecules

For a long time it was thought to be too technically challenging to apply laser cooling to molecules, the reason being the complex energy level structure of even a simple diatomic molecule due to its rotational and vibrational degrees of freedom. The decay into one of these sublevels, which are dark to the cooling laser, will exempt it from further cooling unless optically pumped back into the cycle.

In 2004 DiRosa described necessary requirements for molecules to reduce leaking into states not addressed by the cooling laser and suggested suitable candidate molecules [51]. The critical property here is the Franck-Condon factor (FCF) q_{ij}, which is the square of the overlap integral of two vibrational molecular wave functions. In an electric dipole transition it describes the probability amplitude of a transition from vibrational state i to vibrational state j. A high value q_{00} would allow a large number of photon absorptions and re-emissions before a decay to another vibrational level occurs. For example, a molecule with $q_{00} = 0.99$ would on average cycle $N = 1/(1 - q_{00}) = 100$ times between the vibrational ground states before decaying to a vibrational excited state. Some molecules show FCFs above 95% (see chapter 2.2). It is therefore feasible to get quasi closed vibrational transitions by adding just

one or two repump lasers addressing the lowest vibrational levels.

In order to prevent the losses into rotational sublevels, it was proposed to use the $(N' = 1 \rightarrow N'' = 0)$ transition [52], where N' and N'' are the rotational quantum numbers of the ground state and first excited state respectively. In their 2008 paper, Stuhl *et al.* pointed out that the selection rule $\Delta J = 0, \pm 1$ for the total angular momentum $\hat{J} = \hat{N} + \hat{S}$ would allow only the decay back to the $N' = 1$ ground state. For simplicity they proposed using molecules with net nuclear spin $I = 0$, which would avoid a hyperfine structure, where each level would have to be addressed by lasers separately. Of course this criteria constrains the choice of molecule a lot. Later experiments included hyperfine levels as well, since they can be addressed by creating radio frequency sidebands on a single laser using modulators.

In the same paper, the problem of dark states in this kind of transition was discussed. Dark states are states that can not be addressed by the chosen laser polarization. They are inevitable for the case $J' > J''$, since the ground states with $|m_{J'}| = J'$ will always be dark to one of the circular polarizations. Additionally there can exist coherent dark states, which are the coherent superposition of two bright states. Molecules in a dark state will not be repumped and are lost from the cooling process. In a MOT setup this could make the molecules interact with just one of the two counter-propagating beams, possibly prohibiting trapping (see chapter 1.3.4). Dark states can be made bright again by applying magnetic fields at a certain angle to the laser polarization. The magnetic field induces a Larmor precession of the spins, remixing the populations of the magnetic sublevels.

The first demonstration of radiation pressure on a molecular beam was reported by Shuman *et al.* in 2009 [53]. Using the techniques suggested by Stuhl *et al.*, they managed to scatter about 150 photons from each SrF molecule, leading to a deflection of 1 mm corresponding to a transverse velocity of 5.6 mm/s. They used the $X^2\Sigma^+(N = 1, \nu = 0) \rightarrow A^2\Pi_{1/2}(\nu = 0)$ transition (excited state lifetime $\tau = 24$ ns) with only one vibrational repump laser for the $(\nu = 1 \rightarrow 0)$-transition. SrF has very favourable Franck-Condon factors with $q_{00} = 98.1\%$. Both cooling and repump lasers were electro-optically modulated to produce RF sidebands and address all four hyperfine levels. Dark states were remixed by applying a magnetic field of $B = 7$G at an angle $0 < \theta < 90°$, corresponding to a Larmor frequency of a few MHz. The

experiment can be seen as a milestone in laser cooling molecules.

The same group continued working on SrF and achieved the first one dimensional transverse laser cooling of a molecular beam only one year later [54]. Now adding a second vibrational repump laser, they were able to observe both Doppler cooling and transverse Sisyphus cooling effects. By retro-reflecting the cooling light along the beam path, they were able to increase the interaction time substantially and scatter about 1000 photons per molecule, reducing the transverse temperature from 5 mK to less than 1 mK. As a source they used a cryogenic buffer gas cell, similar to the one we use (see chapter 3.1).

Later the group also demonstrated longitudinal slowing, decelerating a SrF beam from 140 m/s to 50 m/s, corresponding to 10^4 scattered photons per molecule [55]. Unfortunately the slowing led to transverse heating and increased divergence of the beam, decreasing the molecular beam flux to only 6 % of its initial value.

Today there are at least six groups working on laser cooling of different molecules: The Ye group at JILA (YO), the DeMille group at Yale (SrF), the Doyle group at Harvard (CaF, SrOH), the Hoekstra group at the University of Groeningen (SrF), the Zelevinsky group at the University of Columbia (BaH), and us. Our group at Imperial College London achieved the first longitudinal slowing and cooling of a supersonic CaF beam [56]. With only one repump laser and estimated 1000-2000 scattering events per molecule, the forward velocity could be reduced by 17 m/s. When the cooling laser was kept in resonance by chirping the frequency, the slowing effect was doubled. The translational temperature was reduced from 3 K to 330 mK. The cooling occurs due to the higher Doppler shift of faster molecules, which brings them closer to resonance with the light field, leading to increased slowing. There are other molecular species investigated for laser cooling at our group including YbF and BH [57, 58].

1.3.4 Magneto-optical trapping of molecules

If laser cooling of some molecules is possible, one could think that a three-dimensional magneto-optical trap should be straightforward. Unfortunately, this is not the case. The rotationally closed transition ($N' = 1 \rightarrow N'' = 0$) has lower angular momen-

tum in the excited state than in the ground state. This means that there are dark states in the system. Atomic MOTs operating on such transitions have been produced previously [59]. They are called Type-II MOTs and they have far weaker confining forces due to the presence of the dark states[3]. The problem here is that a particle can be in a state that is dark to the counter-propagating and bright to the co-propagating laser, which results in an anti-confining force. If no remixing of the states occurs, on average each absorption of a confining photon must be followed by the absorption of a photon that is anti-confining, leading to no net trapping force. It is however possible that the standard quadrupole magnetic field of a MOT provides the necessary remixing effects.

In 2013 the group of Jun Ye presented a solution to remix the dark states [60]. They were able to demonstrate a two-dimensional MOT of YO molecules by constantly switching the laser polarizations from σ^+ to σ^- with a pockels cell and simultaneously changing the magnetic field direction to preserve the trapping force. As result they observed 2D transverse cooling from 25 mK down to 2 mK. The switching frequency had to be of the order of the excited state decay rate (a few MHz). It should be mentioned that remixing dark states in YO by magnetic fields instead of polarization swapping was not an option since one of the ground state hyperfine levels has $F = 1$ but a Lande factor of $g = 0$, which means its 3 sublevels ($m_F = 0, \pm 1$) can not be remixed by an external magnetic field. This is not the case for SrF or CaF.

In 2014 the first three dimensional MOT of SrF molecules was observed [61]. In this experiment the dark state issue is not given particular treatment, and is explained as being solved "due to Larmor precession in the quadrupole magnetic field and due to optical pumping as molecules move through the complicated optical polarization gradients arising from the orthogonal pairs of circularly-polarized laser beams". Because of weak confining forces with a trap depth of only 10 mK , compared to a few K of atomic MOTs, the 2.5 mK cold molecules were trapped for only 56 ms, with molecule numbers of only about 400. Nevertheless this presented an important step for the goal of a reliable source of dense ultracold molecule samples. The trap was subsequently improved [62] after a proposal to change the polarisation of the

[3] for more details on the MOT forces see section 8.1

trapping light [63] (see chapter 8.1). Another improvement up to 10^4 molecules at sub-milikelvin temperatures [64, 36] was possible by switching the magnetic fields and polarisations at MHz rates, as done in the Ye group before. These molecule numbers are still at least 4 orders of magnitude smaller than what is routinely achievable in atomic MOTs, which is mostly attributed to the challenge of slowing lots of molecules down to the capture velocity of the trap. This thesis describes the production of the first CaF MOT, describes the methods we use to increase the number of slow molecules available to be captured in the MOT, and discusses how this could be increased further.

1.4 Thesis overview

This thesis describes the long way from an initially fast ($\sim$ 600 m/s) beam of CaF molecules to the final goal of a 3-dimensional magneto-optical trap.

Chapter 2 gives some necessary background on the molecule of choice, CaF, and its most important properties.
Chapter 3 provides a basic theoretical explanation of the Buffer gas method, which allowed us to replace the fast supersonic source of CaF with a much slower one, and then describes our source setup and results.
Chapter 4 is somewhat independent from the rest: It presents work done in Markus Arndt's group in Vienna, during a 5 month secondment, focussing on buffer gas sources of large molecules for interferometry.
Chapter 5 presents the optical setup and the lasers needed for further slowing and trapping of the CaF beam.
Chapter 6 shows how we successfully slow down the molecules, and introduces a new method called Zeeman-Sisyphus deceleration.
Chapter 7 describes the MOT chamber and detection setup.
Chapter 8 finally demonstrates the first magneto-optical trapping of CaF molecules, and characterises the most important properties of it.
Chapter 9 summarises the results and shows a glimpse into future experiments.

1.5 Contributions of the author

Complex experiments like ours require teamwork to be successful. The work in the lab was mainly done by three people: my PhD colleague Hannah Williams, the postdoctoral researcher Stefan Truppe and myself. My main contributions were:

- developing the cold buffer gas source (together with Stefan).
- initial laser development (cooled ECDL and injection locking). The final optical table setup was designed by Stefan and built by all three of us.
- setting up the MOT chamber and blackening it.
- setting up the detection, testing and improving its sensitivity.
- testing the Zeeman decelerator (which was designed and built by Noah Fitch) in our CaF beam, and analysing the results.
- setting up the buffer gas source for biomolecules in Vienna (together with PhD student Ugur Sezer).

I was less involved in the chirp slowing experiments, which is why they are described only briefly here. The final push for the first MOT and the initial characterisation measurements were done by all three of us.

Chapter 2

The CaF molecule

2.1 Basic theory of diatomic molecules

In this chapter I will give a short summary of the interactions inside a diatomic molecule, elaborate how they lead to the various contributions to the complex energy level scheme, and explain the usual notation of the states.

2.1.1 Born-Oppenheimer approximation

The complete description of a diatomic molecule consisting of two nuclei A and B and N electrons requires solving the time-independent Schroedinger equation, which turns out to be very complicated. It can however be well described using the Born-Oppenheimer approximation. The derivation presented here follows [65], but can be found in most molecular physics textbooks.

First of all we are only interested in the motion of nuclei and electrons relative to the center of mass, not the motion of the center of mass itself. We therefore introduce the relative coordinate $\vec{R} = \vec{R}_A - \vec{R}_B$ and the center of mass coordinate $\vec{R}_{CM} = \frac{m_A\vec{R}_A + m_B\vec{R}_B}{m_A+m_B}$ with the positions $\vec{R}_A$ and $\vec{R}_B$ of the nuclei in the lab frame and the electron positions $\vec{r_i}$. The total Hamiltonian consists of the kinetic energy T_N of the nuclei, the kinetic energy T_e of the electrons and the Coulomb interaction $V = \frac{Z_A Z_B e^2}{4\pi\epsilon_0 R} - \frac{e^2}{4\pi\epsilon_0}\sum_{i=1}^{N}(\frac{Z_A}{|\vec{r_i}-\vec{R_A}|} + \frac{Z_B}{|\vec{r_i}-\vec{R_B}|}) - \frac{e^2}{4\pi\epsilon_0}\sum_{i<j=1}^{N}\frac{1}{|\vec{r_i}-\vec{r_j}|}$,

$$H = T_N + T_e + V\,. \tag{2.1}$$

The time-independent Schroedinger equation then reads

$$H\,\Psi(\vec{R},\vec{r}_i) = (T_N + T_e + V)\,\Psi(\vec{R},\vec{r}_i) = E\,\Psi(\vec{R},\vec{r}_i)\,. \tag{2.2}$$

In the Born-Oppenheimer approximation we can assume the motion of the nuclei to be "frozen out" in comparison to the much faster motion of the electrons. This is justified, since the reduced mass $\mu = \frac{m_A m_B}{m_A+m_B}$ of the nuclei is about 3 orders of magnitude larger than the electron mass m_e, while the Coulomb forces acting on both are comparable. In the center of mass frame, we can neglect the kinetic term of the nuclei ($T_N = 0$) and consider the Coulomb potential as a time-independent effective potential $V(R)$ with the internuclear distance R as parameter. This allows writing down the time-independent Schroedinger equation for the electronic part of the wavefunction Ψ_q

$$H_e\,\Psi_q(\vec{R},\vec{r}_i) = (T_e + V(R))\;\Psi_q(\vec{R},\vec{r}_i) = E_q\,\Psi_q(\vec{R},\vec{r}_i)\,, \tag{2.3}$$

with the kinetic energy of the electrons $T_e = -\sum_{i=1}^{N} \frac{\hbar^2}{2m_e}\nabla_i^2$. Solving this equation numerically for different values of the parameter R gives the potential curves $E_n(R)$ of the electronic energies. While the eigenvalues only depend on the internuclear separation R, the eigenfunctions $\Psi_q(\vec{R},\vec{r}_i)$ are angle dependent and therefore depend on the orientation $\vec{R}$ of the internuclear axis as well. The electronic wavefunctions form a complete basis of the total molecular wavefunction,

$$\Psi(\vec{R},\vec{r}_i) = \sum_q \chi_q(\vec{R})\Psi_q(\vec{R},\vec{r}_i)\,, \tag{2.4}$$

with the nuclear wavefunctions $\chi_q(\vec{R})$. We can insert this into the time-independent Schroedinger equation 2.2, multiply by Ψ_n^* from the left and integrate over the electronic coordinates $\vec{r}_i$. This gives

$$\sum_q \int d\vec{r}_1..d\vec{r}_N\;\Psi_n^*(T_N + T_e + V(R))\chi_q(\vec{R})\Psi_q = E\underbrace{\sum_q \chi_q(\vec{R})\int d\vec{r}_1..d\vec{r}_N\;\Psi_n^*\Psi_q}_{=\chi_n(\vec{R})}\,. \tag{2.5}$$

The left side of equation 2.5 can be written as the sum of a term containing $(T_e + V(R))$ and another term containing T_N. The first term can be simplified by using equation 2.3 to

$$\sum_q \chi_q(\vec{R}) \int d\vec{r}_1..d\vec{r}_N \, \Psi_n^* \underbrace{(T_e + V(R))\Psi_q}_{=E_q\Psi_q} = \sum_q E_q \chi_q(\vec{R}) \underbrace{\int d\vec{r}_1..d\vec{r}_N \, \Psi_n^* \Psi_q}_{=\delta_{qn}} \quad (2.6)$$

$$= \chi_n(\vec{R}) E_n \, . \quad (2.7)$$

The part containing the kinetic energy T_N of the nuclei is simplified by applying the adiabatic approximation, where the nuclei's motion is assumed as slow compared to the motion of the electrons, which adapt quickly to changes in $\vec{R}$. The approximation gives

$$\nabla_R^2(\chi_q(\vec{R})\Psi_q) = \nabla_R^2(\chi_q(\vec{R}))\Psi_q + 2\nabla_R(\chi_q(\vec{R}))\nabla_R(\Psi_q) + \chi_q(\vec{R})\nabla_R^2(\Psi_q) \quad (2.8)$$

$$\approx \nabla_R^2(\chi_q(\vec{R}))\Psi_q \, . \quad (2.9)$$

We then get a solvable equation for the nuclear wavefunction,

$$\left(-\frac{\hbar^2}{2\mu}\nabla_R^2 + E_n(R) - E \right) \chi_n(\vec{R}) = 0 \, . \quad (2.10)$$

Expressing the Laplace operator ∇_R^2 in spherical coordinates gives

$$\left(-\frac{\hbar^2}{2\mu}\frac{1}{R^2}\frac{\partial}{\partial R}\left(R^2\frac{\partial}{\partial R}\right) + \frac{\hat{N}^2}{2\mu R^2} + E_n(R) - E \right) \chi_n(\vec{R}) = 0 \, , \quad (2.11)$$

where N is the operator for the rotational angular momentum of the molecule. The nuclear wavefunction can be separated into a radial part and an angular part,

$$\chi_n(\vec{R}) = \frac{1}{R} f_\nu(R) \, g(\Theta, \Phi) \, . \quad (2.12)$$

Inserting this into equation 2.11, we can separate the terms that depend only on the radial parameter R from the angular dependent parts of the equation. The angular solutions are the well known spherical harmonics $g(\Theta, \Phi) = Y_{NM}(\Theta, \Phi)$, which satisfy the relation $\hat{N}^2 Y_{NM}(\Theta, \Phi) = N(N+1)Y_{NM}(\Theta, \Phi)$ of the rotational

operator $\hat{N}$. We are left with the radial equation

$$\left(-\frac{\hbar^2}{2\mu}\frac{d^2}{dR^2} + \frac{N(N+1)}{2\mu R^2} + E_n(R) - E\right) f_\nu(R) = 0\,. \tag{2.13}$$

A Taylor expansion of the electronic potential around R_0 gives

$$E_n(R) \approx E_n(R_0) + \frac{1}{2}k(R-R_0)^2\,, \tag{2.14}$$

with $k = \frac{d^2E_n(R)}{dR^2}|_{R_0}$. The higher Taylor terms can be neglected for low vibrational quantum numbers[1]. If we also neglect the stretching of the internuclear distance R in rotations, meaning that we approximate $\frac{N(N+1)}{2\mu R^2} \approx \frac{N(N+1)}{2\mu R_0^2}$, the radial equation becomes the well known harmonic oscillator equation. We get the total energy E:

$$\begin{aligned} E &= E_N + E_\nu + E_n(R)\,, & (2.15)\\ E_N &= \frac{N(N+1)\hbar^2}{2\mu R_0^2}\,, & (2.16)\\ E_\nu &= (\nu+1/2)\hbar\omega_e\,, & (2.17) \end{aligned}$$

with $\omega_e = \sqrt{k/\mu}$. The total wavefunction is the product of electronic, vibrational and rotational wavefunctions,

$$\Psi(\vec{R},\vec{r}_i) = \underbrace{\Psi_n(\vec{R},\vec{r}_i)}_{electronic} \cdot \underbrace{R^{-1}f_\nu(R)}_{vibrational} \cdot \underbrace{Y_{NM}(\Theta,\Phi)}_{rotational}\,. \tag{2.18}$$

The electronic, vibrational and rotational energies are the main contribution to molecular energy levels. In the complete description however we find more terms that we neglected so far, like the centrifugal distortion of rotating molecules, the spin-orbit coupling, the spin-rotation coupling, the Λ-doubling and the hyperfine interaction. These couplings will be explained in the next chapters, and the notation of molecular states will be introduced.

2.1.2 Molecular state notation

Instead of the spherical symmetry that we find in atoms, diatomic molecules are axially symmetric around the internuclear axis $\vec{z}$. Since the angular momentum $\hat{L}$

[1] including higher terms leads to the so called Morse potential

of the electron no longer commutes with the electronic Hamiltonian operator $\hat{H}_e$, we introduce the quantum number Λ, which describes the projection of $\hat{L}$ onto the internuclear axis. It then makes sense to also introduce Σ, describing the projection of $\hat{S}$ onto the internuclear axis. The spin quantum number S is still a good quantum number. The new quantum numbers satisfy the equations

$$\begin{aligned} \hat{L}_z|\Lambda\rangle &= \Lambda\hbar|\Lambda\rangle\,, \\ \hat{S}_z|S,\Sigma\rangle &= \Sigma\hbar|S,\Sigma\rangle\,, \\ \hat{S}^2|S,\Sigma\rangle &= S(S+1)\hbar^2|S,\Sigma\rangle\,. \end{aligned}$$

States with quantum number Λ =(0, 1, 2 ...) are described with the letters (Σ, Π, Δ, ...). Here the Σ-state should not be confused with the quantum number Σ for the spin projection. Analogous to the total angular momentum $\hat{J} = \hat{L} + \hat{S}$ in atoms, we also define $\Omega = \Sigma + \Lambda$, with Ω being a good quantum number in some but not all cases (see next sections). The electronic state general quantum number is denoted by a unique letter (X, A, B, C, ...), where X describes the ground state and A the first excited state etc. .
The complete description of a molecular electronic state is of the form

$$(\text{unique letter})^{2S+1}\Lambda_{\Omega}^{\pm}\ .$$

The term $(2S+1)$ is called the multiplicity since it determines the number of states in the spin-orbit coupling (singlet, doublet etc.). The superscript $\pm$ does not describe the parity, but instead the reflection symmetry of the electronic state through a plane containing the internuclear axis, and is used only for Σ states. For symmetry reasons such a reflection maintains the electronic energy eigenvalue, but changes the angular projection quantum number from Λ to $-\Lambda$. This means all states with $\Lambda \neq 0$ are doubly degenerate. The coupling of the two states to the rotation of the nuclei can split the energy levels, which is known as Λ-doubling. In the case of $\Lambda = 0$, effective one-electron wavefunctions like we find for alkaline earth monofluorides will only have one state. Since it doesn't change by reflection in the plane, it is denoted as Σ^+.

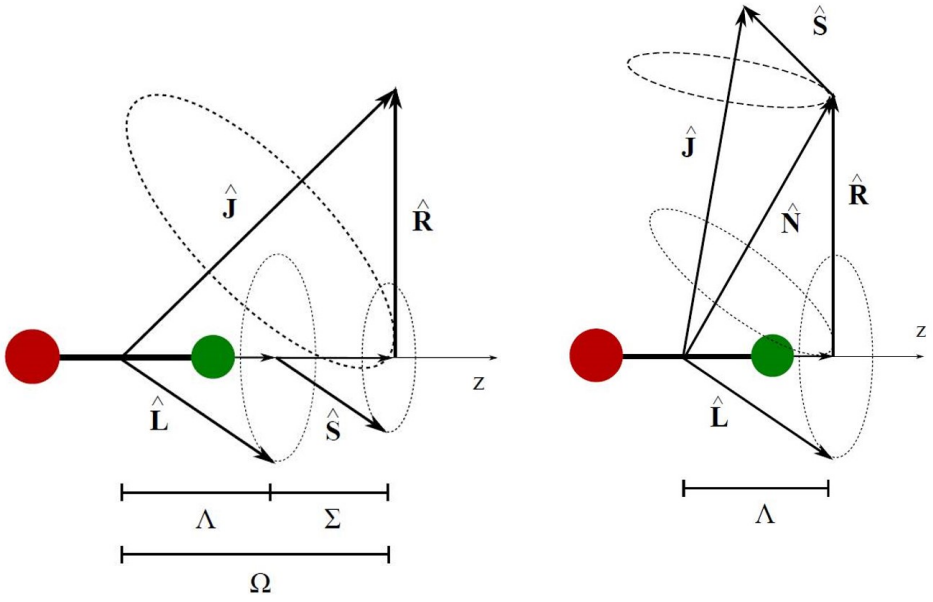

Figure 2.1: Left: Hund's case a.) for coupling of angular momenta. Right: Hund's case b.). Both graphics are taken from [66].

Apart from the Λ-doubling, the energy of the molecular states depends on the coupling of many different angular momenta (orbital, rotational, electron spin, nuclear spin etc.) to each other. Since the coupling strength varies for different molecular states and not all momenta are conserved at all times, it is helpful to distinguish different cases and their good quantum numbers. The two cases relevant for CaF will be described in the following sections.

2.1.3 Hund's case a.)

In Hund's case a.) the coupling of the nuclei's rotation $\hat{R}$ to the electron's spin $\hat{S}$ and angular momentum $\hat{L}$ is very weak ($\Delta E^{\text{el}} \gg \Delta E^{\text{spin-orbit}} \gg \Delta E^{\text{rot}}$). Instead, $\hat{S}$ and $\hat{L}$ are strongly coupled to the internuclear axis $\vec{z}$ (see figure 2.1). $\hat{L}$ and $\hat{S}$ couple with the rotation of the molecule to produce the total angular momentum $\hat{J} = \hat{R} + \hat{L} + \hat{S}$.

The good quantum numbers in Hund's case a.) are S, Σ, Λ, Ω and J. It is the right case to describe the first excited state $A^2\Pi_{1/2}$ of CaF.

2.1.4 Hund's case b.)

In Hund's case b.), the angular momentum $\hat{L}$ again processes around $\vec{z}$. But this time the coupling between the rotation $\hat{R}$ and the orbital angular momentum $\hat{L}$ plays the dominant role. ($\Delta E^{\text{el}} \gg \Delta E^{\text{rot}} \gg \Delta E^{\text{spin-orbit}}$). The product is the total rotational momentum $\hat{N} = \hat{R} + \hat{L}$, which further couples with the spin of the electron and gives $\hat{J} = \hat{N} + \hat{S}$.

The good quantum numbers in Hund's case b.) are S, Λ, N and J. It is the right case to describe the ground state $X^2\Sigma^+$ and the second excited state $B^2\Sigma^+$ of CaF.

2.2 Choosing a suitable molecule

CaF has several properties that make it one of the most suitable choices for laser cooling (see table 2.1). It has a reasonably high dipole moment of 3.07 Debye [67], which makes it interesting for many applications in the future. The lifetime of the first excited state of CaF is 19 ns, small enough to allow quick optical cycling. CaF is significantly lighter than other candidate molecules, which means that the same number of scattered photons will lead to a stronger maximum acceleration[2] $a_{\max} = \frac{\hbar k \Gamma}{2m}$. Most importantly, it has favourable Franck-Condon factors, which allows using only two or three vibrational repump lasers to make a MOT (see section 2.3.1).

Another argument for choosing CaF is the availability of tunable lasers (especially diode lasers) in the necessary wavelength regime. The energy levels of CaF are shown in figure 2.2. The cooling transition $X^2\Sigma^+(\nu' = 0, N' = 1) \rightarrow A^2\Pi_{1/2}(\nu'' = 0, J = 1/2, p = +)$ (abbreviated as "A-X") has a wavelength of 606 nm, while the three vibrational repump lasers run at 628.6 nm, 628.1 nm and 627.7 nm. As explained in chapter 5.3 we were able to tune a commercial laser diode to these repump wavelengths. Additionally, we use the $X^2\Sigma^+(\nu' = 0, N' = 1) \rightarrow B^2\Sigma^+(\nu'' = 0, N'' = 0)$ ("B-X") transition to slow the molecular beam, with a wavelength of 531 nm.

[2] This is an upper limit, not taking into account the reduced scattering rate in a multilevel system, see section 2.4.2.

molecule	λ_{00} (nm)	q_{00} (%)	q_{01} (%)	q_{02} (%)	q_{03} (%)	mass (amu)	excited state lifetime (ns)	$a_{\max}$ (m/s^2)
CaF [68]	606	96.4	3.5	0.12	2.5×10^{-3}	59	19	4.7×10^4
SrF [55]	663	98.1	1.8	0.04	10^{-3}	107	24	1.9×10^4
YO [60]	614	99.4	0.4	0.04	$< 10^{-4}$	105	33	1.5×10^4
YbF [69]	552	92.8	6.9	0.30	< 0.2	192	28	1.1×10^4
BaH*[70]	905	96.4	3.6	0.02	$< 10^{-3}$	138	125	2.0×10^3
MgF [68]	359	98.6	1.4	0.02	$< 10^{-3}$	43	7	2.9×10^5
BH [58]	433	98.6	1.3	0.09	$< 7 \times 10^{-3}$	12	127	4.8×10^4
BaF [71]	860	95.1	4.8	0.15	2.7×10^{-3}	157	56	4.2×10^3
TlF* [72]	272	98.9	<0.2	1.1	$< 3 \times 10^{-2}$	223	99	5.3×10^3
AlF [73, 74]	228	99.99	0.0009	0.007		46	1.9	1.6×10^6

Table 2.1: Properties of some candidate polar molecules for laser cooling. The q_{ij} describe the Franck-Condon factors for transitions between ground and first excited electronic state in which the vibrational quantum number changes from j to i. The values of molecules marked with * are for the (B-X) transition instead. YbF and TlF are less suitable for laser cooling than other molecules on the list, but of special interest for high precision measurements.

2.3 Energy level structure of CaF

After understanding the basics and origin of the complex level structure of simple diatomic molecules, let's now have a look at our molecule of choice, calcium fluoride.

2.3.1 Vibrational branching

There are no selection rules for the change of the vibrational quantum number in an electronic transition. Instead, vibrational branching in spontaneous decay is governed by the Franck-Condon factors (FCF) $q_{\nu'\nu}$, where ν' and ν are the vibrational quantum numbers of the excited and ground electronic state respectively. The FCFs are defined as the square of the overlap integral between the different vibrational wavefunctions,

$$q_{\nu''\nu'} = \left(\int f^*_{\nu''}(R) f_{\nu'}(R)\, dR \right)^2 . \tag{2.19}$$

From the FCFs we can directly calculate the vibrational branching ratios (e.g. the relative probabilities of decay) via

$$b_{\nu''\nu'} = \frac{q_{\nu''\nu'} \cdot \omega^3_{\nu''\nu'}}{\sum_j q_{\nu''j} \cdot \omega^3_{\nu''j}} . \tag{2.20}$$

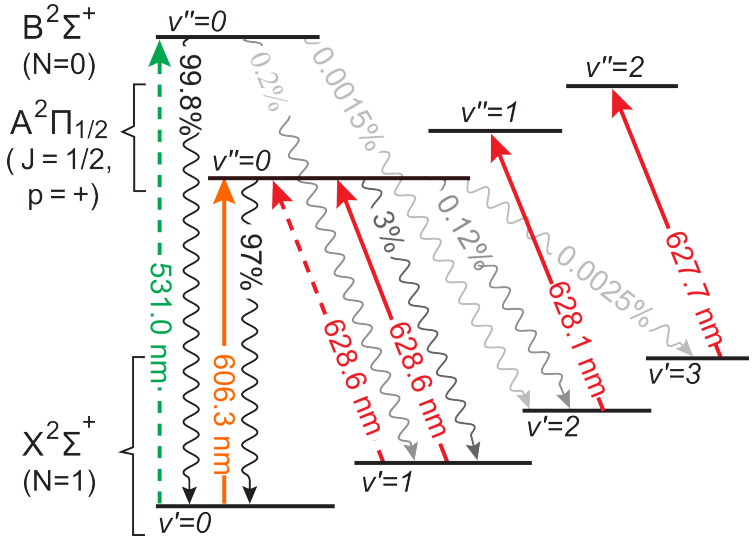

Figure 2.2: Laser cooling scheme for CaF. Solid arrows are transitions used for trapping in the MOT, dashed arrows are transitions used in laser slowing. Wavy lines indicate spontaneous decay with given Franck-Condon factors. The hyperfine levels of ground and excited state are not shown here.

Since in our case the transition frequencies into the different vibrational states are almost equal, the FCFs effectively present the decay probabilities.

Figure 2.2 shows the first 4 vibrational states of the ground state $X^2\Sigma^+$ and the branching ratios for the A and B states to each of these vibrational states of X. With only about $3 \cdot 10^{-3}\,\%$ decays from the $\nu'' = 0$ vibrational level of the first excited state into $\nu' \geqslant 3$ vibrational levels of the ground state, we expect $n_{sc} = 1/(3 \cdot 10^{-5}) \approx 3 \cdot 10^4$ scattered photons per molecule when using two repump lasers. Adding a third repump laser increases this number to about $n_{sc} = 1/(1.2 \cdot 10^{-6}) \approx 8 \cdot 10^5$ photons.

At this point we should check whether the probability for decay to higher lying vibrational states is becoming comparable to the probability of magnetic dipole (M1) or electric quadrupole (E2) transitions. The selection rules for these transitions state that the parity cannot change, unlike in electric dipole transitions (E1), where it has to change. This means M1 and E2 transitions will bring the populations into states not addressed by our lasers.

M1 transitions are suppressed by a factor $\alpha^2/4 \approx 10^{-5}$ (with $\alpha = 1/137$) com-

pared to E1 transitions ([65], p. 66). Additionally, the Einstein coefficient A_{ij} is proportional to ω_{ij}^3, so the total suppression factor is

$$\frac{A_{\mathrm{M1}}}{A_{\mathrm{E1}}} = \frac{\alpha^2}{4}\frac{\omega_{\mathrm{M1}}^3}{\omega_{\mathrm{E1}}^3} \approx 10^{-5} \times \frac{\omega_{\mathrm{M1}}^3}{\omega_{\mathrm{E1}}^3}\,. \tag{2.21}$$

M1 transitions do not change the electron orbital, which means that transitions from the A to the X state are suppressed since these states correspond to different electron orbitals. Transitions within the A state have transition frequencies that are many orders of magnitude smaller, leading to a large suppression factor according to equation 2.21. Despite this, M1 transitions have been found to be surprisingly large in some molecules [75].

Electrical quadrupole (E2) selection rules on the other hand allow transitions from the A to the X state, given that the parity doesn't change and $|\Delta J|, |\Delta M_J| \leqslant 2$. For E2 transitions with $\omega_{E2} \approx \omega_{E1} = \omega$, the relative strength compared to E1 transitions is given by (see [65], p. 68)

$$\frac{A_{\mathrm{E2}}}{A_{\mathrm{E1}}} = \frac{\omega^2\, a^2}{4c^2} \approx 1 \times 10^{-6}\,, \tag{2.22}$$

with the size $a \approx 2 \cdot 10^{-10}$ m of the CaF molecule[3]. According to this approximation, electric quadrupole transitions might play a role in our MOT, as they are similarly likely as losses to $\nu' \geqslant 4$ vibrational states.

On the B-X transition, which is used for laser slowing of the molecular beam[4], we only need a single repump laser to scatter about $7 \cdot 10^4$ photons. This is enough to slow a CaF molecule from 150 m/s to rest, since each absorption of a photon at $\lambda = 531$ nm reduces the velocity by $\Delta v = \hbar k / m_{CaF} = 1.3$ cm/s, resulting in about $1.2 \cdot 10^4$ required photon scatters.

2.3.2 Rotational branching

The rotational levels of CaF are shown in figure 2.3, including also the Λ-doubling, fine and hyperfine structure. The important thing to note is that, according to

[3] approximated by the atomic radius of Ca, found in the periodic table

[4] The B-X transition isn't used for the MOT because our numerical model suggests that it has a lower capture velocity [76]

dipole selection rules, $\Delta J = (0, \pm 1)$ and the parity of the state has to change. In our experiment we always drive transitions from the negative parity ground state with $N = 1$ to positive parity excited states. From there, decays are only allowed back to negative parity states. While both $N = 1$ and $N = 3$ have negative parity, decay to the $N = 3$ state of the ground state is forbidden from both the $A^2\Pi_{1/2}(J = 1/2)$ and the $B^2\Sigma^+(N = 0)$ state. This is because the $N = 3$ ground state has $J = (5/2, 7/2)$ so it can't be reached from a $J = 1/2$ upper state with $\Delta J = 0, \pm 1$. Since $\vec{J} = \vec{N} + \vec{S}$, the quantum numbers $N = 0$ and $S = 1/2$ imply $J = 1/2$ for the B state. In the A state, described by the Hund's case a.), we only address the $J = 1/2$ state. This means our laser cooling transitions A-X and B-X are both rotationally closed.
The rotational energies (in rigid rotor approximation) are given by

$$E_N = B_e N(N + 1)\,, \tag{2.23}$$

with $B_e = 10.1$ GHz [66].

2.3.3 Spin-orbit coupling

In Hund's case a.) (describing the A state) the spin $\hat{S}$ couples directly to the angular momentum $\hat{L}$. Both L and S are precessing around the internuclear axis, with projections Λ and Σ, so that their coupling can be described by the quantum number $\Omega = \Sigma \pm \Lambda$. In the $A^2\Pi$ state ($\Sigma = 1/2$, $\Lambda = 1$), we find a doublet with $\Omega = (1/2, 3/2)$, of which we only address the $\Omega = 1/2$ state (labelled $\Pi_{1/2}$) with a laser. The Hamiltonian of the interaction is [77]

$$E_{LS} = A_{LS}\hat{L} \cdot \hat{S}\,. \tag{2.24}$$

Since both $\hat{L}$ and $\hat{S}$ are oriented along the internuclear axis, the splitting is simply

$$E_{LS} = A_{LS}\Lambda\,\Sigma\,, \tag{2.25}$$

with the molecular constant[5] $A_{LS} \approx 2.1$ THz [78].

[5] we neglect the weak dependence on the vibrational quantum number ν

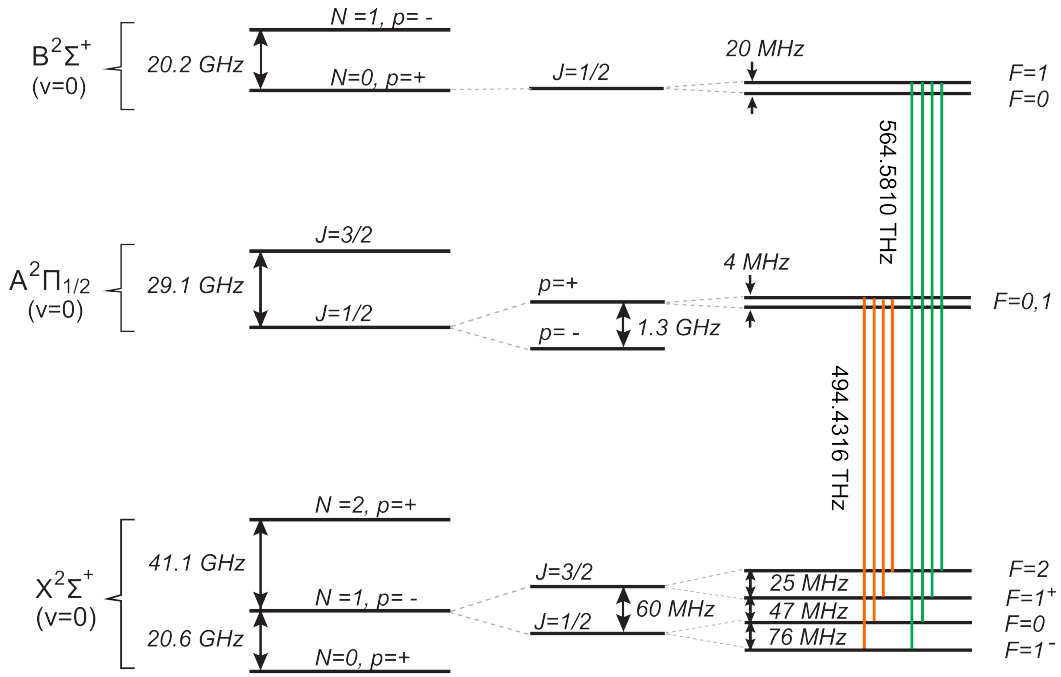

Figure 2.3: Rotational and hyperfine branching of CaF. (v, N, J, F) are the quantum numbers for vibration, rotational angular momentum, total electronic angular momentum and total angular momentum. The parity of the states is labelled as p. The main cooling transitions used for trapping in the MOT and laser slowing of the beam are shown in orange and green respectively.

2.3.4 Spin-rotation coupling

The spin-rotation coupling in Hund's case b.) (describing X and B state) with $S = 1/2$ leads to states with $J = (N - 1/2, N + 1/2)$. In case of the $X^2\Sigma^+(N = 1)$ state we get $J = (1/2, 3/2)$, while the $B^2\Sigma^+(N = 0)$ only has one state with $J = 1/2$. The Hamiltonian of the interaction is

$$H_{NS} = \gamma_{\nu N}\, \hat{N} \cdot \hat{S} \tag{2.26}$$

with the molecular constant[6] $\gamma_{\nu N} = 39.7$ MHz [66]. Since $\hat{N} \cdot \hat{S} = (\hat{J}^2 - \hat{N}^2 - \hat{S}^2)/2$, we find the energies

$$E_{NS} = \frac{\gamma_{\nu N}}{2}(J(J+1) - N(N+1) - S(S+1))\,. \tag{2.27}$$

For the X state with $S = 1/2$, $N = 1$ and $J = (1/2, 3/2)$ we find the splitting $\Delta E = E_{NS,J=3/2} - E_{NS,J=1/2} \approx 60$ MHz.

2.3.5 Lambda doubling

The Hund's cases should be understood more as an approximation than a rigid classification. For example, there can be a transition from Hund's case a.) to case b.) with growing rotational quantum number N, which causes the spin $\hat{S}$ to uncouple from the internuclear axis and couple with $\hat{N}$.
Another example is the decoupling of the angular momentum $\hat{L}$ from the internuclear axis, due to the coupling between $\hat{L}$ and the rotation $\hat{N}$ of the molecule. This interaction leads to a splitting of otherwise degenerate energy levels with quantum number $\pm\Lambda$ and is known as Λ-doubling [77]. It only occurs in the cases where $\Lambda > 0$, like in the A state of CaF, but not in the X and B states. In the $A^2\Pi_{1/2}(J = 1/2)$ state of CaF, the energy splitting between the two states is about 1.35 GHz [79].

2.3.6 Hyperfine structure

The hyperfine interaction $\hat{F} = \hat{J} + \hat{I}$ of electronic total angular momentum $\hat{J}$ with the nuclear spin $I = 1/2$ is responsible for the level splitting with the lowest energy

[6] again, we neglect the dependence of the constant on quantum numbers ν and N

scale (see figure 2.3). In the X state, the $J = (1/2, 3/2)$ states split into a total of four states with $F = (1^-, 0, 1^+, 2)$, where the superscript is only used to distinguish the two $F = 1$ states. In the A state, $J = 1/2$ leads to two states with $F = (0, 1)$, which are separated by only 4.8 MHz [80]. This is less than the linewidth of the transition, and the states are therefore not resolved. The splitting of the X state (see figure 2.3) is of the order of tens of MHz and can be addressed by modulating a single laser frequency with EOMs and AOMs (see chapter 5.4).

2.4 Scattering rate and cooling force

2.4.1 Two-level system

The force that a laser exerts on a molecule or atom is proportional to the rate at which photons are scattered, (=absorbed and spontaneously re-emitted), since each scattering event produces an average momentum kick of $\hbar\vec{k}$. In a simple two-level system the scattering rate follows from the Bloch equations, a set of four coupled differential equations, to give [65]

$$R_{\mathrm{sc}} = \Gamma\rho_{ee} = \frac{\Gamma}{2}\frac{s_0}{1 + s_0 + 4(\Delta/\Gamma)^2}\,, \tag{2.28}$$

with total detuning Δ, decay rate Γ and excited state population ρ_{ee} in the steady state. The saturation parameter $s_0 = I/I_{\mathrm{sat}} = 2\Omega^2/\Gamma^2$ is calculated from the saturation intensity

$$I_{\mathrm{sat}} = \frac{\pi h c \Gamma}{3\lambda^3}\,. \tag{2.29}$$

With $\Gamma = 2\pi \times 8.3$ MHz ($2\pi \times 6.3$ MHz) in the first (second) excited state in CaF we find $I_{\mathrm{sat}} = 4.9$ mW/cm^2 (5.5 mW/cm^2). The maximum scattering rate in a two level system is $\Gamma/2$, in which case the population is equally distributed between the two states. This is because the Einstein coefficients for absorption and stimulated emission are equal, and both processes balance out at $\rho_{ee} = 1/2$, so that increasing the pump intensity further does not increase ρ_{ee}.

2.4.2 Multi-level system

Let's now consider a system with n_e excited states and n_g ground states. As before, the scattering rate can be derived from a (now larger) set of coupled differential equations. The result is [37]

$$R_{\mathrm{sc}} = \Gamma \frac{n_e}{(n_g + n_e) + 2\sum_{j=1}^{n_g}(1 + 4\Delta_j^2/\Gamma^2) I_{\mathrm{sat},j}/I_j}\,, \tag{2.30}$$

with the saturation intensities $I_{\mathrm{sat},j}$ and intensities I_j of the transitions to each ground state level. We can assume that all levels have the common values $\Delta_j = \Delta$ and $I_{\mathrm{sat},j} = I_{\mathrm{sat}}$ and are driven by an intensity $I_j = I/n_g$, where the total intensity I is equally divided over all ground states. Inserting these assumptions into equation 2.30 allows writing the scattering rate in the same form as before,

$$\begin{aligned} R_{\mathrm{sc}} &= \frac{\Gamma_{\mathrm{eff}}}{2} \frac{s_{\mathrm{eff}}}{1 + s_{\mathrm{eff}} + 4(\Delta/\Gamma)^2}\,, & (2.31)\\ \Gamma_{\mathrm{eff}} &= \frac{2n_e}{n_e + n_g}\Gamma\,, & (2.32)\\ s_{\mathrm{eff}} &= I/I_{\mathrm{sat,eff}}\,, & (2.33)\\ I_{\mathrm{sat,eff}} &= \frac{2n_g^2}{n_g + n_e} I_{\mathrm{sat}}\,, & (2.34) \end{aligned}$$

with the effective saturation intensity $I_{\mathrm{sat,eff}}$ and the effective scattering rate Γ_{eff}.

2.4.3 The laser cooling force

From the scattering rate we can directly derive the force onto a molecule travelling at velocity v in a one-dimensional optical molasses. It is the sum of the forces $\vec{F}_\pm$ from the two counter-propagating lasers with corresponding Doppler shifts $\Delta_D = \pm k \cdot v$, given as [81]

$$\vec{F}_\pm = \pm\hbar\vec{k}\,\frac{\Gamma_{\mathrm{eff}}}{2} \frac{s_{\mathrm{eff}}}{1 + s_{\mathrm{eff}} + 4((\Delta \mp kv)/\Gamma)^2}\,. \tag{2.35}$$

Adding the two forces and neglecting terms of order $(kv/\Gamma)^4$, we get

$$\vec{F}_{\mathrm{OM}} = \vec{F}_+ + \vec{F}_- \approx \frac{8\Gamma_{\mathrm{eff}}\hbar k^2 \Delta s_{\mathrm{eff}} \vec{v}}{\Gamma^2(1 + s_{\mathrm{eff}} + (2\Delta/\Gamma)^2)^2} = -\beta\vec{v}\,. \tag{2.36}$$

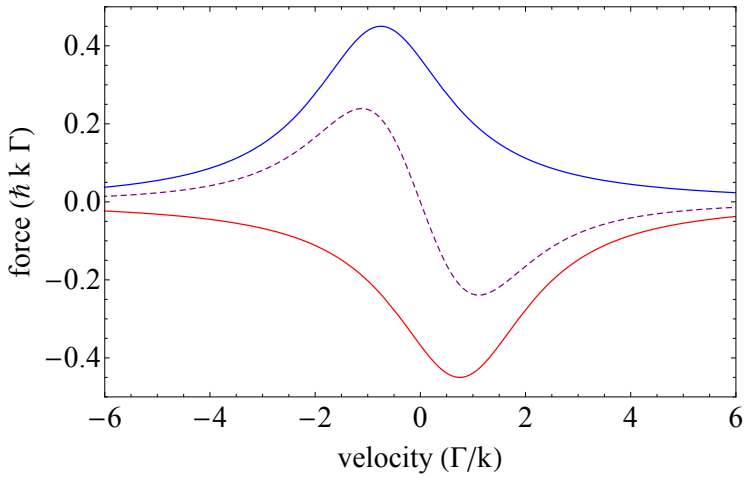

Figure 2.4: The laser cooling force vs velocity of the molecule. Purple dashed line is the total force in the optical molasses and the sum of the contributions of the two counter-propagating lasers (red and blue). The plot uses $s_{\text{eff}} = 9$ and $\Delta = -0.75\Gamma$, as typically used in our MOT.

We see that for $\Delta < 0$ (red detuned light) the molecules experience a friction force opposite to their motion: they are slowed. Since the mean velocity of a gas is directly related to its temperature, the molasses force cools the molecules.

The force F_{OM} is plotted in figure 2.4 for $s_{\text{eff}} = 9$ and $\Delta = -0.75\Gamma$. The maximum value of the force in this case is found when $v \approx \Gamma/k = 5.0$ m/s with $k = 2\pi/\lambda$.

2.4.4 Remixing dark states

Laser cooling on a $(N' = 1) \rightarrow (N'' = 0)$ transition closes the transition rotationally but inevitably creates dark states on transitions where $F' > F''$. Dark states are states from which no photon can be absorbed by the given laser polarisations. For example, in CaF the $m'_F = +2, -2$ levels of the $F' = 2$ hyperfine ground state are dark to the linearly polarised light used in our setup, as there is no possible transition to the excited electronic state which fulfils $\Delta m_F = 0$. If molecules have a certain probability to decay to a dark state, and no way out of it, all population will eventually end up there and laser cooling will stop.

Fortunately there are methods to avoid this. One technique is a fast switching of the polarisation between the two handednesses at MHz rates (comparable to the

natural linewidth Γ), so that states that are dark to one handedness can be quickly addressed by light of the opposite handedness. The alternative method is to rotate dark states into bright state via Larmor precession (again at MHz rates) by applying a magnetic field. In our experiment we use a magnetic field of 0.5 mT along the whole slowing chamber, oriented at 45° to the polarisation of the slowing lasers, to remix dark states [82].

Chapter 3

A cold and slow buffer gas beam of CaF

Buffer gas sources were first developed in the group of John Doyle at Harvard and are described in several papers [83, 26, 84, 85]. This chapter will first give an overview of the theory of buffer gas sources (more details can be found elsewhere [86, 87, 88]), and then present our buffer gas source of CaF. This intense, cold and slow molecular source of high reliability is a crucial step towards producing a MOT of CaF.

3.1 Theory of buffer gas sources

The idea of the buffer gas technique is simple: A hot gas of particles is cooled via collisions with a cryogenically cooled inert atomic gas (the buffer gas) inside a container of typically a few cm^3 (the buffer gas cell). The technique is applicable to almost every atomic or molecular species, regardless of its internal structure. The only requirement is that the collisions have to be elastic (no chemical reactions), which is why inert noble gases like helium or neon are the usual choice. The temperature of the buffer gas, limited by its vapour pressure, is typically around 4 K for He and around 20 K for Ne. After thermalising with the buffer gas, the particles of interest exit the cell through an aperture and form a beam (see figure 3.1). The properties of the beam (velocity, brightness, etc.) depend on the geometry of the cell and the flow of the buffer gas through it, as will be discussed in the next sections.

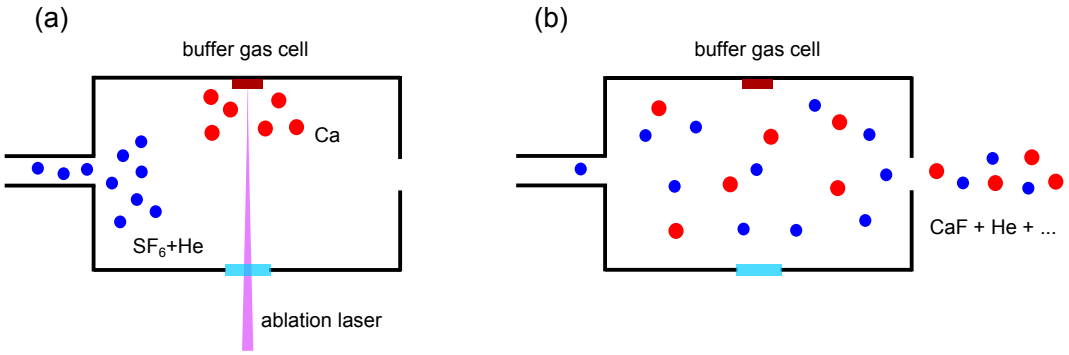

Figure 3.1: Sketch of the buffer gas beam method. (a): CaF molecules are produced by ablating Ca atoms from a target and associating them with fluorine atoms from SF_6 molecules, which are injected into the buffer gas cell together with the cold He buffer gas. (b): After thermalising via collisions with the buffer gas, the CaF molecules exit the cell through an aperture.

3.1.1 Effusive vs supersonic beams

The velocity distribution of an ideal gas at temperature T is given by the Maxwell-Boltzmann distribution,

$$f(v) = \frac{32\, v^2}{\pi^2 \bar{v}^3}\, e^{-4v^2/\pi\bar{v}^2}\,, \tag{3.1}$$

with the mean velocity[1]

$$\bar{v} = \sqrt{\frac{8k_\mathrm{B}T}{\pi\, m}}\,, \tag{3.2}$$

of the particles of mass m. For example, He atoms ($m_\mathrm{He} = 4$ amu) at room temperature travel with about $\bar{v} = 1250$ m/s, while at cryogenic temperatures of 4.5 K they move around with $\bar{v} = 154$ m/s. A gas of CaF molecules ($m_\mathrm{CaF} = 59$ amu) at 4.5 K would even slow down to $\bar{v} = 40$ m/s.

The velocities so far describe the motion of the particles in random directions. The actual forward velocity of molecules in a buffer gas beam depends crucially on the pressure in the buffer gas cell, which is controlled by the flow of the buffer gas through it. We distinguish between the high pressure regime, called the *supersonic* or *fully*

[1] the mean velocity is not to be confused with the most probable velocity, $v_p = \sqrt{\pi/4} \times \bar{v} = \sqrt{2k_\mathrm{B}T/m}$

hydrodynamic regime, and the low pressure regime, called the *effusive* regime. The two regimes are characterised by the Knudsen number,

$$\mathrm{Kn} = \frac{\lambda}{L} = \frac{1}{\sqrt{2}\, n\, \sigma\, L}\,. \tag{3.3}$$

Here $\lambda = (\sqrt{2} n \sigma)^{-1}$ describes the mean free path length of a gas with collisional cross section σ and number density n, and L is a characteristic length, typically the diameter of the aperture of the buffer gas cell. The inverse of the Knudsen number, Kn^{-1}, hence describes the number of collisions of a particle near the aperture of the cell. For high values $\mathrm{Kn} > 1$, we are in the effusive regime, while low values $\mathrm{Kn} < 0.01$ define the hydrodynamic regime, with an *intermediate* regime in between ($1 < \mathrm{Kn} < 0.01$). Alternatively, the regimes are often described by the Reynolds number Re. It is related to the Knudsen number via $\mathrm{Kn} \cdot \mathrm{Re} \approx 2\,\mathrm{Ma}$, where Ma is the Mach number defined as the ratio of the flow velocity to the speed of sound.

Let's first consider the effusive regime ($\mathrm{Kn} > 1$). Here the molecules experience barely any collisions with the buffer gas atoms in the vicinity of the aperture. This means their forward velocity is mostly independent from the forward velocity of the buffer gas atoms and is instead determined by their temperature T and described by the Maxwell Boltzmann distribution. Since the probability of a molecule exiting the cell through the aperture and joining the beam is proportional to its velocity v, the forward velocity distribution $f_{||}(v)$ in the beam is given by [86]

$$f_{||}(v) = f(v)\frac{v}{\bar{v}} = \frac{32\, v^3}{\pi^2 \bar{v}^4}\, e^{-4v^2/\pi\bar{v}^2}\,. \tag{3.4}$$

From this distribution we find the mean forward velocity of the molecules in the effusive beam,

$$\bar{v}_{||,\mathrm{eff}} = \frac{3\pi}{8}\bar{v} = \sqrt{\frac{9\pi}{8}\frac{k_\mathrm{B}\, T}{m_\mathrm{CaF}}} \tag{3.5}$$

A fully effusive beam of CaF molecules at 4.5 K has a mean velocity of $\bar{v}_{||} = 47$ m/s. Unfortunately effusive beams are usually less intense than supersonic beams.

In contrast to effusive beams, hydrodynamic buffer gas beams (Kn$<$ 0.01) show a high number of collisions of the molecules with the buffer gas near the cell aperture. The molecules are "swept out" of the cell by the buffer gas, which behaves as a fluid, and their velocity is about equal to the velocity of the buffer gas atoms. Once the beam exits the high pressure cell and enters the vacuum chamber, it expands and accelerates to its final velocity due to frequent momentum kicks from collisions with buffer gas atoms flowing out of the cell. At the same time the beam cools down in both internal and translational degrees of freedom.
The final forward velocity of the molecules in a hydrodynamic beam of He atoms can be found from thermodynamics as [89]

$$\bar{v}_{||,\mathrm{hy}} = \sqrt{\frac{\gamma}{\gamma-1}\frac{2k_\mathrm{B}\left(T-T_0\right)}{m_\mathrm{He}}}\,, \tag{3.6}$$

$$\approx \sqrt{\frac{\gamma}{\gamma-1}\frac{2k_\mathrm{B}\,T}{m_\mathrm{He}}}\,. \tag{3.7}$$

Here $\gamma = C_p/C_V$ is the specific heat ratio. It depends on the number of degrees of freedom f of the particle via $\gamma = 1 + 2/f$, leading to a value of $\gamma = 5/3$ for a monoatomic gas. The approximation above assumes $T >> T_0$, where T is the temperature before the supersonic expansion and T_0 is the final temperature. This leads to a velocity of the molecules in a hydrodynamic He beam of

$$\bar{v}_{||,\mathrm{hy}} = \sqrt{\frac{5\,k_\mathrm{B}\,T}{m_\mathrm{He}}}\,. \tag{3.8}$$

At 4.5 K this corresponds to $\bar{v}_{||} = 216$ m/s.

In our experiment we typically see velocities between the calculated effusive and hydrodynamic limits, indicating that we are operating in the intermediate regime.

3.1.2 Thermalisation

The molecules in a buffer gas cell are typically created via laser ablation at temperatures in the range of $10^3 - 10^4$ K[2]. The mean change in temperature of the molecules

[2]the exact ablation temperature is difficult to determine but does not influence the necessary number of collisions too strongly. In our case it could be approximated by the boiling point of Ca,

of mass m_{M} and temperature T_{M} after N_{c} collisions with a buffer gas of mass m_{b} and temperature T_{b} is given by the differential equation [90]

$$\frac{dT_{\mathrm{M}}(N_{\mathrm{c}})}{dN_{\mathrm{c}}} = -\frac{(T_{\mathrm{M}}(N_{\mathrm{c}}) - T_{\mathrm{b}})}{\kappa}\,, \tag{3.9}$$

with $\kappa = (m_{\mathrm{M}} + m_{\mathrm{b}})^2/(2m_{\mathrm{M}}m_{\mathrm{b}})$, which gives $\kappa = 8.4$ in our case. Here the temperature T_{b} of the buffer gas is assumed to be constant. The solution of this equation is

$$T_{\mathrm{M}}(N_{\mathrm{c}}) = T_{\mathrm{b}} + (T_{\mathrm{M}}(0) - T_{\mathrm{b}})e^{-N_{\mathrm{c}}/\kappa}\,. \tag{3.10}$$

The number of collisions $N_{\mathrm{c,th}}$ necessary to reach a temperature $T_{\mathrm{M}}(N_{\mathrm{c,th}}) = (1 + \epsilon_{\mathrm{t}})T_{\mathrm{b}}$ is

$$N_{\mathrm{c,th}} = -\kappa \ln\left(\frac{\epsilon_{\mathrm{t}}\, T_{\mathrm{b}}}{T_{\mathrm{M}}(0) - T_{\mathrm{b}}}\right) \approx \kappa \ln\left(\frac{\epsilon_t\, T_{\mathrm{b}}}{T_{\mathrm{M}}(0)}\right)\,. \tag{3.11}$$

For our CaF beam, assuming $T_{\mathrm{b}} = 4.5$ K and $T_{\mathrm{M}}(0) = 1000$ K, thermalisation to $\epsilon_{\mathrm{t}} = 0.1$ requires $N_{\mathrm{c,th}} = 65$ collisions. The thermalisation length,

$$L_{\mathrm{th}} \approx N_{\mathrm{c,th}}\lambda\,, \tag{3.12}$$

can then be calculated via the mean free path length,

$$\lambda = \frac{1}{\sigma_{\mathrm{Mb}} n_{\mathrm{cell}} \sqrt{\frac{m_{\mathrm{M}}}{m_{\mathrm{b}}} + 1}}\,, \tag{3.13}$$

with the number density $n_{\mathrm{cell}} = N/V$ of the buffer gas atoms and the collisional cross section σ_{Mb} between molecule and buffer gas atom. The length L of the buffer gas cell should be chosen larger than L_{th} to allow full thermalisation, but not too large since a larger size tends to decrease the extraction efficiency.

The number density can be found by using the fact that the buffer gas flow F into the cell is equal to the flow $\dot{N}$ out of the aperture. In the effusive regime, the flow

which is 1760 K at ambient pressure.

of a gas with thermal velocity $\bar{v}_\mathrm{b}$ out of a thin aperture of size A_a is [86]

$$\dot{N} = \frac{\bar{v}_\mathrm{b}\, n_\mathrm{cell}\, A_\mathrm{a}}{4}\,. \tag{3.14}$$

Setting $\dot{N} = F$, we get

$$n_\mathrm{cell} = \frac{4F}{A_\mathrm{a}\bar{v}_\mathrm{b}}\,. \tag{3.15}$$

In the hydrodynamic regime, the flow out of the aperture is increased by a factor of 1.8 (for monoatomic gases) compared to the effusive regime [91]. The He flow into the cell can be controlled with a flow controller and is usually measured in sccm (standard cubic centimeter per minute), with 1 sccm corresponding to about $4.5 \cdot 10^{17}$ atoms per second.

3.1.3 Diffusion and Extraction

After ablation, the molecules start diffusing in the cell. This process is in competition with the extraction of the molecules within the stream of buffer gas atoms. If the molecules diffuse to the cold walls of the cell before they are pumped out, they stick to it and are lost. It is hence useful to calculate the typical time scales τ_diff and τ_pump of the competing processes.

The diffusion of a species M into a gas of species b is described by the diffusion equation

$$\frac{dn_\mathrm{M}}{dt} = \nabla^2(D\, n_\mathrm{M})\,, \tag{3.16}$$

with the molecular number density n_M and the diffusion constant

$$D = \frac{3}{16 n_\mathrm{b}\sigma_\mathrm{Mb}}\sqrt{\frac{2\pi k_\mathrm{B}T}{\mu}}\,. \tag{3.17}$$

Here $\mu = (m_\mathrm{M}m_\mathrm{b})/(m_\mathrm{M}+m_\mathrm{b})$ is the reduced mass. In the lowest order diffusion mode, the diffusion time for a cubic cell with length L is [86]

$$\tau_\mathrm{diff} \approx \frac{16}{9\pi}\frac{L^2\, n_\mathrm{cell}\sigma_\mathrm{Mb}}{\bar{v}}\,. \tag{3.18}$$

The extraction time can be approximated by the time to empty the volume of the cell via the flow F,

$$\tau_{\mathrm{pump}} \approx \frac{N}{F} = \frac{4L^3}{A_{\mathrm{a}}\bar{v}}\,. \tag{3.19}$$

It is useful to define the dimensionless number

$$\gamma_{\mathrm{e}} = \frac{\tau_{\mathrm{diff}}}{\tau_{\mathrm{pump}}} = \frac{4}{9\pi}\frac{n_{\mathrm{cell}}\sigma_{\mathrm{Mb}}A_{\mathrm{a}}}{L} \approx \frac{\sigma_{\mathrm{Mb}}F}{L\bar{v}}\,, \tag{3.20}$$

a quantity which is closely related to the extraction efficiency ϵ [92]. If $\gamma_{\mathrm{e}} > 1$, the extraction efficiency will be close to $\epsilon = 1$ (also called hydrodynamic enhancement), while for $\gamma_{\mathrm{e}} << 1$ it reduces to $\epsilon \approx A_{\mathrm{a}}/S$, the ratio of the aperture area to the inner surface of the cell S, since the molecules diffuse in all directions with equal probability.

3.1.4 Mean free path outside the cell

It is crucial that the background pressure outside the buffer gas cell is low enough not to substantially attenuate the molecular beam via collisions. The mean free path equation $\lambda \approx 1/n\sigma$ predicts a mean free path length of 1.6 m, longer than the experimental setup, at the easily achievable pressure of $p = 5 \cdot 10^{-5}$ mbar. It contains no explicit dependence on the velocity of the particles. Unfortunately this is not true when the velocity of the beam and the background gas particles are vastly different. This is actually the case in our experiment: The CaF molecules are slowed down to velocities around 10 m/s, while a background Helium atom at 300 K has a mean velocity of $v_{\mathrm{bg}} = 1260$ m/s. In this case the molecule's movement can be seen as frozen compared to the background gas, which leads to a mean time between collisions given by

$$\tau_{\mathrm{c}} \approx \frac{1}{n_{\mathrm{bg}}\sigma_{\mathrm{Mb}}v_{\mathrm{bg}}} = \frac{k_{\mathrm{B}}T}{p\,\sigma_{\mathrm{Mb}}v_{\mathrm{bg}}}\,. \tag{3.21}$$

For He background gas at 300 K this means that we need a pressure of $p = 2 \cdot 10^{-6}$ mbar for a τ_{c} of 30 ms, which is the total time the molecules spend in the beam before reaching the MOT region. This is achieved with a skimmer acting as a

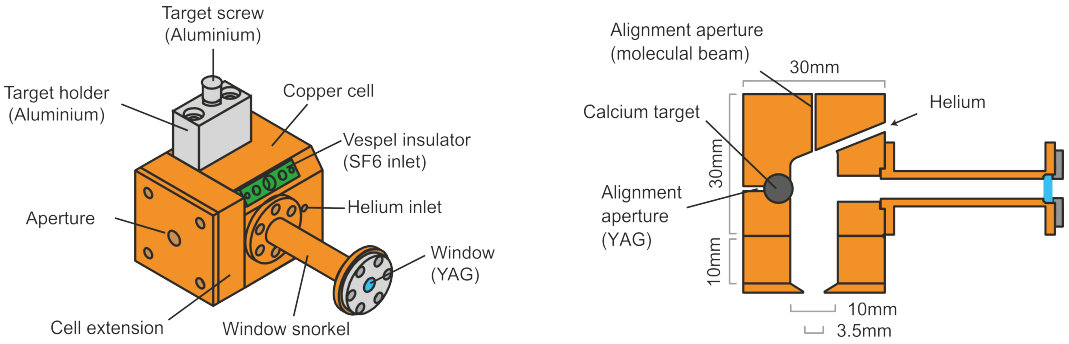

Figure 3.2: Design of the buffer gas cell.

differential pumping stage between source chamber and slowing chamber and an additional differential pumping stage between slowing chamber and MOT chamber (see chapter 7.1).

3.2 Experimental setup

3.2.1 Cell design and molecule production

The buffer gas cell (see figure 3.2) was designed to allow efficient thermalisation and extraction of CaF molecules. The underlying geometry is a copper cube of 30 mm length with a bore of 10 mm diameter as cell volume. The cell length can be adjusted by an extension piece. We found that an additional 10 mm length provide good thermalisation of the molecules with the buffer gas without substantially decreasing the beam intensity. The cell aperture size can be varied as well, here we find that a diameter of 3.5 mm works best.

The molecules are created by ablating Ca from a metal rod and adding Sulfur-Hexafluoride (SF_6) gas, which provides the fluorine to form CaF. The Ca rod can be rotated via a thread to change the ablation spot when needed. For this purpose, the target is connected to a rotational feedthrough on top of the source chamber. The ablation laser[3] enters the cell through a small window perpendicular to the beam axis. The window is set back by a tube (or "snorkel") to reduce deposition of ablated Ca. There are separate gas inlets for the 4 K Helium buffer gas and the room temperature SF_6. The SF_6 line is thermally disconnected from the cold

[3]pulsed Nd:YAG, $\lambda = 1064$ nm, 1-10 Hz, 6 mJ energy, 4 ns duration

cell via a vespel insulator, since the gas would freeze otherwise. We monitor the temperature of the SF_6 line and have installed a heater on it in case it freezes up, but with correct assembly of the source this never occurs. The flow of SF_6 is small compared to the He buffer gas and induces no noticeable heating. After simulations of the buffer gas flow in the cell done by N. Bulleid [93] it was decided to position the He inlet at an angle (see figure 3.2). This should provide a high He density near the ablation spot and allow efficient extraction. Before entering the cell, the He gas is fed through copper spirals connected to the 40 K and 4 K stages to make sure it is properly thermalised.

The buffer gas flow is controlled by a flow controller[4] and usually set to around 1 sccm. With the usual circular cell aperture of $d = 3.5$ mm diameter and a velocity of 200 m/s this gives a number density of He in the cell of $n_{\text{cell}} \approx 9.4 \times 10^{14}\text{cm}^{-3}$ and a mean free path length of $\lambda \approx 0.54$ mm, assuming $\sigma \approx \sigma_{\text{He-He}} \approx 0.5 \times 10^{-14}\text{cm}^2$ [87], which should be a good approximation for noble gases [88]. The Knudsen number then calculates to $\text{Kn} = \lambda/d = 0.15$, confirming that we are indeed in the intermediate flow regime. The extraction number evaluates to $\gamma_{\text{e}} \approx 0.32$, which suggests that slightly more molecules are diffusing to the cell walls than are pumped out. The distance between ablation spot and cell aperture is about 25 mm, leading to about $N_{\text{c}} = 50$ collisions of the molecules with the buffer gas in the cell. According to equation 3.10 this should result in thermalisation down to $T(50) \approx 7$ K, assuming the buffer gas is at 4.5 K. A slightly longer cell could cool the molecules further, but would decrease the intensity of the beam.

3.2.2 Source chamber

The buffer gas cell is mounted on the cold plate of a closed cycle pulsed tube helium cryocooler[5] in the source chamber (see figure 3.3). The cell is surrounded by a copper cylinder, which is thermally connected to the 4 K cold plate. The inner surface of the cylinder is covered in charcoal (see appendix B), which acts as a cryopump by freezing the He atoms to the enhanced surface area of the porous material. An additional charcoal covered plate (known as the skimmer plate) with an aperture

[4] alicat MCE series (0-1 sccm) or mks G series (1-7 sccm), depending on the required flow
[5] Sumitomo RDK-415D, 1.5W@4.2 K, 35-45W@50 K

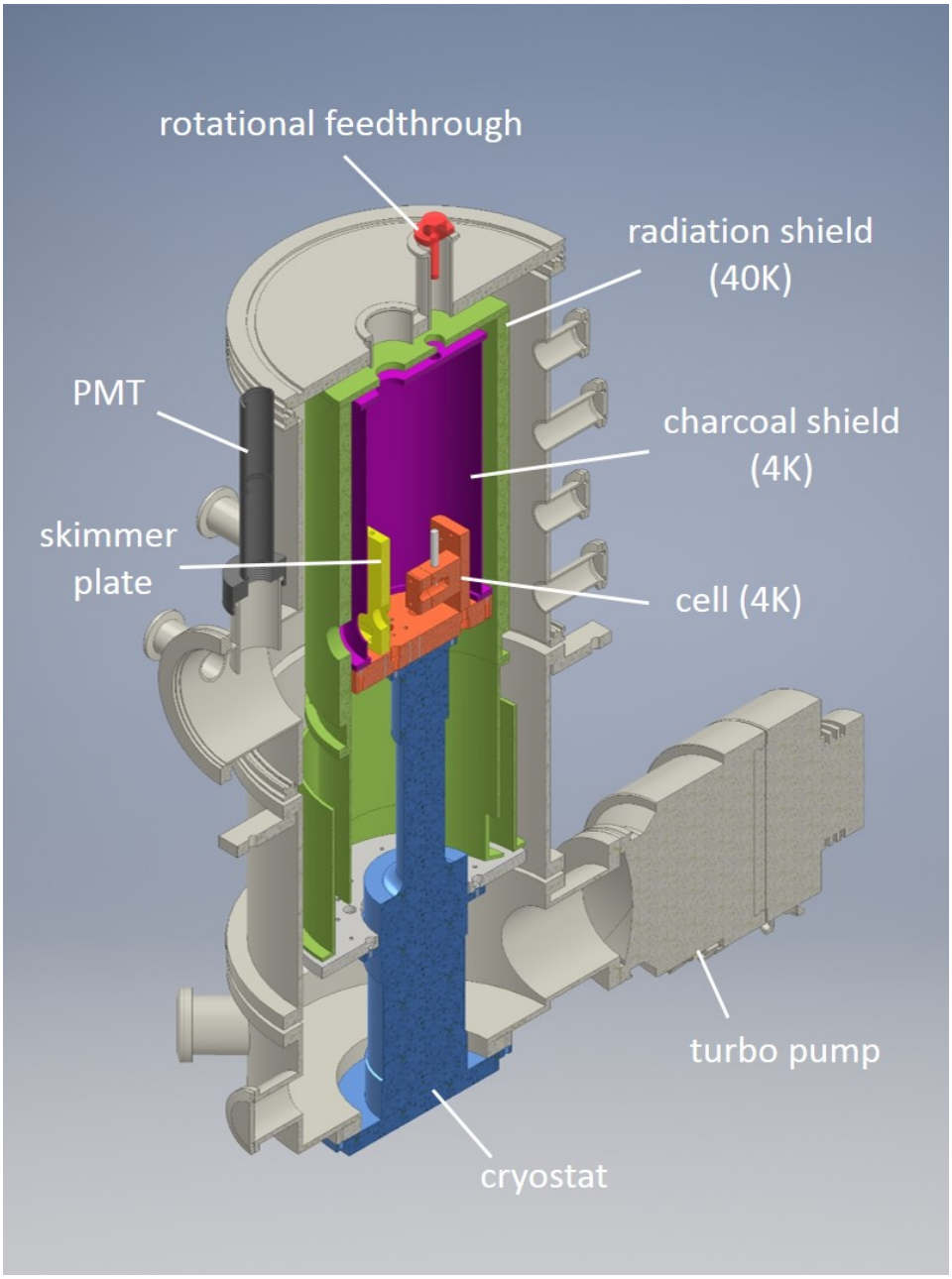

Figure 3.3: Illustration of the source chamber showing a cut through the centre of the apparatus. CaF molecules are produced in the buffer gas cell (orange), which is cooled to about 4.5 K by a cryocooler (blue). The cell is surrounded by a charcoal-coated shield (purple), which acts as a cryopump. An additional skimmer plate (yellow), which is also covered with charcoal, increases the pumping speed further. A radiation shield (green), connected to the second stage of the cryocooler at 40 K, shields the cell from black-body radiation. When the molecules exit the source chamber, they can be detected by laser induced fluorescence collected onto a photo-multiplier tube (black).

of diameter $d_s = 8$ mm is placed 30 mm from the cell aperture and increases the pumping speed further.

The use of charcoal sorption pumps is well known from fusion reactor research and can reach pumping speeds up to 6.7 l s^{-1}cm^{-2} [94]. Our charcoal shield[6] has a total area of $A_{\mathrm{ch}} \approx$1500 cm^2. Its pumping speed depends on the temperature, decreasing strongly when heated above 8 K. After running the experiment for a few hours, the charcoal shield fills up and the pumping speed decreases. It can however be regenerated by temporarily heating it up by a few tens of degrees. The typical background pressure in the source chamber with the experiment running at 1 sccm He flow is at about 2×10^{-7} mbar, which should give a sufficiently long mean free path. Indeed, we find the signal strength along the beam decreasing with only the geometrical $1/r^2$ factor but no additional attenuation.

The cell and the charcoal shield are protected from thermal radiation by a cylindrical aluminium shield ($A_{\mathrm{sh}} = 1600$ cm^2) which is mounted on the second stage of the cryocooler and cooled down to about 40 K. At this temperature the heating from thermal radiation of the shield $P_{\mathrm{sh}} = \epsilon\sigma_{\mathrm{SB}}A_{\mathrm{sh}}T^4$, with the Stefan Boltzmann constant σ_{SB} and the emissivity ϵ, is negligible with only $P_{\mathrm{sh}} \approx$0.03 W (assuming $\epsilon = 1$). A much larger contribution comes from the holes in the shield needed for the molecular beam, detection optics, the laser and the gas lines, which add up to an area of $A_{\mathrm{h}} = 17$ cm^2. Room temperature radiation can reach the cell through these holes and the heat load amounts to $P_{\mathrm{h}} \approx 0.7$ W.

Additional heating comes from the gas lines connected to the cell. They were empirically found to be heating the cell by about 0.5 K, which should correspond to roughly $P_{\mathrm{g}} = 0.5$ W heating power. Another heat source is the ablation laser which contributes (at most) a time-averaged power of $P_{\mathrm{l}} \approx 0.1$ W. The Ca rod is connected to the chamber via a rotational feedthrough, but any heat load due to that was avoided by heat-sinking the connecting rod to the 40 K stage and using PEEK as thermal insulator. Finally, the flow of buffer gas can add heat, although this was found to be negligible provided the gas is pre-cooled by connecting the copper gas line to the 40 K stage. All electrical wires going to the 4 K stage are thermally connected to the 40 K stage and were found to have a negligible effect too.

[6] see appendix B for details on the preparation

After all optimisation the cell temperature during the experiment[7] typically lies at about 4.5 K for the calculated heat load $P_{\text{total}} \approx 1.3$ W, which is quite close to the cryocooler's specifications of 4.2 K at $P = 1.5$ W.

3.2.3 Detection and velocity analysis

The CaF molecules are detected by collecting laser induced fluorescence (LIF) onto photo-multiplier tubes (PMTs) at different positions x along the beam (with $x = 0$ defining the aperture of the molecular source). The detection efficiency including the quantum efficiency of the PMTs[8] at $x = 53$ cm and $x = 130$ cm is 1.0%, while at $x = 2.5$ cm it is only 0.006% due to covering a smaller solid angle (see appendix A). The PMTs produce a current proportional to the incident photon rate, and an amplifier converts this to a voltage, which is recorded over time and called a time-of-flight signal (TOF). The calibration from this voltage to a photon count rate is $1.9 \cdot 10^7$ s^{-1}/V (see appendix A).

The probe laser addresses the $A - X(v = 0 \rightarrow v' = 0)$ P(1) transition at 606 nm and typically has a power of about 1 mW with a FWHM beam diameter of $d = 3.5$ mm. Light of other wavelengths (used for laser slowing) is filtered out by an interference filter[9]. The main probe frequency is modulated via EOMs and AOMs to produce three more sidebands (see section 5.4), so that the four hyperfine levels of the X state are addressed simultaneously. The angle between the probe beam and the molecular beam axis is either 90°, for Doppler-insensitive detection, or 60° for Doppler-sensitive detection (used to determine the velocity). The Doppler sensitive method is especially useful when the molecular beam is slowed down (see chapter 6), since the simple formula $v = x/t$ does not work at all in this case. For this reason we present the Doppler sensitive method here and confirm that $v = x/t$ describes the free flight case well.

Figure 3.4 (a) shows the time of flight LIF signals detected at $x = 2.5$ cm, 53 cm and 130 cm. At the first detector, right after the cell, the molecular pulse has a FWHM length of only 270 μs. This quick extraction from the cell is unusual for buffer gas sources and is probably due to our slightly smaller cell volume and our

[7] measured with calibrated thermocouples attached to the cell
[8] Hamamatsu R5929, quantum efficiency 9%@600 nm
[9] Semrock BrightLine bandpass filter FF01-593/40

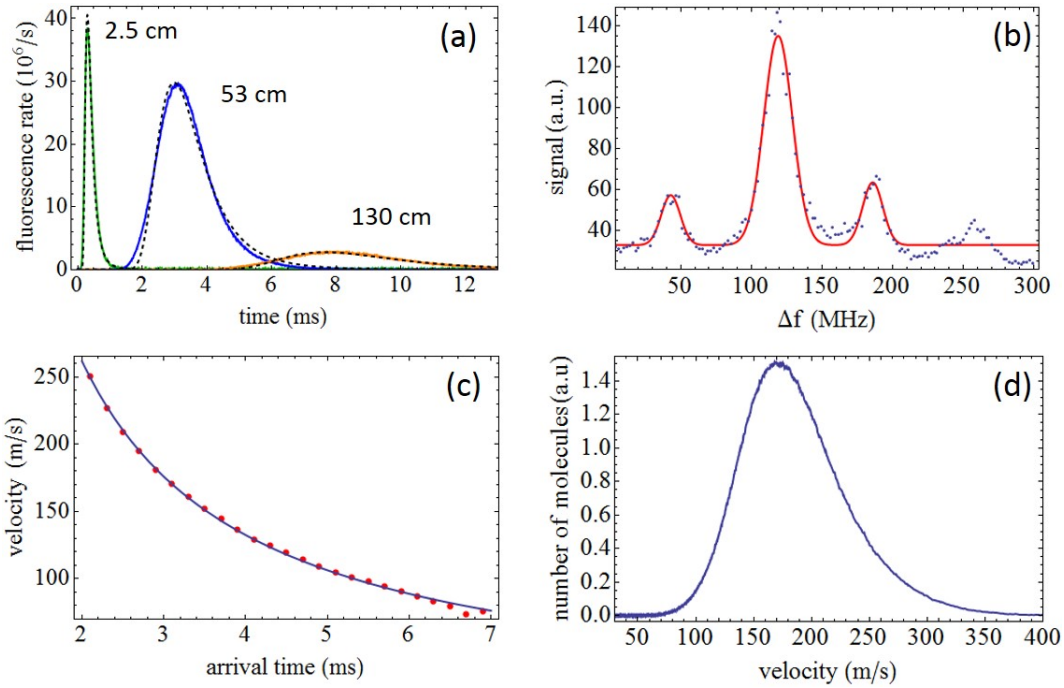

Figure 3.4: Detection and velocity analysis of the molecular beam. (a) Solid lines: Time of flight profiles of the molecular beam detected with PMTs at $x = 2.5$ cm (green), 53 cm (blue) and 130 cm (orange). The integrated signal at 2.5 cm is smaller than the others due to a smaller detection efficiency (see text). Dashed lines: Fit to the data (see text). (b) Laser-induced fluorescence as a function of probe laser detuning, with the probe beam at 53 cm and at an angle $\alpha = 60°$. The largest peak is obtained when all four hyperfine components are driven simultaneously. Several smaller peaks appear on both sides of the main peak when only some of the hyperfine components are driven. The data is binned to only include molecules arriving between 3.6 ms and 3.8 ms. The probe laser detuning $\Delta f = 0$ is defined as the centre position of the largest peak when measuring with an orthogonal probe beam. Points are data, solid line is a fit of a sum of three gaussians to the data around the main peak (leaving out the smallest peak). (c) Arrival time of the molecules vs velocity, which is determined from fits as in (b). Points are data, solid line is a fit (see text). (d) Velocity profile of the molecular beam at $x = 53$ cm, calculated by applying fit function from (c) to the TOF data in (a).

geometry with the angled He inlet. Typical extraction times of buffer gas sources in other groups lie between 1 and 10 ms, for example 2 ms reported for a beam of ThO [85]. The short pulses are advantageous for the chirp slowing method (described in section 6.4) because the whole molecular pulse can be addressed and slowed.

We can model the signal at the detector by assuming that the molecules leave the cell at the time $t = 0$ with a Maxwell Boltzmann distribution of velocities $f(v)dv = Av^3\exp(-m(v-v_0)^2/2k_BT)dv$. Here m is the mass of the molecule, A is a normalisation constant, T is the temperature and v_0 is the central velocity. This leads to a time dependent detector signal at the distance x from the source of the form [95]

$$h(t) = \frac{Ax^4}{t^5}\, e^{-\frac{mv_0^2}{2k_\mathrm{B}T}\left(\frac{(t-t_0)^2}{t^2}\right)} \tag{3.22}$$

with $t_0 = x/v_0$. The fits to this model work very well for all three TOF profiles (see the dashed lines in figure 3.4 (a)) and give a temperature of $T = 13.5 \pm 0.2$ K.

For spectroscopy measurements the frequency of the probe beam (with sidebands) is scanned over the four hyperfine levels of the X state in subsequent experimental shots. Integration of the recorded TOF signals gives the total amount of collected photons at each frequency. Figure 3.4(b) shows a typical spectrum obtained this way. Without sidebands, we would see only four peaks in the spectrum, corresponding to the four hyperfine levels. Adding the sidebands leads to a large peak in the centre, where all four laser sidebands are simultaneously resonant with the four hyperfine components. Additional smaller peaks appear where only some of the hyperfine levels are matched by the laser sidebands.

LIF measurements with a probe laser at an angle $\alpha \neq 90°$ to the molecular beam axis contain information about the particle's velocities. Due to the Doppler effect, faster molecules experience the partially co-propagating probe laser as further red detuned. This means that now a scan of the probe laser produces the sum of many spectra like the one shown in figure 3.4 (b), but each shifted in frequency relative to spectra from the perpendicular probe by the Doppler shift of the corresponding class of molecules with velocity v. We partition the TOF signals into time bins of 0.2 ms length and produce a spectrum for each of the bins. We determine the

relative frequency of the centre peak by fitting the spectrum to a sum of three Gaussians. This analysis gives the frequency difference between the Doppler-shifted and Doppler-insensitive spectra, Δf. From this we determine the mean velocity of the molecules in each time bin via $v = c\Delta f/(f\cos(60°))$. The result is shown in figure 3.4 (c). For our short molecular pulse, there is a strong correlation between the arrival time at the PMT and the velocity of a molecule, so we can equate the mean velocity of molecules in a time bin with their actual velocity (for more details see [82]). The relation between arrival time t and velocity v is well described by $v = x/(t - t_s)$, where x is the distance from the source to the detector and t_s describes the delay between the formation of the molecules and the time when they exit the source. The data shown in figure 3.4 (c) are taken at the middle detector at $x = 53$ cm. The fit gives $x = 53.6 \pm 0.5$ cm, confirming the measured detector distance, while the delay $t_s = -47 \pm 25$ μs is very close to zero, confirming quick extraction from the cell.

We use the fit parameters to determine the velocity profiles from the TOF profiles. The result for the same data is shown in figure 3.4 (d). The velocity profile peaks at 170 m/s and has a FWHM of 95 m/s.

3.3 Results

3.3.1 Pulsed helium flow

In our first experiments the He buffer gas was introduced into the cell through a pulsed solenoid valve in high pressure pulses of about 200 μs pulse length at 2 Hz repetition rate. This was done due to initial concerns about insufficient He pumping capacities for a continuous flow. The resulting molecular beam showed strong dependence on both the length of the gas pulse and its timing relative to the ablation laser pulse. Possibly due to this sensitivity on time scales of a few μs, which aren't controlled to this precision in our experiment[10], both velocity and intensity of the beam show a higher shot-to-shot variation than in later experiments with continuous He flow. For this reason, the continuous flow is preferred and used for all experiments in this thesis.

[10] the smallest unit of time we control is 2 μs

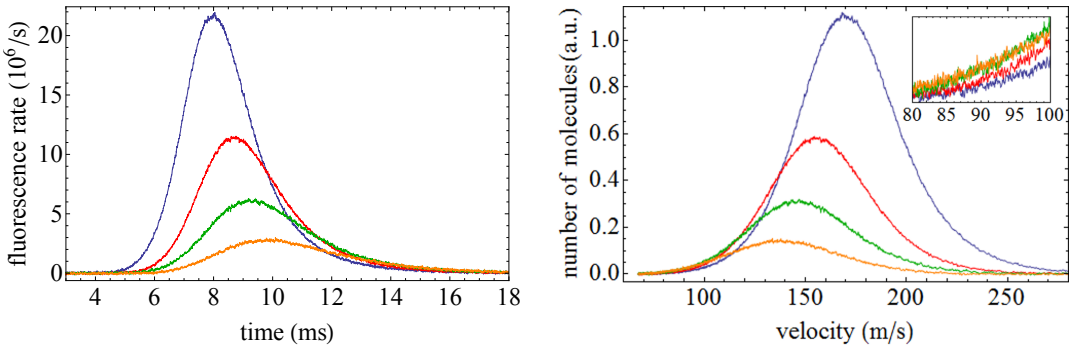

Figure 3.5: Left: Time of flight signal at $x = 53$ cm for various He flow rates (Blue: 0.3 sccm, red: 0.2 sccm, green: 0.1 sccm, orange: 0.05 sccm). Right: Corresponding velocity profiles.

3.3.2 Continuous helium flow

After the initial experiments we removed the solenoid valve and installed a flow controller for continuous He flow. The flow of SF_6 into the cell is controlled with a flow controller as well, but is kept at very low levels (0.01 sccm) and shows no strong influence on the molecular beam when varied. The velocity distribution in the beam depends crucially on the He flow, as shown in figure 3.5. A higher flow produces a higher molecule flux, but increases the centre velocity of the distribution. Looking only at the slow tail of the velocity distribution, the lower flow actually produces more molecules at these low velocities (see inset in the figure). However, since in chirp slowing we can sweep over a wide range of initial velocities, we prefer the larger total flux and settle on $F = 0.3$ sccm.

Another parameter which we find to have an influence on the TOF and velocity profiles is the position of the ablation spot. After turning the Ca target, the beam speeds up for a few shots at a higher beam intensity, but then settles at a lower speed and is remarkably stable over hours of continuous operation. Tweaking the position of the ablation spot by changing the alignment of the ablation laser has the same effect, but also influences the settled velocity profile. This might be due to changing the direction of the ablation plume towards the He flow or away from it, which influences the internal flow dynamics in the cell.

We have investigated different repetition rates of our experiment, in order to increase

the number of molecules per time. We find that at 5 Hz the beam is as stable as at 2 Hz, running for hours without much signal decay, but at a molecule flux which is smaller by a factor of about 2. Finally, at 10 Hz we observe a collapse of the fluorescence signal after a few hundred shots. It has been suggested that this might be due to heating the Ca target locally and changing the ablation conditions on the surface [90]. Molten layers of Ca could form, which could reduce the ablation of the solid metal beneath it. At lower repetition rates this doesn't occur because there is enough time for the metal to cool down in between shots. Since the number of molecules per second is roughly equal for 5 or 2 Hz and the source seems most stable at 2 Hz, this ablation rate is chosen. We have tried rotating the target during the experiment, but observed a decrease in signal stability, possibly due to the varying surface properties of the different ablation spots.

We can determine the number of molecules in the beam from the measured TOF profiles. We first use the calibration of the PMT (see appendix A) to turn the measured voltages into a detected fluorescence rate (as already done in the TOFs shown in this chapter) and then integrate the TOF profiles over time to get the number N_{ph} of detected photons per pulse. The number of molecules per pulse is then given by

$$N_{\mathrm{mol}} = \frac{N_{\mathrm{ph}}}{\eta p} \tag{3.23}$$

with the detection efficiency η and the mean number p of photons emitted by each molecule. The probe laser power of $P = 0.5$ mW was chosen such that the number of photons emitted per molecule is about $p = 1$ (see appendix A). With $p = 1$ and $\eta = (1.01 \pm 0.05) \times 10^{-2}$ (see appendix A), the blue TOF (at $x = 53$ cm) in figure 3.4 corresponds to $N_{\mathrm{mol}} = (5.8 \pm 0.3) \times 10^4$ detected molecules, or $(9.3 \pm 0.5) \times 10^{10}$ molecules per steradian per pulse (in the $N = 1$ rotational state).

3.3.3 Summary

In this chapter we have presented a cryogenic buffer gas source of CaF which is well suited for further slowing and trapping in a magneto-optical trap. The typical velocity of the molecules is 170 m/s, with a velocity width of 95 m/s corresponding to

a translational temperature of about 14 K. The molecule number is about 10^{11} sr^{-1} pulse^{-1} in $N = 1$. The source operates at 2 Hz repetition rate, shows remarkable stability over the day and needs no maintenance over months. These properties are all very advantageous for the further experiments presented in this thesis.

Chapter 4

Buffer gas beams for interferometry of biomolecules

The results of this chapter were produced between January and May 2015 during a secondment at the group of Prof. Markus Arndt at the University of Vienna. The main focus of this group lies in matter wave interference of large molecules. This chapter will explain how the interferometer works, why a buffer gas source would be beneficial for it and also present the setup and first results.

4.1 Motivation: A cold buffer gas source for Kapitza-Dirac Talbot-Lau Interferometry

It is not clear why we observe quantum effects like superposition only on the microscopic and low mass scale, while the macroscopic world around us seems classical. Some theories explain this by decoherence, while others predict a (often mass-dependent) collapse of the wavefunction, which makes quantum mechanics fail on the big scale [97].

One experimental approach to this question is to do interference experiments with increasingly massive particles. The *Quantum Nanophysics and Molecular Quantum Optics* group of Prof. Markus Arndt has several interferometers set up, one of which is a *Kapitza-Dirac Talbot-Lau (KDTL) interferometer* [98]. It consists of three gratings, two material gratings and one standing light wave grating in between them.

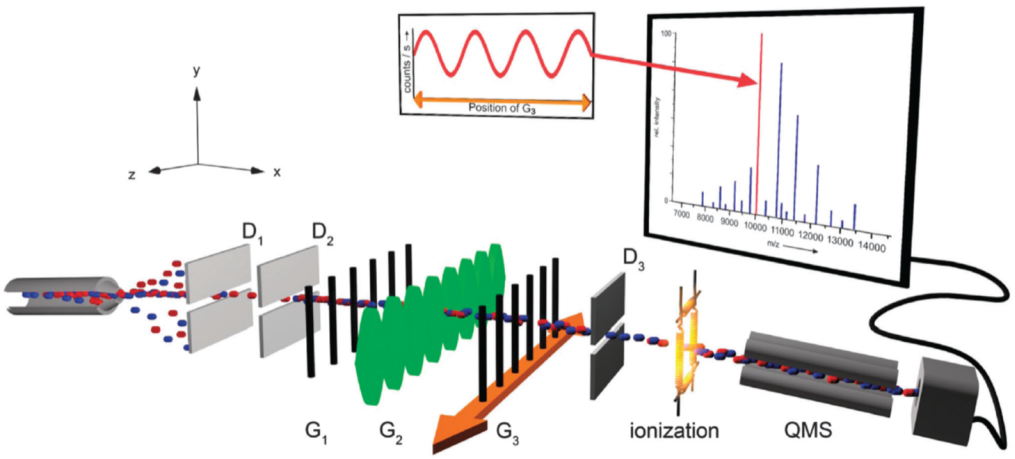

Figure 4.1: Setup of the Kapitza-Dirac Talbot-Lau interferometer (see text). Adapted from [96].

The optical grating avoids the coherence loss due to van der Waals interactions between molecule and grating material, which is a problem for high mass particles. The interferometer works in the near-field, which relaxes the collimation requirements of the molecular beam. More precisely, the distance between the gratings is chosen as a multiple of the Talbot length $L_{\mathrm{T}} = d^2/\lambda_{\mathrm{DB}}$ with the grating periodicity d and de-Broglie wavelength λ_{DB}. At these positions, the grating pattern is re-imaged by the Talbot-Lau effect [99, 100], as shown in figure 4.2.

The general setup is shown in figure 4.1. Molecules are heated in an oven to 500-1000 K and form a beam. Their forward velocity and with this their de-Broglie wavelength $\lambda_{\mathrm{DB}} = h/mv$ is selected by three horizontal slits D_1-D_3, defining a parabola in the gravitational field. The beam passes three gratings (G_1-G_3) of the identical grating period of $d = 266$ nm, positioned 10.5 cm from each other.

The first grating (G_1) is made of silicon nitride (SiN_x) and prepares coherence of the initially incoherent beam. It does this by restricting the molecules spatially to the width of the slit ($s = 110$ nm), which according to Heisenberg's uncertainty principle gives a transverse velocity spread of $\Delta v_x \approx \hbar/s$. The beam can now be understood as a number of elementary waves, spreading out and overlapping at the position of the second grating.

The second grating is created by focussing a single-mode laser beam onto a plane

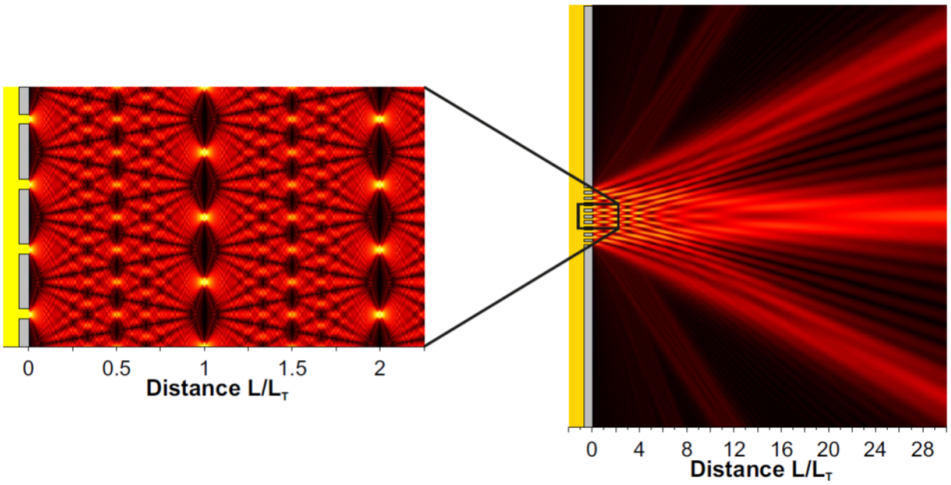

Figure 4.2: Talbot effect: the grating is re-imaged in the near field at distances multiple of L_{T}. In the far field we see the usual Fraunhofer diffraction. Adapted from [101].

mirror to form a standing wave of the same period d. The laser has a power of up to P=14 W (continuous wave) at the wavelength $\lambda_{\mathrm{g}} = 532$ nm with a linewidth below 5 MHz. The off-resonant light field acts as an optical dipole potential and introduces a phase shift

$$\Phi(z) = \Phi_0 \sin^2(2\pi z/\lambda_g)\,, \tag{4.1}$$

with amplitude $\Phi_0 \propto \alpha_\omega P$ proportional to the optical polarizability α_ω. This is known as Kapitza-Dirac effect [102].
The third grating is another SiN_x membrane and serves as a mask in front of the detector. It is translated perpendicular to the beam and determines which part of the sinusoidal interference pattern can reach the mass spectrometer.

The current setup works well and produced the record of the heaviest particle interfered up to date [96], so why do we need a new source? The answer to this question is actually two-fold. The main reason is that the KDTL interferometer is working close to the limit of the de-Broglie wavelength that it can possibly resolve (about 0.5 pm), due to its geometry. This means that if the particle mass should be in-

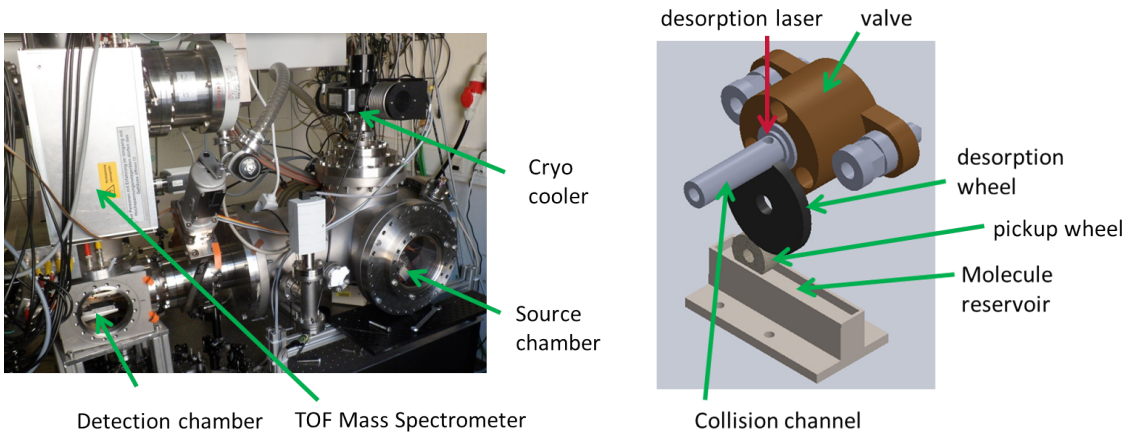

Figure 4.3: Left: Photograph of the preliminary setup. Right: Molecular source with collision channel. Translation and rotation mechanics not shown.

creased by another order of magnitude, the particle velocity has to be reduced by the same factor. Buffer gas sources are the obvious choice to do this.
The other reason is that it is not clear whether hot internal temperatures, e.g. of the vibrational and rotational degrees of freedom, reduce the coherence by radiation and giving which-path information. Unlike in the current hot source, a buffer gas source would produce internally cold molecules and possibly increase fringe visibility.

4.2 Preliminary setup: Pulsed supersonic beam with collision channel

As a first step towards a buffer gas beam source, a pulsed room temperature supersonic source was modified by adding a collision channel in front of the valve and cooling both to intermediate temperatures of down to 90 K by a Stirling cryocooler[1]. The collision channel is a copper piece with a cylindrical bore of 30 mm length and 4 mm diameter (see figure figure 4.3).
The whole setup is shown in figure 4.3. It consists of a source chamber and a detection chamber, separated by a skimmer of 2 mm diameter. In the source chamber, a powder of the molecule of interest is collected from a translatable reservoir onto

[1]Ricor K535, 7W@65K

a spinning felt wheel, and further onto a spinning desorption wheel made of glassy carbon. The carbon wheel absorbs laser radiation of 532 nm and 1064 nm very well and heats up, evaporating the molecules. This happens a few mm away from the aperture of an Even-Lavie valve [103] through which a carrier gas (usually argon) is introduced in high pressure (50 bar) pulses of about 20 μs length. The molecules are entrained in the carrier gas and form a beam, passing through the collision channel towards the detection chamber. There they are photo-ionised by a pulsed VUV laser[2] and detected in a time-of-flight mass spectrometer (TOF-MS). Unlike a quadrupole mass spectrometer (QMS), the TOF-MS works in a pulsed fashion, since it determines the mass (or rather mass-to-charge ratio) of the molecules by their time of flight between the point of ionisation, with immediate acceleration in an electrical field, and the detection of the ions. This way all different masses are measured simultaneously, instead of pre-selecting the mass-to-charge ratio one is looking for. It should be mentioned that while some molecules show fluorescence, the low number densities and a quick decay to other vibrational states make direct fluorescence detection in the gas phase infeasible. It is however possible to collect the molecules on a glass window and detect fluorescence there, as done with single molecule resolution in [104].

The velocity of the molecules is determined by measuring the time between desorption and ionisation, with a distance of 63 cm between source and detector. This method doesn't take into account possible delays due to diffusion in the collision channel, hence the actual velocity of the molecules could be higher than determined. However, the measured velocities at different temperatures fit well with theoretical predictions, so the delay should not be large. An additional mechanical chopper in the molecular beam could get rid of this uncertainty, but was not installed yet.

The dependence of the forward velocity on pressure behind the valve, temperature, valve pulse length and geometry of the collision channel was investigated. While cooling down the valve and collision channel decreases the velocity as expected (see figure 4.6), varying the pressure and pulse length didn't have a big influence. Doubling the length or diameter of the collision channel from its initial values $l = 30$ mm and $d = 4$ mm did not change the velocity much either.

[2] $\lambda = 157$ nm, 1.3 mJ pulses, 10 Hz repetition rate, F_2 eximer laser

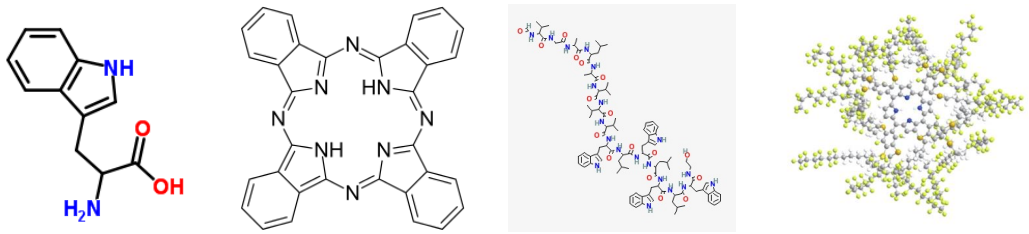

Figure 4.4: Left: Tryptophan (204 amu). Middle Left: Phtalocyanin (514 amu). Middle Right: Gramicidin A (1882 amu). Right: Fluorous porphyrin (10k amu), the current mass record in matter wave interferometry [96].

4.3 Testing molecules

When looking for a new molecule to use in a matter wave interferometer, several things need to be considered. First of all the molecule has to stay intact when being ablated. Next, there should be a way to detect it without fracturing it, as can happen during ionization for mass spectrometry. Finally it should have a high mass and a strong optical polarizability, which is crucial for the phase grating of the KDTL interferometer. Other properties like optical absorption cross sections and electric susceptibilities can then be measured by deflectometry in the interferometer [105, 106]. Another interesting question is whether the molecule forms clusters with either other molecules of the same species or for example with the buffer gas atoms. Before setting up the buffer gas source, several molecules were tested in the supersonic source. Most of them fractured in either ablation or ionization and were ruled out for interferometry. Other molecules like the amino acid tryptophan (204 amu) and the antibioticum gramicidin (1882 amu) worked well and were used as test molecules.

Finally, a different molecule that would break the mass record was found. Peridinin chlorophyll complex (PerCP), an important molecule in photosynthesis, has a mass of $m \approx 32$k amu and was desorbed without fragmentation. Unfortunately it could not be photo-ionised without breaking apart, but was instead identified after the experiment by doing matrix assisted laser desorption ionisation (MALDI) [107] of molecules deposited on a glass plate inserted into the beam path. PerCP is however known to emit fluorescence at $\lambda \approx 670$ nm when excited in the blue. For this reason,

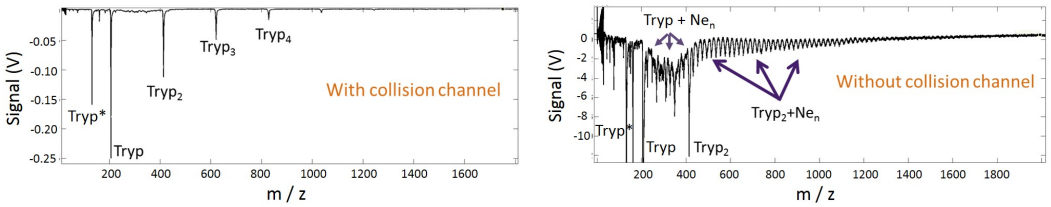

Figure 4.5: Left: Mass spectrogram of tryptophan with neon carrier gas through the collision channel. Tryptophan clusters form. The peak at 130 amu, labelled Tryp*, shows the main dissociation product of tryptophan. Right: Same experiment without the collision channel. We only see tryptophan clusters up to 2 molecules, however now neon attaches to them.

an additional fluorescence detection setup was built and will be integrated in the buffer gas source in the future (See chapter 4.4.3).

As seen in figure 4.5, we also observed clustering effects in the gas phase, which are generally not well understood yet. In the experiment, tryptophan was desorbed and entrained in supersonic pulses of room temperature neon. Depending on whether the collision channel was installed or left out, the mass spectrometry shows different clustering behaviour: With the collision channel up to 4 tryptophan molecules combine, while without it we see only one or two tryptophan molecules, which now have neon atoms attached. Adding the channel strongly decreases the signal strength, probably because it disturbs the formation of the translationally and internally cold supersonic neon beam in which the tryptophan molecules are entrained. Systematic investigations of the dependence on all external parameters like temperature and number density of the carrier gas would be interesting in their own right, but were not carried out due to limited time.

Figure 4.6 shows the long term stability of our source. It can be run continuously for several hours before having to refill the molecule reservoir, which is very convenient. In the same figure on the right we see time-of-flight measurements of gramicidin ($m_{\mathrm{G}} = 1882$ amu) in argon ($m_{\mathrm{Ar}} = 40$ amu) carrier gas, taken at different temperatures of valve and collision channel. As we are in the high pressure regime, we expect forward velocities near the supersonic speed of argon, $v = \sqrt{5k_{\mathrm{B}}T/m_{\mathrm{Ar}}}$. At the measured temperatures this predicts $v(300K) = 558$ m/s, $v(223K) = 481$ m/s

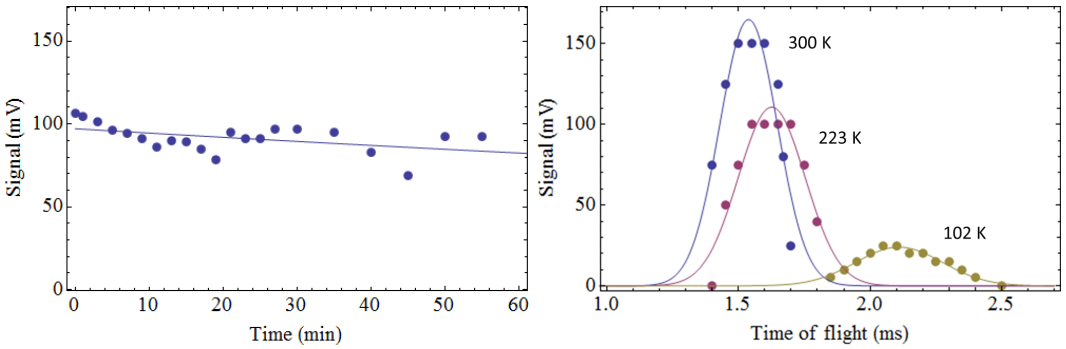

Figure 4.6: Left: Long term stability of the preliminary source. Right: Time of flight profiles of gramicidin with argon as carrier gas at different temperatures of the collision channel. The corresponding velocities are $v(300K) = 606$ m/s, $v(223K) = 559$ m/s and $v(102K) = 391$ m/s

and $v(300K) = 326$ m/s. The measured values are about 10-15% higher, possibly due to insufficient thermalisation of the gases with the collision channel and valve.

4.4 The buffer gas source

Since favourable molecules were identified and first cooling tests seemed promising, and due to the plan of preserving the preliminary setup for a different interferometer, it was decided to set up a completely new buffer gas experiment. This chapter will describe it and show the first results.

4.4.1 Setup

The general setup is shown in figure 4.7. As in the preliminary setup, molecules are delivered onto a glassy carbon wheel and desorbed by a laser. The desorption wavelength is $\lambda = 1064$ nm with either pulsed operation (10 Hz, 30-48 mJ per pulse) or with a quasi-continuous laser (P=6 W, 80 MHz). They then enter the buffer gas cell, where they are entrained in the buffer gas and sent through a skimmer (d=2 mm) towards the detection region. Depending on the molecule species they can be detected via fluorescence after deposition on a chamber window, or ionized in a quadrupole mass spectrometer. An additional velocity selector can determine the velocity spread, without relying on pulsed beam operation and time of flight

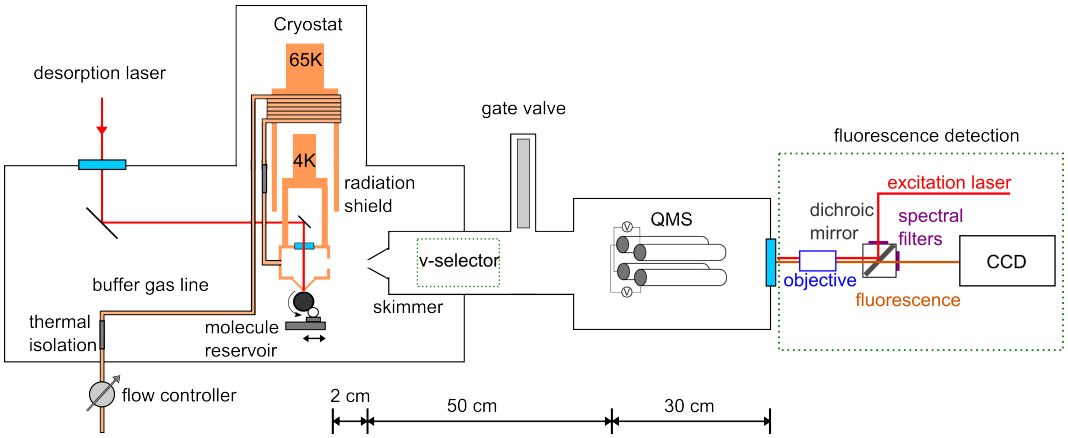

Figure 4.7: Sketch of the setup. The v-selector and fluorescence detection (green boxes) were set up but not used for the first experiments.

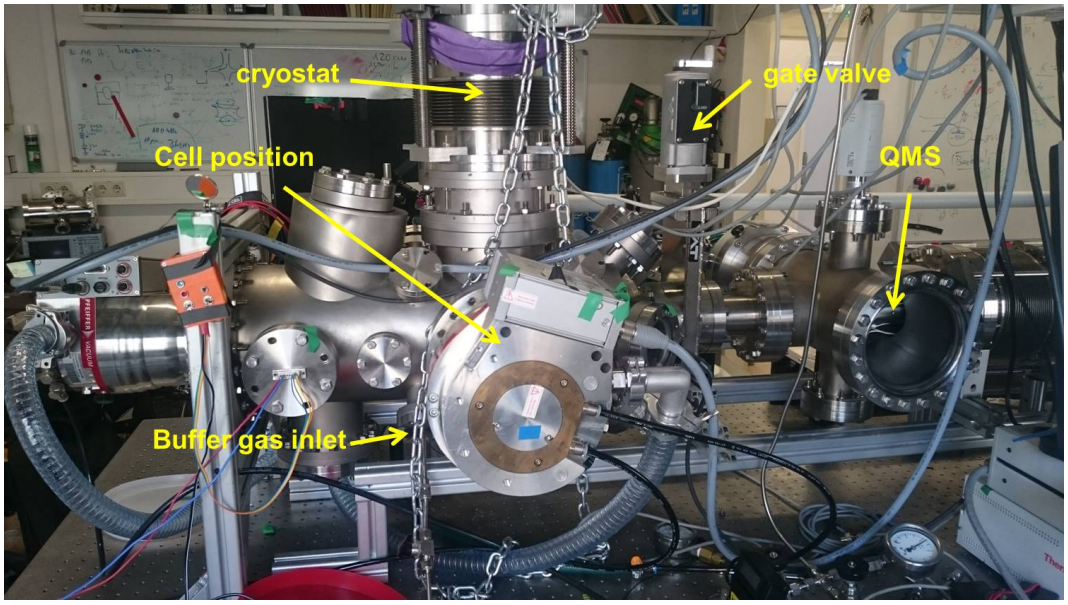

Figure 4.8: Photo of the buffer gas experiment set up during the secondment.

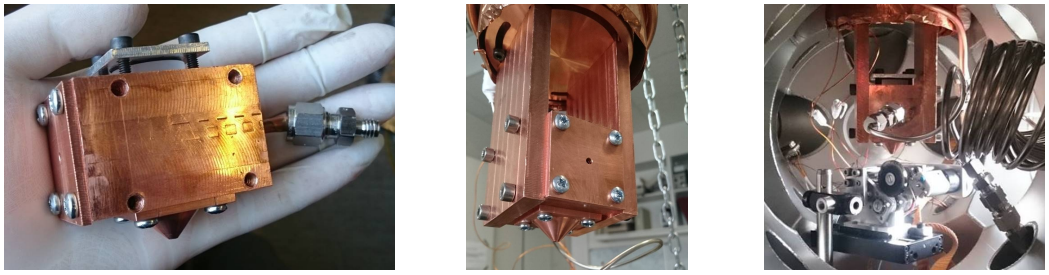

Figure 4.9: Left: The buffer gas cell. Middle: Cell mounted onto the cryostat. Right: Cell in chamber with carbon wheel.

measurement. The different parts of the setup are discussed in the following sections.

4.4.2 Cell design

As before, the buffer gas cell is mainly a copper block with a cylindrical bore (see figure 4.9). This time the buffer gas is inserted from the back for simplicity. The cell's dimension is 40 × 40 × 60 mm, while the bore has a diameter of 30 mm. On the top of the cell is a window for the ablation laser, which passes through the cell onto the carbon wheel. The wheel is set back slightly by a copper cone with a 4 mm aperture. The cone was initially designed to minimise gas leaks by bringing it very close to the wheel, it should however also be tried to bring the wheel into the cell directly. The cell is mounted on both sides to 10 mm thick copper plates, which connect it to the cryocooler[3]. There is a radiation shield connected to the 65 K stage, but it only shields the upper parts of the cryostat. This was enough to reach a temperature of 12 K, which is sufficient when using neon as a buffer gas. If in the future He should be preferred, the shield can easily be extended to cover the buffer gas cell too.

With a circular aperture of 9 mm diameter and 10 sccm neon flow rate, the number density in the cell should be $n_{cell} \approx 1.4 \cdot 10^{15}$ cm^{-3}, not taking into account the small losses through the ablation cone. This is about equal to the density in the CaF experiment in London. The values of extraction efficiency and Reynold's number of the cell depend on which molecular species is used and have an uncertainty due to not always well known collisional cross sections. The best approximations are

[3]Sumitomo SRP-062, 0.5W@4.2K, 30W@65K

molecule	m (amu)	σ (cm^2)	λ_{cell} (mm)	L$_{th}$(mm)	Re	γ	λ_{ch} (mm)
tryptophan	204	1×10^{-14}	0.21	5.1	85	0.75	250
phthalocyanin	514	2×10^{-14}	0.07	3.7	259	1.5	80
gramicidin	1882	4×10^{-14}	0.02	3.4	993	3.0	21
PerCP	3.2×10^4	64×10^{-14}	0.0003	1.7	32k	48	0.3

Table 4.1: Properties and calculated characteristic numbers for different complex molecules, including mass m, collisional cross section σ, mean free path in the buffer gas cell λ_{cell}, thermalisation length L_{th}, Reynolds number Re, characteristic number for extraction γ and mean free path in the source chamber λ_{ch}. The calculations assume 10 sccm neon flow through a 9 mm aperture at 20 K with cell length $L =$ 30 mm (distance ablation to aperture). Mean free path in source chamber before the skimmer assumes $p = 5 \times 10^{-5}$ mbar. Due to badly known collisional cross sections, values should be understood as an approximation of the order of magnitude.

summarised in table 4.1. It is interesting that while the heavier molecules need a higher number of collisions to thermalise, their increased collisional cross section more than compensates for this and leads to shorter thermalisation lengths. For the heavier molecules the flow should probably be reduced if effusive behaviour is aimed at. This will also decrease the pressure in the source chamber from the current value of $p = 5 \times 10^{-5}$ mbar for 10 sccm neon flow and allow the molecules to reach the skimmer without collisions (see mean free path lengths in table 4.1). A charcoal shield could be installed for that purpose too. After the skimmer the pressure is below 1×10^{-6} mbar, which is also crucial to not damage the mass spectrometer.

4.4.3 Detection

A mass spectrometer is the ideal detector for beams of complex molecules, since its mass selectivity leads to high signal-to-noise ratios and allows to check whether a particle has been fractured, or clusters together with other particles. As discussed in chapter 4.3, the necessary ionization does not work for every molecule without fragmentation, but nevertheless it is useful for first tests and characterisations of the source. It was decided to use a quadrupole mass spectrometer (QMS) instead of the previous time-of-flight mass spectrometer (TOF-MS), since the QMS detects continuously instead of in a pulsed fashion, given that the ionization is continuously applied. This is also the reason for using electron impact ionization (ESI) of the

built-in filaments of the QMS instead of photo-ionizing with a pulsed laser. Installing continuous detection is necessary when running the molecular beam continuously by desorbing with a quasi-cw laser (see chapter 4.4.5). Continuous operation of the beam is advantageous for higher count rates once the source will be integrated into the KDTL interferometer.

For molecules which can't be ionized without fragmentation, such as PerCP, a fluorescence setup was built (see figure 4.7). It excites molecules that are deposited on the inside of a window in the back of the chamber. The fluorescence light is collected with a microscope objective (magnification 20), separated from the excitation laser by a dichroic mirror and spectral filters, and sent onto a CCD camera[4]. While a test slide with phtalocyanine was successfully imaged with this setup, the molecular beam was not yet detected this way.

4.4.4 Helical velocity selector

Matter wave interferometry benefits from a thin velocity distribution of the particles, since the velocity determines their de-Broglie wavelength and hereby their diffraction behaviour. One solution is to use a helical velocity selector [108] as shown in figure 4.10. It is a cylinder with angled grooves through which the molecules are flying while the selector is rotated. The rotation speed determines which velocity class will pass it undisturbed, while too slow or too fast particles are hit by the selector and removed from the beam. The center velocity that can pass the rotating selector of length L, rotation frequency $\omega = 2\pi f$ and angle Φ of the grooves is

$$v_0 = \frac{L\omega}{\Phi}. \tag{4.2}$$

The velocity resolution is determined by the width of the grooves, described by the angle Ψ (see figure 4.10), and given as[109]

$$\sigma = \frac{\delta v}{2v_0} = \frac{v_{max} - v_{min}}{v_0} = 2\frac{\Psi/\Phi}{1 - \Psi^2/\Phi^2} \approx \frac{\Psi}{\Phi} \tag{4.3}$$

[4] Andor SCMOS Neo 5.5

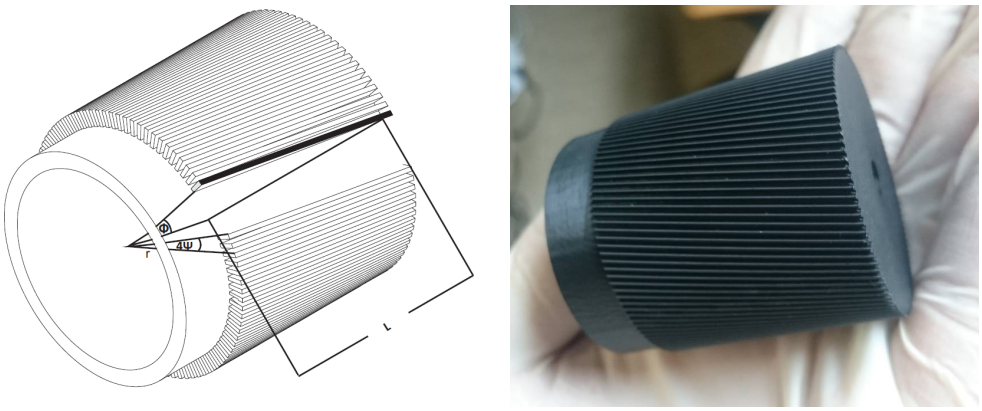

Figure 4.10: Left: Helical velocity selector. Right: 3D-printed selector made of plastic (ABS M30).

The selector was designed to transmit molecules of $v = 200$ m/s at the rotation speed $\omega = 100$ s^{-1}. It was 3D-printed with a length of $L = 40$ mm and only 50 g weight and should be reasonably stable. Alignment to the molecular beam by a laser is made possible by a single straight cut through the otherwise angled grooves.

4.4.5 Results

As the first test of the buffer gas source, gramicidin was ablated with the pulsed YAG laser into the room temperature cell. The aperture diameter was 6 mm and 10 sccm of neon served as carrier gas. Figure 4.11 shows the result of running the source continuously for 15 minutes. The front plate around the aperture is covered with a layer of gramicidin, but a spot next to it is uncovered, possibly cleaned by the gas flow after the ablation was stopped. The picture next to it shows a glass plate that was inserted into the beam axis about 3 cm away from the aperture. We see gramicidin molecules, as later confirmed by mass spectrometry of the deposited powder, in a central spot and a less clearly visible ring around it. The reason for this peculiar pattern is not clear and should be investigated by numerically simulating the buffer gas flow. The molecule deposition was also seen with the cell cooled down to 12 K.

Next, it was tried to get quantitative information of the number of molecules in the beam while it was running, so that the dependence of parameters like gas flow and

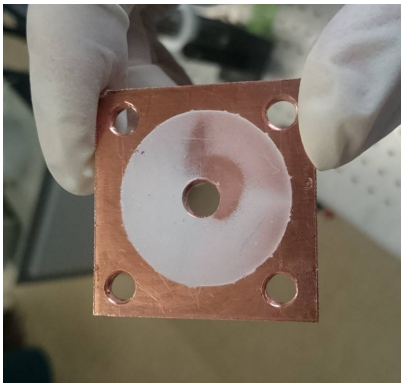
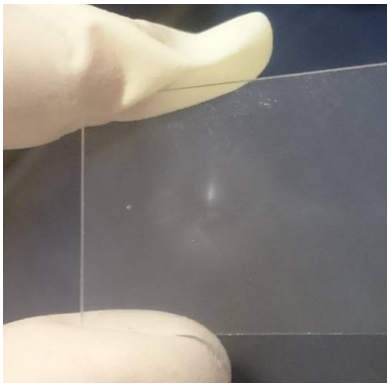

Figure 4.11: Left: Gramicidin deposited inside the cell around the aperture. Right: Gramicidin collected on a glass plate inserted into the beam, 3 cm away from the aperture.

laser could be investigated. A high precision scale[5] was inserted instead of the glass plate and showed a weak mass change rate, but the results were not conclusive and close to the resolution limit of the scale.

Consequently the QMS was built in and aligned to the skimmer and cell with a laser beam. The mass spectrometer was first tested and its parameters optimised by detecting toluene (92 amu), which was injected into the chamber via a fine control valve. The most critical parameter here is the voltage of the dynode, which attracts the positive ions and produces secondary electrons, which are then measured on the channel plate.

Finally the molecular beam was run at room temperature, looking for a first signal at the QMS. After no signal was found with gramicidin, phthalocyanin (514 amu) was used and showed a small peak in the spectrometer at a mass of around 500 amu, which is inside the calibration error range of the QMS from the expected value of 514 amu. The peak was even better visible when the ablation was done quasi-continuously with the 60 MHz laser (see figure 4.12). For this experiment the distance of the 2 mm skimmer to the cell aperture was reduced from 4 cm to 2 cm and the diameter of the cell aperture was increased to 9 mm, which should have increased the extraction efficiency.

These mass spectrometer measurements were done in the last week of my stay in

[5]inficon deposition controller xtc 2

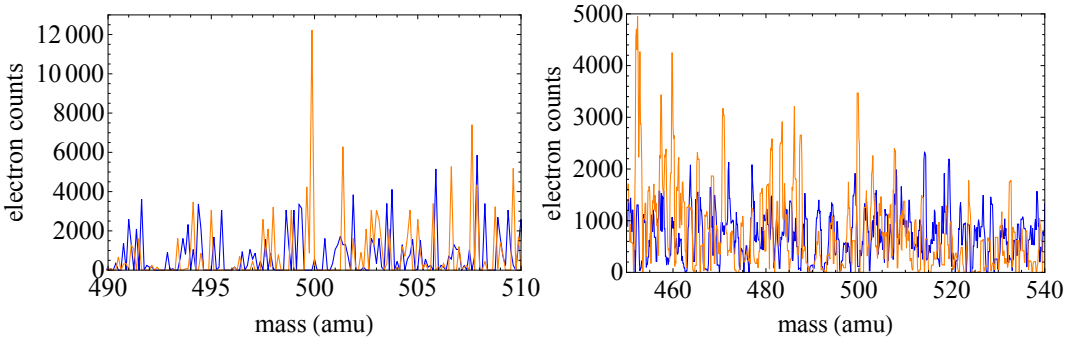

Figure 4.12: Left: Mass spectrogram of a phthalocyanin beam with continuous ablation (orange) and background measurement with closed gate valve (blue). The peak at 500 amu should correspond to phtalocyanin. Right: Zoom out of the same data shows additional peaks, possibly from fragmented phthalocyanin molecules. A moving average of 5 was applied for better visibility.

Vienna, so unfortunately there was no more time for optimising all parameters, especially the alignment, or to build in the helical selector for velocity measurements.

Chapter 5

Optical setup for laser cooling and trapping of CaF

5.1 Requirements

Laser cooling of CaF molecules requires good control over a large number of lasers: One cooling laser and 3 repump lasers for the MOT itself, and two additional lasers for radiation pressure slowing (see table 5.1). All laser frequencies need to be controlled, ideally by locking them to a stabilised reference laser. This complexity calls for a highly stable, low maintenance laser system and optical setup, with a minimum amount of re-aligning or other daily tweaking measures.

Laser	transition	purpose	λ (nm)	Power per beam in chamber (mW)
$\mathcal{L}_{00}$	A-X(v=0→v=0)	MOT cooling	606.3	80
$\mathcal{L}_{10}$	A-X(v=1→v=0)	MOT repump	628.6	100
$\mathcal{L}_{21}$	A-X(v=2→v=1)	MOT repump	628.1	10
$\mathcal{L}_{32}$	A-X(v=3→v=2)	MOT repump	627.7	0.5
$\mathcal{L}^s_{00}$	B-X(v=0→v=0)	laser slowing	531.0	100
$\mathcal{L}^s_{10}$	A-X(v=1→v=0)	laser slowing	628.6	100

Table 5.1: Summary of lasers needed for MOT and laser slowing.

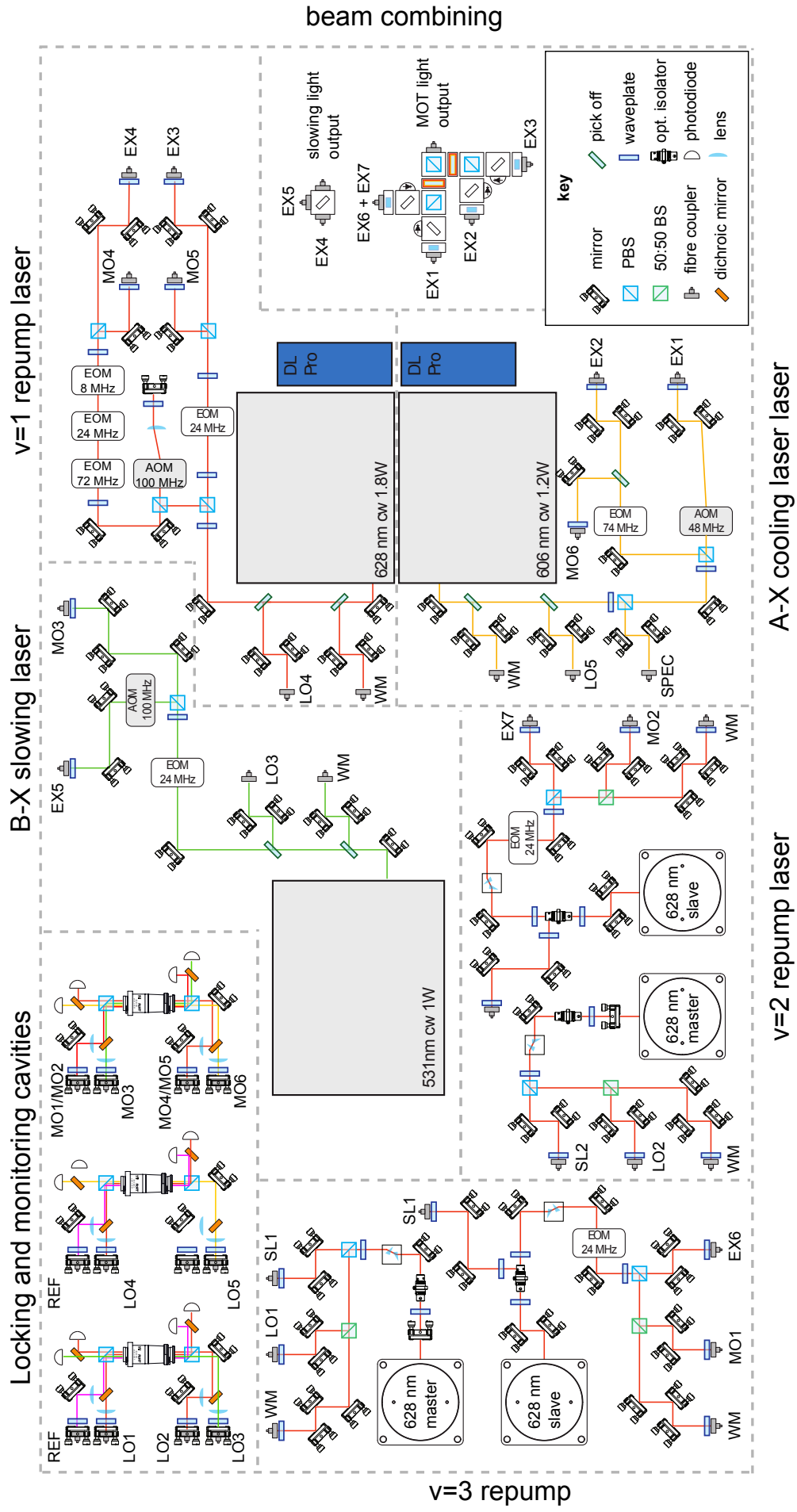

Figure 5.1: Layout of the optical setup. Fibre ports are labelled as LO (for locking), MO (monitoring sidebands), WM (to wavemeter), SPEC (for spectroscopy), SL (for injection locking) and EX (going to the experiment after beam combining).

5.2 Overview of the setup

The layout of our optical setup (excluding the reference laser, see section 5.6) is shown in figure 5.1 and will be explained in detail in the next sections. There are 5 lasers: 3 commercial fibre amplified diodes and two injection locked diodes. Free-space beam paths are kept as short as possible by using optical fibres, which also allows quick realignment after replacing faulty lasers. All laser light is treated with the same principle:

- A small fraction is sent via an optical fibre to a transfer cavity, which is used to lock the laser frequency relative to that of a stable reference laser.
- Another small fraction is sent via fibre to the wavemeter.
- The main beam is modulated via AOMs and EOMs to create the required sidebands (see section 5.4), and then coupled into a fibre. An additional AOM can serve as a fast switch to turn the light on or off.
- There are additional pick-offs for spectroscopy of the molecular beam and monitoring the power distribution in the sideband spectrum.
- The frequencies for the MOT and the slowing are each combined into a single polarisation maintaining fibre (see chapter 5.5) for perfect overlap. This reduces the available laser power but allows decoupling the MOT and slowing light alignment from the rest of the optical setup.

The described setup needs very little maintenance, except for optimising fibre coupling once a week and replacement of cheap diodes in the injection locking setup, which have a lifetime of about half a year [1].

5.3 Laser System

5.3.1 Replacing dye lasers

At the beginning of this PhD most of the laser light for laser cooling and detection of CaF was produced by dye lasers. While this allowed the first demonstration of

[1] Quote from one of our providers of laser diodes: "All diode lasers fail. It is not a question of if but of when."

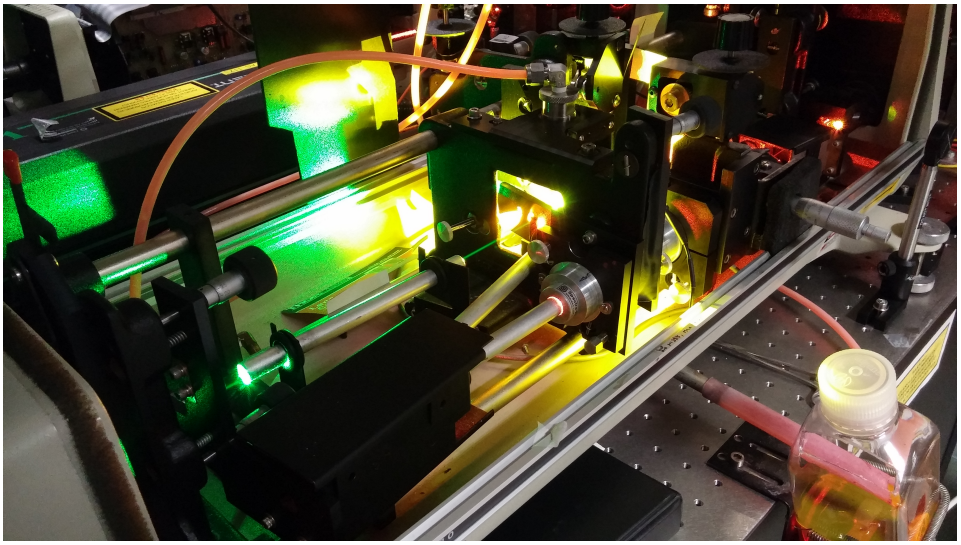

Figure 5.2: Picture of one of the dye lasers used in previous experiments.

longitudinal slowing and cooling [56], dye lasers have several disadvantages: Most importantly, they need regular dye exchanges and other maintenance such as realigning of the laser cavity, especially if they are run at their maximum power. While dye lasers can have output powers above 1 Watt, our laser (shown in figure 5.2) typically produces about 100 mW, which is factor 10 less than the fibre amplified lasers introduced later in this chapter. Further, the dye itself, usually Rhodamin 6 G for wavelengths around 606 nm, is classified as hazardous when ingested or in contact with the eyes, and has to be handled with care. Due to all of these reasons during this PhD the whole laser system was changed to solid state lasers and fibre amplifiers, ranging from low maintenance home-made diode lasers to turn-key commercial systems consisting of diode lasers with fibre amplification. The stability and reliability of these lasers is crucial to the results achieved in this thesis, and will be described in the following sections.

5.3.2 Diode lasers

Principle of diode lasers

Diode lasers are electrically pumped semiconductor lasers. The gain medium consists of several layers of semiconductor material which can be positively (p-type) or

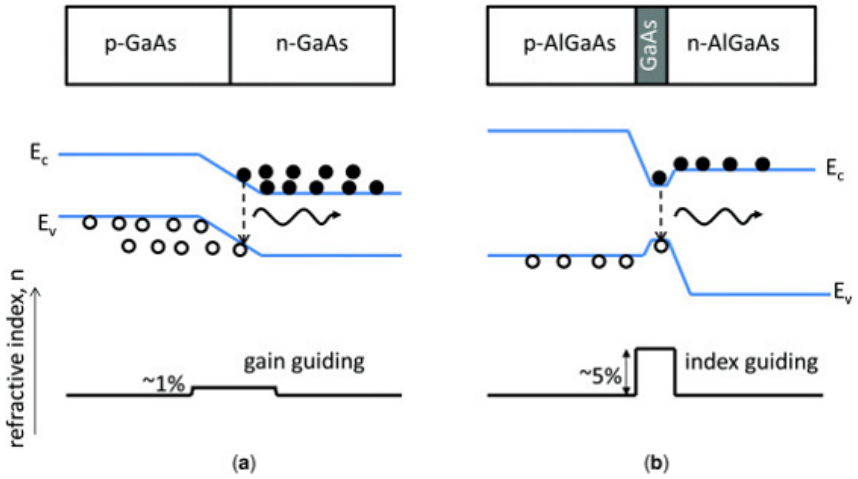

Figure 5.3: Principle of diode laser operation [110]. (a): Homojunction (GaAs - GaAs). (b): Double-heterojunction (AlGaAs - GaAs - AlGaAs). See text.

negatively (n-type) doped. The simplest design is a p-n homojunction, where differently doped layers of the same material are brought in contact (see figure 5.3 a). A more common design uses a double-heterojunction, which means a semiconductor with a smaller band gap is placed between an n-type and a p-type layer of a second semiconductor with a higher band gap (see figure 5.3 b). The inner layer represents the active region where electrons in the conduction band combine with holes in the valence band to emit photons in spontaneous or stimulated processes.
The population inversion necessary for lasing operation is created by applying a voltage between the outer layers, which excites electrons to the conduction band. The double hetero-structure increases the carrier density in the active region and allows lower lasing thresholds. The outer layers also act as a wave guide for the photons due to a lower refractive index. The laser cavity is often formed by the highly reflective end facets of the semiconductor. The emitted beam is highly divergent (especially in one dimension) and has to be collimated.

The frequency of a laser diode is mostly determined by its choice of semiconductors and the resulting band gaps, but it can be tuned slightly in various ways [111]. First of all, the temperature influences the wavelength by two different means: a higher temperature leads to an elongation of the laser cavity consisting of the end

facets of the semiconductor, changing the standing wave condition to higher wavelengths. Secondly, an increase (decrease) in temperature shifts the whole gain curve to longer (shorter) wavelengths as well. The shift of the gain curve is usually much faster than the frequency shift of the allowed modes due to the cavity length. Therefore heating or cooling the diode leads to so called mode hops. These are sudden frequency changes that occur when the gain of one mode allowed by the laser cavity becomes bigger than the gain of the neighbouring mode. The mode spacing is given[2] as $\delta\nu = c/2nL$ with the cavity length L and the refractive index n. The resulting frequency dependence on temperature has the form of a staircase with sloping steps. The temperature of a diode also influences the laser threshold, shifting it to smaller values when it is cooler. Therefore, at a fixed current, colder diodes will have a higher output power.

Another way to tune the laser frequency is by the injection current, which of course also determines the output power. A higher current means a higher carrier density inside the semiconductor, which increases its refractive index. This in consequence increases the optical path length of the internal cavity, leading to higher wavelengths again. As a side effect, a higher current also heats the diode further, increasing the wavelength even more.

The last method to tune the wavelength and more importantly achieve single longitudinal mode lasing is to install an external cavity, as will be explained in the next chapter.

Home-made External Cavity Diode Laser (ECDL)

The output of a laser diode often consists of several frequency components due to competing longitudinal modes within the gain curve. This multimode behaviour can be avoided and a single longitudinal mode can be selected via frequency dependent feedback into the laser. A common way to do this is by adding an external resonator in the form of a reflection grating. In the so called Littrow-Configuration [112], the minus first diffraction order of the laser beam is retro-reflected into the diode and provides the feedback, while the zero-th order presents the output of the resonator

[2]The mode spacing actually depends on the resonator geometry. While the given formula is correct for planar resonators, in the often used confocal geometry it is $\delta\nu = c/4nL$.

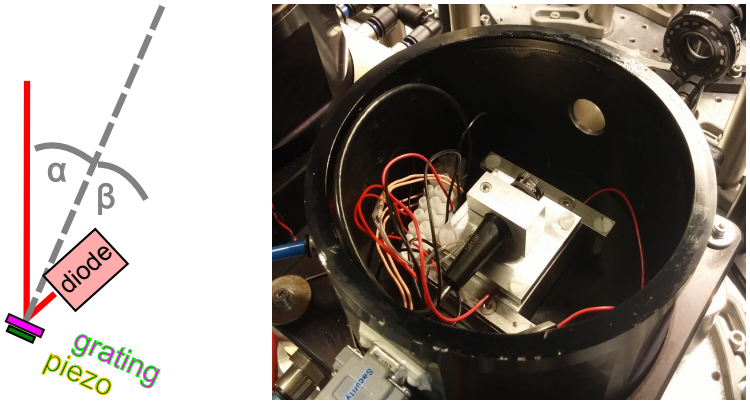

Figure 5.4: Left: Schematic drawing of the external cavity diode laser in Littrow configuration. The laser beam (red) is reflected in first order by the grating (pink). Right: Photo of a slave laser setup.

(see figure 5.4). The wavelength selectivity is given by the grating equation

$$d(\sin\alpha + \sin\beta) = m\lambda$$

with the wavelength λ, the diffraction order m, the line spacing d of the grating and angles of the incident and reflected beam α and β respectively. In Littrow configuration we have $\alpha = \beta$ for the first order diffraction (m=1). This means the desired wavelength of the feedback light can be chosen by the grating angle. The spectral width of the diffracted light at a certain angle depends on the line spacing, since it increases the number N of illuminated slits and thereby the wavelength resolution $\lambda/\Delta\lambda = mN$.

In addition to selecting the wavelength by diffraction, the grating also represents a second cavity with a standing wave condition. This can be used to precisely tune the frequency by mounting the grating on a piezo actuator, which varies the resonator length depending on the applied voltage.

The ECDL set up as a repump for the $v = 2$ vibrational state ($\mathcal{L}_{21}$) uses a grating with 1200 lines/mm, which is glued onto a piezo actuator and mounted onto a mirror mount. Since at the time there were no diodes specified to run at room temperature at the desired wavelength of 628 nm, a laser diode[3] specified for 637 nm was cooled to

[3]HL 63133 DG, Thorlabs

about $-20°$ C in a two-stage peltier setup[4] placed on a water-cooled aluminium base (see figure 5.5). The upper stage peltier element is connected to a P-I-controller[5], which gets feedback from a thermistor and provides temperature stability up to 10 mK on the time scale of seconds. To avoid condensation of humidity the diode is set under vacuum (< 1 mbar). The grating angle can be changed from outside the vacuum via a mechanical feedthrough.

5.3.3 DBR laser

In parallel to developing the ECDL, a commercial DBR-RW (distributed Bragg reflector-ridge waveguide) laser was purchased[6]. In this laser the light is guided inside a sharp ridge, where it is confined by a step in refractive index. At the end of the guide the light is reflected at a distributed Bragg grating, which also acts as a longitudinal mode filter.

Due to higher reliability and less required maintenance the DBR laser eventually replaced the home-made ECDL setup for both the $v = 2$ and $v = 3$ repump frequencies. The laser works near room temperature, although it needs temperature stabilisation as well. The output power is up to 20 mW, enough for seeding the slave diode, and the linewidth is about 100 kHz.

5.3.4 Injection locking

The output power of a laser diode is reduced by an external cavity. One way to obtain more laser power is the use of the injection locking method, often also called a master-slave system. In this setup one laser (the master) is carefully frequency stabilized and a part of its light is injected into the second diode (the slave) via the polarizing beam splitter of an optical isolator. This forces the slave diode to run at exactly the same frequency. This way a higher power laser can be seeded without its own active frequency stabilization. Our master-slave setup is depicted in figure 5.6.

The diode used for the slave laser is the same as in the ECDL setup. As explained before, it has to be cooled to about $-20°$ C to reach the right wavelength. It is

[4] two peltiers RS 490 1367 for the lower stage and a single RS 490 1266 for the upper stage
[5] wavelength electronics, MPT 2500
[6] laser provided by the Ferdinand Braun Institute, Berlin

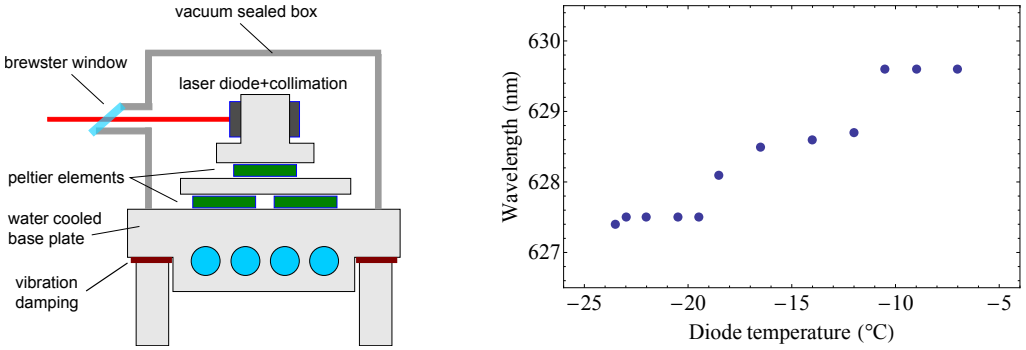

Figure 5.5: Left: Laser diode cooling setup consisting of two stages of peltier elements on a water cooled base plate and vacuum sealed. Right: Wavelength behaviour when diode is cooled down shows steps as predicted.

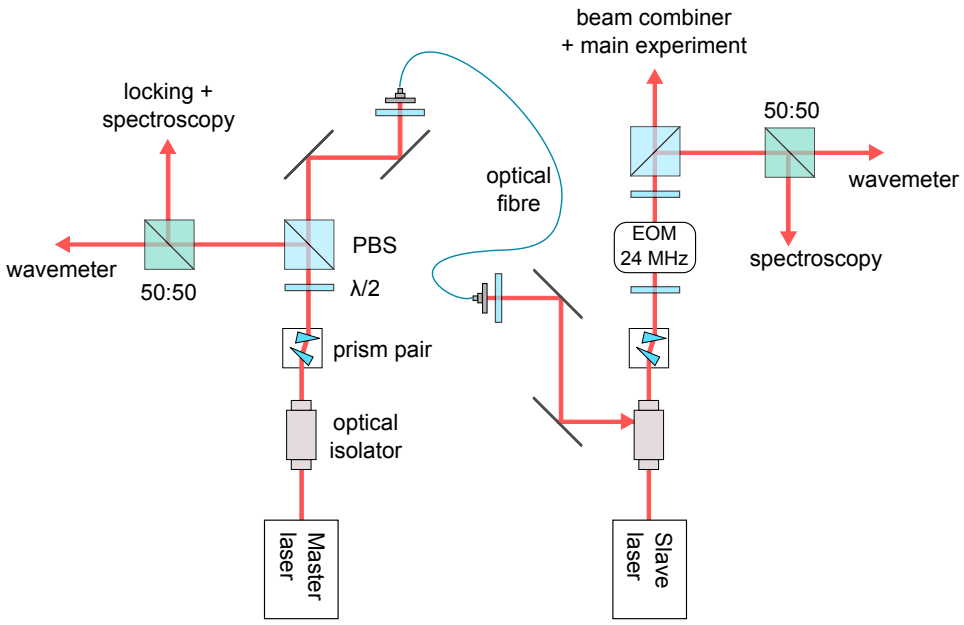

Figure 5.6: Scheme of the injection-locking setup for the repump laser diodes.

injected with 2 mW seed power and the output power is about 100 mW, which is more than sufficient for repumping higher lying vibrational states.

5.3.5 Fibre amplifiers

One downside of laser diodes is their often limited maximum power. Fortunately there are ways to amplify the output of a laser diode, while maintaining their other favourable properties. Optical amplifiers can be thought of as a lasers without a cavity: The light passes through a gain medium only once while being amplified. The most common optical amplifiers are tapered amplifiers (based on semiconductors) and fibre amplifiers, which can be based on Raman scattering or stimulated emission in doped fibres. We use both types of fibre amplifiers in our experiment.
Both the cooling ($\lambda_{\mathcal{L}_{00}} = 606$ nm) and the first repump laser light ($\lambda_{\mathcal{L}_{10}} = \lambda_{\mathcal{L}^s_{10}} = 628$ nm) is produced in the same way: Infra-red diode lasers[7] at wavelengths of 1212 nm and 1256 nm are each amplified by a Raman fibre amplifier[8]. In a Raman amplifier, which is optically pumped by diodes of wavelength λ_{pump}, an incoming photon from the seed laser (at λ_{seed}) will trigger stimulated Raman emission of a Stokes photon with $\lambda_{\text{stokes}} = \lambda_{\text{seed}} > \lambda_{\text{pump}}$. The difference in energy between pump and Stokes photon is dissipated in form of a phonon, and eventually heat.
After amplification up to 7 W, the infrared light is frequency doubled in a nonlinear crystal to the final wavelengths at output powers of 1.8 W (repump) and 1.2 W (cooling laser). The linewidth is below 1 MHz and the mode-hop free tuning range is 30 GHz. The higher power of the repump laser allows using it for the MOT and the laser slowing simultaneously. This is experimentally realised by splitting the beam and shifting the frequency of the slowing part by -200 MHz in a double pass AOM, while the MOT repump light stays on resonance.
The third fibre laser[9] in our setup is based on stimulated emission in an Erbium-doped fibre. The fibre is pumped by diode lasers and the maximum output power after the doubling crystal is 1 W at $\lambda_{\mathcal{L}^s_{00}} = 531$ nm with a linewidth below 200 kHz. Crucially for our purpose, its frequency can be chirped with chirp rates up to 30 MHz/ms.

[7] Toptica DL 100 pro
[8] MPB VRFA-P
[9] Quantel EYLSA-A-531

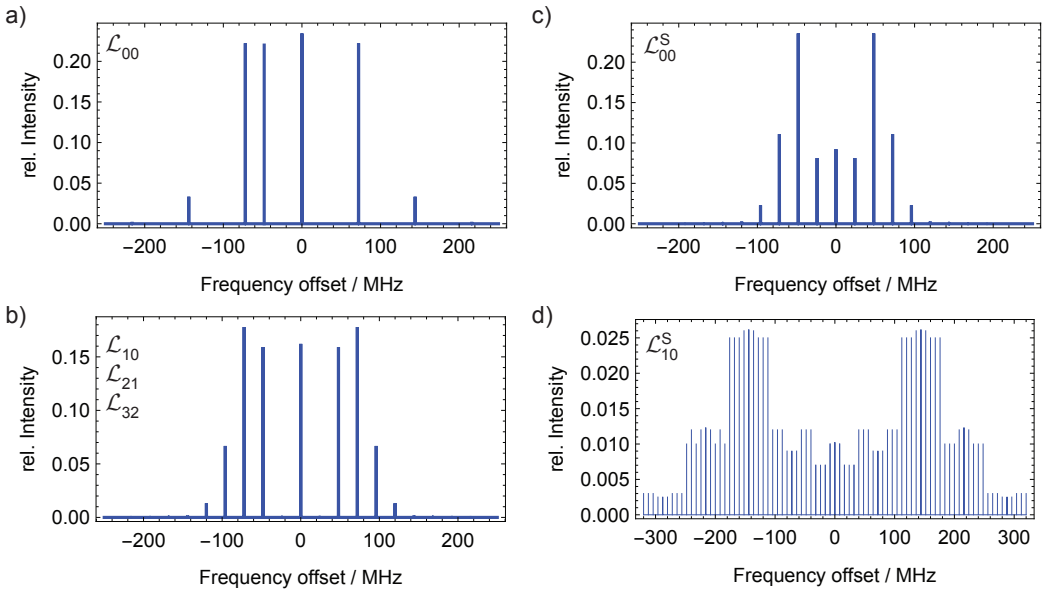

Figure 5.7: Summary of sideband structures used in this thesis. See text.

5.4 Sideband creation

All cooling, slowing and repump lasers need to address all four hyperfine levels (see section 2.3.6) to allow optical cycling. As the levels are separated by only tens of MHz, it is possible to reach them all by applying RF sidebands on a single laser frequency. For the cooling laser $\mathcal{L}_{00}$ this is done by first locking the laser on the $X^2\Sigma(J = 1/2, F = 0) \rightarrow A^2\Pi_{1/2}$ transition and splitting the beam in two parts, which will later be recombined. One part is sent through an acousto-optical modulator (AOM) in the minus first order of diffraction, which reduces the frequency by 48 MHz. The second part of the beam goes through an electro-optical modulator (EOM) running at 74 MHz. The optical layout to achieve this can be seen by following the orange path out of the 606 nm laser shown in figure 5.1. By tuning the amplitude of the EOM, which modulates its optical depth, we can add two sidebands to the fundamental frequency, so that the power is distributed about equally between all three components. The power in both beam paths is distributed in a way that the spectrum of the combined beam has 4 sidebands of equal intensity (figure 5.7 a.)).

There is a simpler way to produce all four required frequencies by using only a

single EOM at 24 MHz driven to higher modulation depth. This method produces additional sidebands which are not needed but are not harmful either when applied to the repump lasers which contribute very little to the forces in the MOT. The optical setup to generate the sidebands can be seen by following the laser path from any of the MOT repump lasers in figure 5.1. The resulting frequencies are shown in figure 5.4 b).

The laser slowing presented in chapter 6.4 requires sidebands on the slowing lasers as well. While the main slowing laser $\mathcal{L}^s_{00}$ uses a single 24 MHz EOM similar to the MOT repump lasers (but at slightly lower modulation depth), the spectrum of the repump laser $\mathcal{L}^s_{10}$ is simply broadened over about 500 MHz by passing it through EOMs at 72 MHz, 24 MHz and 8 MHz. This method is easier than chirping the repump laser and works equally well.

5.5 Beam combining

The laser beams used for slowing as well as for trapping in the MOT require combining light of multiple frequencies and polarisations, ideally into a single polarisation-maintaining optical fibre for perfect spatial overlap.

In the case of the laser beam used for radiation pressure slowing the required wavelengths are $\lambda_{\mathcal{L}^s_{00}} = 531$ nm and $\lambda_{\mathcal{L}^s_{10}} = 628$ nm with their respective sidebands. The polarisation of these beams is not crucial, except that there has to be a non-zero angle to the direction of the B-field in the slowing chamber to allow remixing of dark states. In practice the polarisation is chosen such that beams of both wavelengths are linearly polarised at 45 degrees to the magnetic field direction, but perpendicular to each other, since they are combined on a simple polarising beam splitter (PBS). We have tested both an integrated fibre-based beam combiner and a free-space setup where beams are coupled out of fibres, combined on a PBS, and coupled back into a fibre.

For the MOT beams, we have to combine four wavelengths, each with their sidebands. They consist of cooling light of wavelength $\lambda_{\mathcal{L}_{00}} = 606$ nm, which has components of two polarisations perpendicular to each other (the reason will be explained in chapter 8.1), and 3 repump laser frequencies. The polarisation of the repump

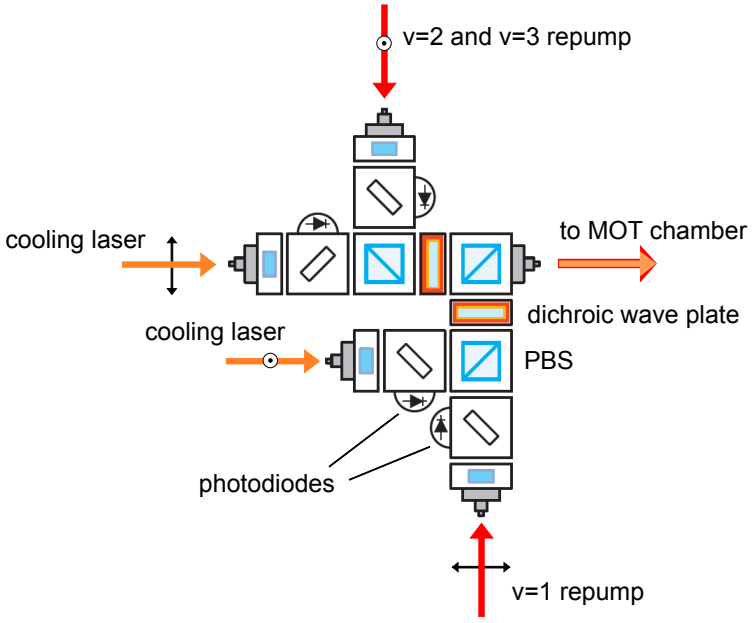

Figure 5.8: Beam combiner for the MOT light. The direction of linear polarisation is indicated by black arrows.

lasers is not crucial, since most of the forces in the MOT come from the cooling laser. We use an integrated fibre-based beam combiner[10] shown in figure 5.8. It uses polarising beam cubes and dichroic wave plates, which rotate the polarisation depending on the input wavelength. The coupling into the input fibres is monitored via photodiodes. The system has proven to be very stable, and delivers a total efficiency of about 50 percent in all beams, measured as ratio of power available in the MOT chamber to power coupled into the input fibres.

The light of the $v = 2$ and $v = 3$ repump lasers ($\mathcal{L}_{21}$ and $\mathcal{L}_{32}$) is combined on a simple 50:50 beam splitter before the MOT beam combiner. Since their wavelengths are very similar, the dichroic wave plate in the combiner works for both. The power requirements at these repump frequencies are not very high, as molecules are rarely pumped into high lying vibrational states, so the additional power loss from combining them beforehand is manageable.

[10] custom made by Schaefter-Kirchhoff

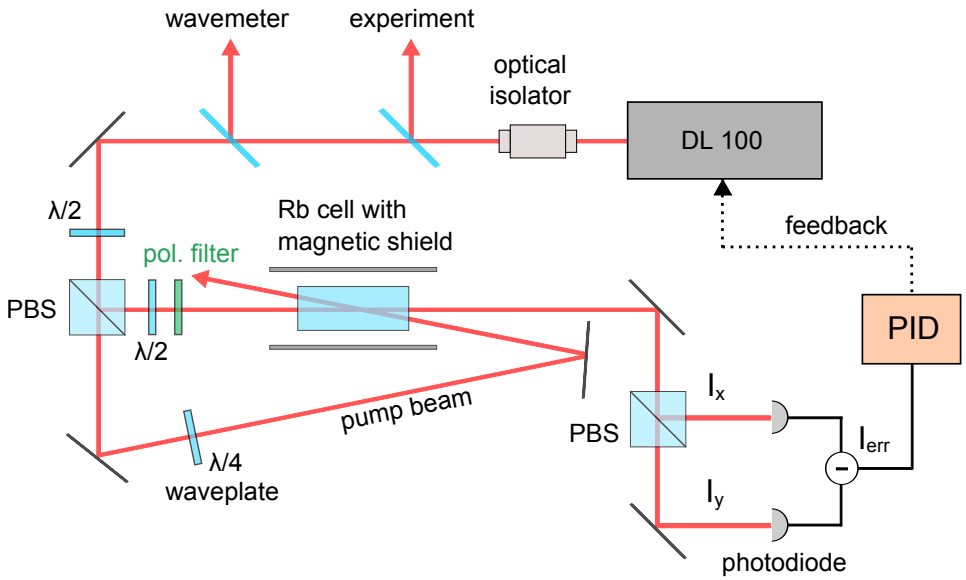

Figure 5.9: Setup of the polarisation spectroscopy.

5.6 Frequency stabilisation

A frequency locking system, stable from day-to-day at the 1 MHz level, is crucial to the research presented in this thesis. Double-checking frequency set points via spectroscopy measurements would cost valuable time every day, but is not needed in our case. All lasers are locked via transfer cavities to a reference laser, which is itself locked to a Doppler-free spectroscopic feature in Rb. This allows us to make a MOT within an hour of entering the lab in the morning.

5.6.1 Reference laser stabilisation

The reference laser is a Toptica DL 100 diode laser at 780 nm. It is locked to an atomic rubidium transition via polarisation spectroscopy [113]. This technique is an extension of the more common saturated absorption spectroscopy. There are a range of other techniques for frequency locking, for example modulation transfer spectroscopy [114, 115].

The setup of our polarisation spectroscopy is shown in figure 5.9. A laser beam is split into a strong pump and a weak probe beam, which then pass a vapour cell in opposite directions. Just as in saturation spectroscopy, the counter-propagating

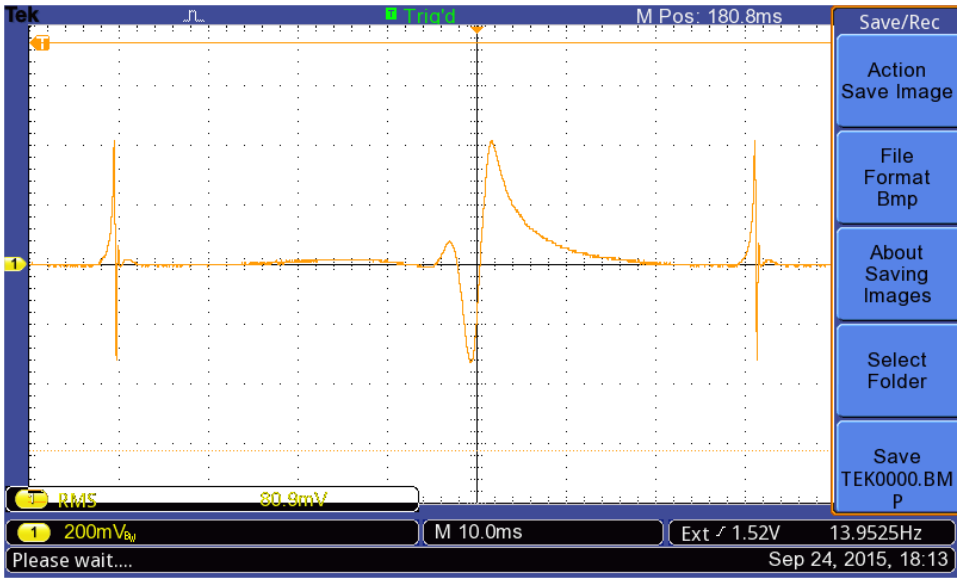

Figure 5.10: Typical dispersion signal of our polarisation spectroscopy. One box of the horizontal scale corresponds to a frequency change of 45 MHz.

pump beam allows a resolution below the Doppler broadening by depleting the ground state population (which leads to decreased absorption) of the velocity classes that are in resonance with both pump and probe at the same time. There are two cases when this can happen: Firstly, when the laser is directly on resonance with a hyperfine transition, the molecules with zero velocity relative to the probe beam will not be Doppler-shifted and will be resonant to both beams. The second case is less obvious: the so called cross-over peaks involve the depletion of a non-zero velocity class of atoms on one transition $F \rightarrow F'$ by the pump laser while the same atoms are resonant to the probe on a transition $F \rightarrow F''$ to a different excited state. There can also be cross-over resonances when atoms at one velocity and in one hyperfine state are optically pumped by the pump laser into another hyperfine state which is resonant with the probe.

Unlike in saturated absorption spectroscopy, in polarisation spectroscopy the pump beam is circularly polarised, while the probe beam has a linear polarisation at angle $\Phi = \pi/4$ to the plane of a polarising beam cube that is placed after the gas cell. The probe light passes this beam cube and is split into two parts, I_y and I_x, which are detected on photodiodes and electronically subtracted from each other. Without the

pump beam, the linear probe beam would be split in equal parts, $I_x = I_0 \sin^2 \pi/4 = I_0/2$ and $I_y = I_0 \cos^2 \pi/4 = I_0/2$, so the intensity of the error signal $I_{\text{err}} = I_y - I_x$ would be zero. The pump beam introduces a birefringence in the atomic vapour by pumping the population into higher (or lower) m_F states for σ^+ (or σ^-) pump light. Each linear polarisation can be written as a superposition of σ^+ and σ^- circularly polarised components. The two components experience a difference Δn in the index of refraction, which leads to a phase delay and effectively a rotation of the linear probe beam polarisation. A detailed analysis [113], neglecting the effect of the glass cell walls, gives the error signal intensity

$$I_{\text{err}} = I_0 e^{-\alpha L} L \Delta\alpha_0 \frac{x}{1+x^2} \tag{5.1}$$

with the cell length L, the average absorption coefficient $\alpha = \frac{\alpha_+ + \alpha_-}{2}$, the maximum difference in absorption of the two components $\Delta\alpha_0$ and the detuning in units of the linewidth $x = \frac{\omega - \omega_0}{\Gamma/2}$. This signal has a steep zero crossing at the atomic resonances and is well suited for frequency stabilisation via a feedback loop.

Our setup uses a Rubidium cell in which two isotopes ^{87}Rb and ^{85}Rb occur at a ratio of 28% to 72%. We lock our reference laser to the $F = 2 \rightarrow F' = 3$ transition in ^{87}Rb at 384.2278 THz. Figure 5.10 shows a typical dispersion signal. The frequency stability of the reference laser was investigated, finding a deviation of 0.7 MHz over half an hour, with a long term stability better than 1.5 MHz over 24 hours.

5.6.2 Transfer cavity offset lock

We use scanning Fabry-Perot cavities[11] to lock all lasers at a controlled frequency offset to the reference laser. The setup is shown in figure 5.11. By using dichroic mirrors and polarising beam splitters, up to 4 laser beams are sent through the cavity simultaneously and separated afterwards onto separate photodiodes. The cavity length L is scanned by applying a voltage ramp to a piezo actuator, which results in transmission peaks when the resonance condition $f = m \times \frac{c}{4nL} = m \times FSR$ is fulfilled (m being an integer). The photodiode signals and the voltage ramp are sent to the computer where the peak positions, expressed as a voltage, are found using real-

[11] Thorlabs, 1.5 GHz free spectral range (FSR)

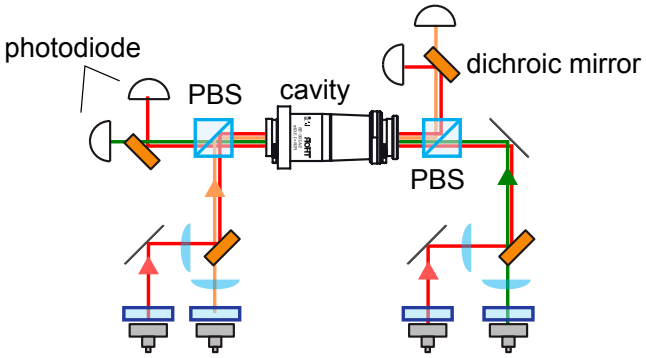

Figure 5.11: Offset locking setup with 4 frequencies in a single Fabry-Perot cavity.

time fitting of a lorentzian function. The error between the desired position and the actual position is used to create a feedback to each laser, for example by controlling the piezo voltage of its external cavity. The calibration of cavity piezo voltage to frequency offset can be done by looking at a laser spectrum with sidebands of known separation frequency. For the $\mathcal{L}^s_{00}$ laser we measure 385 MHz/V. The offset locking method relies on a linear relationship between piezo voltage and cavity length, which is usually true but can vary at very high voltages, which should be avoided.

Chapter 6

Deceleration of the CaF beam

The molecular source presented in chapter 3 produces molecules at velocities around 150 m/s, which is too fast for direct loading of a MOT. This chapter will discuss different approaches for slowing the beam, including a new method called Zeeman-Sisyphus deceleration, which is currently investigated in our group.

6.1 Predicted capture velocity of a MOT of CaF

How slow do the molecules need to travel to be captured in the MOT? This question is best answered with a complete three-dimensional simulation including the Zeeman shifts of all energy levels in the magnetic field, but a simple approximation in one dimension can give a first rough estimation.

Let's assume the MOT region as a sphere of diameter $d = 2r$, in which the molecule scatters photons at a constant rate R_{sc}. From basic mechanics we know that a molecule travelling with velocity v_{c} will be stopped by an acceleration a in the distance d, if

$$v_{\mathrm{c}} = \sqrt{2\,a\,d} \tag{6.1}$$

The acceleration $a = R_{\mathrm{sc}}\,\Delta v_{\mathrm{ph}}$ depends on the scattering rate R_{sc} and is proportional to the known velocity reduction per absorbed photon of the cooling laser, $\Delta v_{\mathrm{ph}} = 1.11$ cm/s. Assuming a value of $R_{\mathrm{sc}} = 1.5 \times 10^6$ s^{-1} (as measured in section 8.3.3)

of a counter-propagating beam[1], we find a value of $a = 1.7 \times 10^4$ m/s^2.
In the simplest approximation, the distance d can be assumed equal to the $1/e^2$ beam diameter $d_{1/e^2} = 16.2$ mm of the MOT beams. This leads to a capture velocity of $v_c = 23.4$ m/s. This approximation assumes that the molecule is in resonance to a counter-propagating laser beam over the whole distance d, an assumption which can depend on the power broadening, the magnetic field gradient and the detuning of the cooling laser. We are also neglecting the fact that molecules can enter the MOT area off-axis. Most likely the effective capture velocity is lower than our estimation.

6.2 Overview of common slowing methods

6.2.1 Zeeman and Stark decelerators

One common method to slow down a molecular beam relies on the Stark effect, which shifts the energy levels of a molecule in an electric field depending on its internal state. A Stark decelerator consists of a series of electrode pairs along the molecular beam that can be switched quickly [116]. Molecules in low field seeking states will see regions of high electric fields as potential hills and lose kinetic energy approaching the field maximum of an electrode pair. Once they reach it, the field is swapped non-adiabatically with the next pair of electrodes, transferring the molecules to the bottom of the potential hill, from where they start climbing again. In reference to Greek mythology, methods that involve this kind of repeated climbing of hills are called Sisyphus methods. Since the molecules are typically in weak field seeking states, they can be guided towards the beam axis where the field is smallest. Stark deceleration of molecules in strong field seeking states has been demonstrated [117], but is less common.
Similar to the Stark decelerator, a Zeeman decelerator can be designed using pulsed magnetic fields and the resulting Zeeman shift [118]. Both Zeeman and Stark decelerators require synchronisation between the motion of the molecules and the switching of the fields. For this reason, they work best with molecular pulses of limited length and velocity width.

[1] This is a simplification. In the experiment, there are instead two MOT beams propagating at an angle of 45 degrees to the molecular beam which mainly contribute to the trap loading.

6.2.2 Travelling wave deceleration

A travelling wave decelerator works by confining molecules with a certain velocity in a three-dimensional electric or magnetic trapping potential that initially moves at the same velocity and which is then slowed down gradually, decelerating the molecules in the process [119]. The deceleration is limited by the risk of removing the molecules from the trap. An electrical travelling wave decelerator has been successfully combined with a Stark decelerator to slow ammonia molecules from supersonic velocities to rest [120]. Just like Zeeman and Stark decelerators, the method provides no actual cooling due to the lack of dissipation of entropy.

6.2.3 Laser radiation pressure slowing

Another way to slow molecules is to use the radiation pressure of a counter-propagating laser beam. As the molecules slow down, their resonance frequency changes due to the decreased Doppler shift $\Delta\omega_D = kv$. In the *white light slowing* method [61], the molecules are kept in resonance by broadening the spectrum of the slowing laser to cover all relevant velocities, usually by electro-optical modulation. The method usually doesn't cool the beam[2] (e.g. reduce the width of the velocity distribution), but instead produces molecules at a wide range of velocities and positions in time. In contrast to this, the *frequency chirping* method controls the velocity of the beam by ramping the laser frequency gradually, which also longitudinally cools the molecules. This method is what allowed us to slow down CaF molecules to the capture velocity of the MOT [82] and is discussed shortly in section 6.4. Both methods have the downside that there is no transverse guiding, which leads to divergence of the slowed beam.

6.2.4 Centrifuge

The methods described so far all depend on the internal energy levels of the molecules. A much more general slowing technique has been demonstrated by using mechanical forces in a centrifuge [121]. In this method, polar molecules enter an electrical guide on the periphery of a rotating disc and are guided in a spiral towards its center, from

[2] it is possible to longitudinal cool the beam in white light slowing if the frequency spectrum has a sharp edge, and we have actually observed this in our experiment

Method	guiding?	longitudinal cooling?	continuous beams?
Zeeman dec. [122]	✓	×	×
Stark dec. [116]	✓	×	×
Travelling wave dec. [123]	✓	×	×
Centrifuge [121]	✓	×	✓
White light slowing [55]	×	(✓)	✓
Chirp slowing [82]	×	✓	×

Table 6.1: Summary of slowing methods for molecular beams.

where they exit in direction of the surface normal. The molecules are decelerated by having to climb the potential hill produced by the centrifugal force. The centrifuge can decelerate continuous beams of a wide range of velocities. There is no cooling of the beam, hence the beam diverges after leaving the guide.

6.2.5 Less common methods

Molecules have been slowed down by other methods, which can't all be discussed here, including counter-rotating nozzles [124], photo-dissociation [125], bichromatic forces [126] and collisions with atomic beams [127].
No single slowing method combines cooling, guiding and efficient slowing in a satisfactory way (see table 6.1). In the next section we present a new approach, the Zeeman-Sisyphus decelerator, that tries to combine all those properties.

6.3 The Zeeman-Sisyphus decelerator

An ideal deceleration method should allow simultaneous slowing, cooling and transverse guiding of continuous molecular beams down to velocities near the capture velocity of a MOT of about 20 m/s, while having a large phase space acceptance. Here we propose a new kind of decelerator for molecules, based on a Sisyphus type scheme in a static magnetic field, that uses optical pumping to dissipate the kinetic energy. We call it Zeeman-Sisyphus Decelerator (ZSD).
The general idea has first been introduced as a way to decelerate Rydberg atoms in inhomogeneous electric fields [128] and the same approach was later proposed

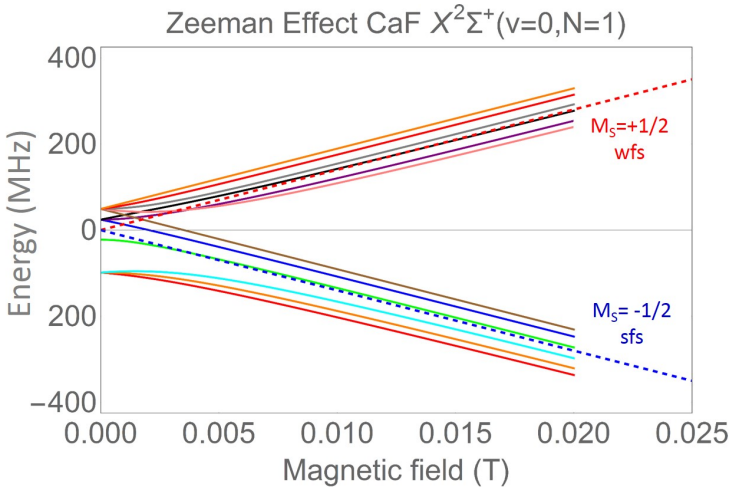

Figure 6.1: Zeeman shift of the N=1 rotational level of the X(v=0) state of CaF. At small magnetic fields the different states shift by $\Delta E = M_F g \mu_B B$, while at large magnetic fields they form an effective two-level system depending on their spin.

for neutral molecules [129]. More recently, Sisyphus type deceleration in magnetic fields has been discussed [130] and even been applied to load a magnetic trap [131]. Here we present some details of how to actually design such a decelerator, discuss its properties and show results of testing a first prototype that we built. The theoretical side of this work and the design of the prototype was done by a postdoctoral researcher in our group, Noah Fitch. His results, including numerical simulations of particle trajectories, are summarised in a recent paper [132]. Here I will focus on the general ideas and the experimental results of testing the method on our beam of CaF.

6.3.1 Zeeman effect in CaF

Molecules in a magnetic field experience a Zeeman shift of their internal energy levels proportional to the magnetic field strength B. We can distinguish *weak field seeking states* (wfs) which will see regions of high B-field as potential hills and will be attracted to low B-field areas, and *strong field seeking states* (sfs), which will be attracted to regions of high B-field.

The Zeeman shift in the first rotationally excited state (N=1) of X(v=0) of CaF is shown in figure 6.1. The Hamiltonian of the Zeeman interaction is consists of

nuclear, orbital and spin terms

$$\hat{H} = \vec{\mu} \cdot \vec{B} = \underbrace{g_S \mu_B \vec{S} \cdot \vec{B}}_{spin} + \underbrace{g_L \mu_B \vec{L} \cdot \vec{B}}_{orbital} + \underbrace{g_I \mu_B \vec{I} \cdot \vec{B}}_{nuclear} . \tag{6.2}$$

Since the ground state of CaF is a Σ state, we have $\vec{L} = 0$. The nuclear term can be neglected due to a much smaller Landé factor g_I, so that only the spin term remains which produces the energy shift $\Delta E = g_S \mu_B \vec{S} \cdot \vec{B} = g_S M_S \mu_B B$. This can be seen at strong magnetic fields (> 100 G) in figure 6.1, where the 12 magnetic sublevels of the ground state effectively split into a two-level system of spin-up ($M_S = +1/2$) and spin-down ($M_S = -1/2$) states, which are separated by $\Delta E_{\text{Zee}} = g_S \mu_B \Delta M_S B = 28h \times B\,\text{GHz/T}$.

At low magnetic fields, the coupling of the spin to the magnetic field is smaller than the coupling of the spin to rotational angular momentum $\vec{N}$ and nuclear spin $\vec{I}$. Recall that, at zero magnetic field, the $N = 1$ level is split into four hyperfine components labelled $F = (1^-, 0, 1^+, 2)$ (see section 2.3). At low magnetic fields, the states are best described by the total angular momentum quantum numbers (F, M_F) and have a Zeeman shift $\Delta E_{\text{Zee,low}} = g_F M_F \mu_B B$, with the Landé factors of the 4 hyperfine states $g_F = (-1/3, 0, 5/6, 1/2)$ for the $F = (1^-, 0, 1^+, 2)$ state respectively. The Zeeman shift of the exited state $A^2\Pi_{1/2}$ is about 50 times smaller than that of the ground state, so in the simplest picture it can be neglected. This is because the contributions of the spin $\vec{S}$ and the angular momentum $\vec{L}$ to the magnetic moment cancel each other out and produce an effective Landé factor $g \approx 0$.

6.3.2 Deceleration principle

The slowing scheme is shown in figure 6.2 and the experimental setup in figure 6.3. Alternating regions of high and low magnetic field strengths are produced by permanent magnets along the molecular beam, while two pump beams are counter-propagating to the molecules. A molecule in a weak field seeking (wfs) state enters a region of high B-field and gains potential energy, which in turn leads to a reduction of its kinetic energy. On top of the potential hill it comes into resonance with light of the first pumping laser that optically pumps it into a strong field seeking (sfs)

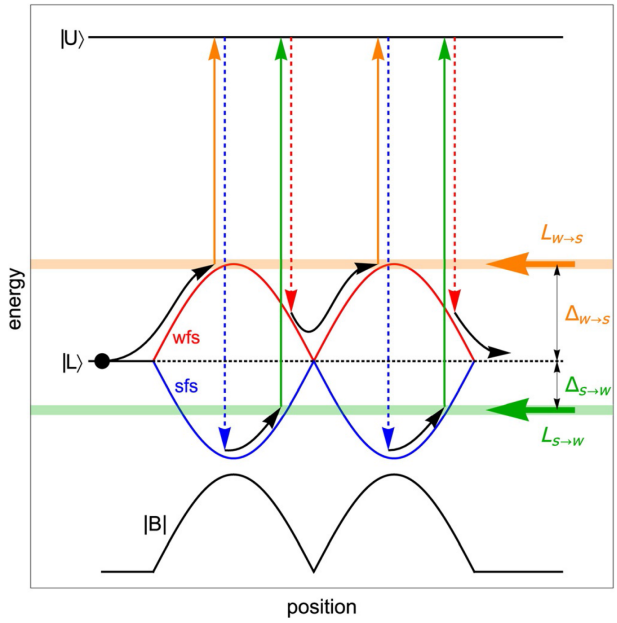

Figure 6.2: Sisyphus deceleration scheme. Molecules (black dot) decelerate by repeatedly climbing potential hills and are optically pumped near the hilltops by two counter-propagating pump lasers (green and orange). Dotted lines mark spontaneous decay. Adapted from [132].

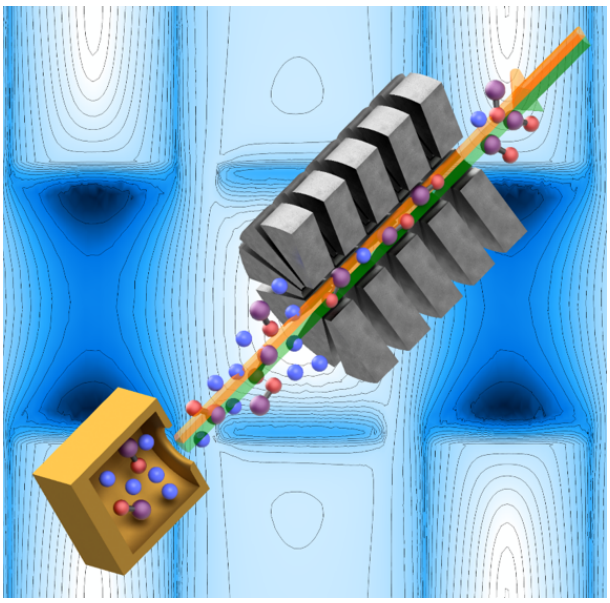

Figure 6.3: Sisyphus decelerator setup, showing molecules from a buffer gas source travelling through an array of permanent magnets while being addressed by 2 pump lasers. Adapted from [132] (Inside cover).

state. In this state the molecule experiences a negative energy shift from the high B-field. Since it is still moving in the z-direction towards a low B-field region, it has to climb up the next potential hill and is slowed again. Near the B-field minimum it is optically pumped back into a weak field seeking state by the second pump laser and the cycle starts again. The optical pumping laser is tuned to the laser cooling transition from $X(v = 0, N = 1)$ to $A(v = 0, J = 1/2)$. This transition remains rotationally closed for all relevant magnetic field strengths because the magnetic field does not mix states of opposite parity and the $N = 3$ state is energetically distant from $N = 1$. The strong spin-orbit interaction in the A state ensures that the electron spin can flip in the decay back to the X state, switching the molecule between wfs and sfs states.

Depending on the magnetic field strengths the slowing method can be very efficient. The kinetic energy extracted per cycle depends on the detuning of the pump lasers and is given by

$$\Delta E_{\text{kin}} = 2\left(|\Delta_{W-S}| - |\Delta_{S-W}|\right) \tag{6.3}$$

The detuning Δ_{S-W} should be chosen small but non-zero to avoid unintended optical pumping. There is a benefit to choosing a slightly larger Δ_{S-W} of a few GHz, as this means the molecules will spend more time in the wfs state than in the sfs state. Since the magnetic field is the weakest on the beam axis, molecules in wfs states are focused towards the axis while in a sfs state they are drawn towards the magnets. The imbalance in time spent in the different states should lead to net focusing of the beam and increase transverse stability.

The method is very efficient in the number of scattering events needed, compared to the 10^4 scattered photons in chirp or white light slowing. For example, with a detuning $\Delta_{W-S} = 14$ GHz (corresponding to a 1 T magnetic field) and $\Delta_{W-S} = 3$ GHz, we extract $\Delta E = h \times 22$ GHz per strong field stage, slowing a CaF molecule from 150 m/s to 10 m/s in 76 stages. The ZSD is therefore a viable option for molecules with less closed cycling transitions, for example YbF.

Apart from combining efficient deceleration, guiding and possibly longitudinal cooling (see section 6.3.3), the strength of the ZSD is that it is completely time-independent.

Nothing is switched, and the laser frequencies are static, so it works for continuous particle beams. It also works for molecules with a large range of initial velocities, since they all come into resonance at some point on the potential hill.

6.3.3 Longitudinal cooling

Simulations done by Noah Fitch suggest that there is a way to modify the ZSD to reduce the width of the longitudinal velocity distribution of the molecular beam [132]. In the configuration as shown in figure 6.2, this isn't the case: The counter-propagating pump lasers actually increase the velocity width by bringing the faster molecules (with larger Doppler shift) into resonance when they have travelled less far up the potential hill, so they get slowed less. Also, faster molecules spend less time in the pumping region, making it more likely for them to not get optically pumped and skip a deceleration step. Even when neglecting these two effects, the ZSD removes the same amount of kinetic energy (not velocity) from each molecule, which widens the velocity distribution.

Our solution to this problem is to taper the magnitude of the maximum B-field so that it increases slightly from the first to the last deceleration stage. If now the detuning $\Delta_{W\to S}$ is chosen as resonant with an energy slightly above the first potential hilltop, only the fastest molecules will be in resonance with the pump laser due to their large Doppler shift and will decelerate. The slower molecules will not be able to dissipate their potential energy, hence regain their initial velocity while descending the potential hill. Due to the tapered potential energy landscape, at each following stage a slightly slower class of molecules will start to decelerate, until all molecules have joined. Effectively each velocity class experiences a decelerator of different length and gets decelerated accordingly, leading to a reduced longitudinal velocity width. Unfortunately this technique increases the required total length of the decelerator, so it might not be practical in all cases.

6.3.4 Magnet design

If a Zeeman decelerator for CaF needs around 70 strong field stages, the periodicity L needs to be less than 2 cm for the decelerator to fit in our vacuum chamber.

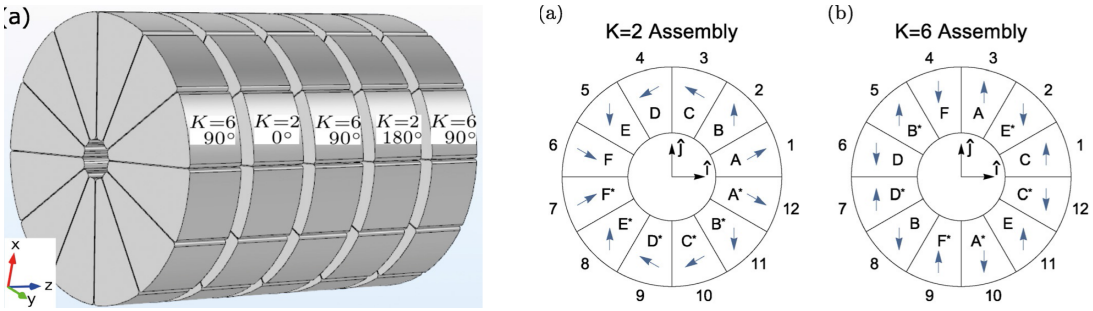

Figure 6.4: Magnet design for the ZSD. Left: Setup with alternating guiding (K=6) and deceleration stages (K=2). Right: Magnetizations (blue arrows) of the guiding and deceleration stages in Halbach configuration. Both figures adapted from [132].

Our design uses NdFeB permanent magnets in a so called Halbach configuration. A Halbach magnet has a magnetization that rotates K times when going once around the cylinder in the radial plane (see figure 6.4). For $K = 2$ this leads to a *deceleration stage*, with a strong magnetic field in the centre pointing in a defined radial direction. For $K = 6$ we get a magnetic field that is almost zero in the middle, and increases with distance from the centre, a *guiding stage*. Using these guiding stages is preferred over just leaving a gap between the strong field stages because of their transverse magnetic field profile, which strongly confines wfs molecules by its steep radial field gradient.

We have set up two versions of cylindrical magnetic stages. The smaller one has an inner diameter 5 mm, outer diameter 30 mm and longitudinal thickness of 5 mm. The maximum on-axis magnetic field for this design was $B_{\mathrm{max,small}} = 0.64$ T, as measured with a Hall probe. The larger version has the same inner diameter, a larger outer diameter of 40 mm and a thickness of 8 mm. The maximum on-axis magnetic field of this larger version is measured to be $B_{\mathrm{max,large}} = 1.3$ T.

Deceleration stages and guiding stages are mounted in alternating order, with the magnetisation of neighbouring deceleration stages oriented 180° to each other to cancel fringe fields (see figure 6.4).

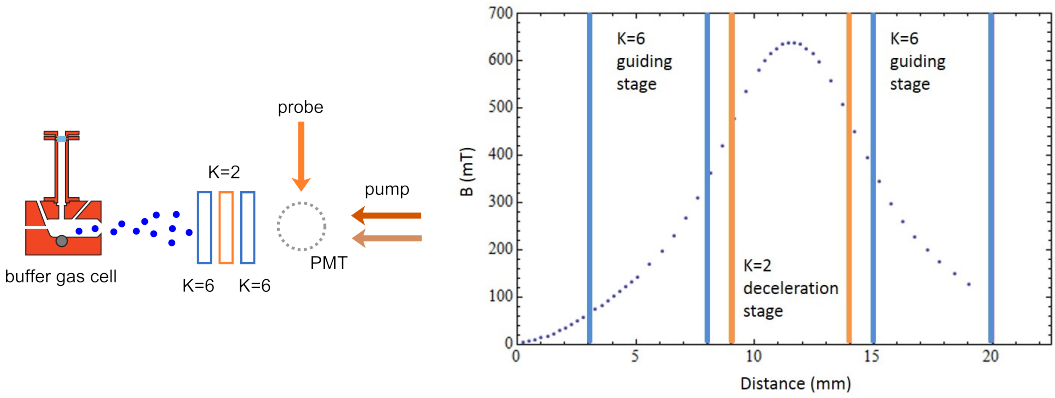

Figure 6.5: Left: Test setup for the ZSD, consisting of a single deceleration stage between two guiding stages. Right: Results of measuring the B-field on the beam axis with a Hall probe. The regions between blue lines are the guiding stages. The region between orange lines is the deceleration stage.

6.3.5 First results

Before setting up the whole decelerator with about 70 stages, we investigated the optical pumping between wfs and sfs states on a single deceleration stage. A high pumping efficiency is crucial, especially on the transition from sfs to wfs states, since a molecule remaining in a sfs state will be attracted by the magnets and is more likely to be lost.

Test setup

The test setup is shown in figure 6.5. Here, we use the smaller of the two prototypes described above. A single deceleration stage is placed between two guiding stages, all separated by 1 mm thick spacers. The setup is installed into the chamber on the beam axis so that the molecules reach a detection region 5 cm after exiting the last stage. The pump laser has just a single frequency addressing the $X(v = 0, N = 1) \rightarrow A(v = 0, J = 1/2)$ transition, which can be red or blue detuned to investigate the pumping from wfs to sfs states or vice versa. The detection by light induced fluorescence is done with a single frequency of laser $\mathcal{L}_{00}$ without sidebands. By scanning the laser over the four hyperfine states in subsequent experimental shots, the population distribution in those states is measured, both with and without

the pump beam applied. The angle of linear polarisation of the pump beam is optimised for pump efficiency. The optimum angle is perpendicular to the angle of magnetisation of the deceleration stage and the efficiency varies by less than 5 percent over a range of $\pm 45°$ around this value.

Pumping from strong field seeking to weak field seeking states

The initial spectrum of the four hyperfine states of the $N = 1$ state is shown in figure 6.6. We determine the relative populations by fitting a sum of four Lorentzian functions of equal width but different height to the data. The resulting heights of the $F = (1^-, 0, 1^+, 2)$ states are labelled as A, B, C and D.

How do we expect the populations to change after the optical pumping step? Answering this question requires knowing both the transition matrix T from the 12 magnetic sublevels (labelled by quantum numbers (F, M_F), see figure 6.1) to the 4 $(F, M_F)^*$ excited state sublevels and the branching matrix B for the decay back to the 12 ground states. These matrices are given in appendix C. After a number of scatters the population will approach a steady state, which is described by the matrix $\hat{M}_s$. The algorithm to derive this matrix is explained in detail in appendix C. For pumping with blue detuned light (pumping from sfs to wfs states) on an initial population $P_i = (A, B, C, D)^T$, the steady state population is given by

$$P_{\text{steady},s} = \hat{M}_s P_i = \begin{pmatrix} 0 & 0 & 0 & 0 \\ 0 & 0 & 0 & 0 \\ 0 & 1/2 & 5/6 & 1/10 \\ 1 & 1/2 & 1/6 & 9/10 \end{pmatrix} \cdot \begin{pmatrix} A \\ B \\ C \\ D \end{pmatrix} = \begin{pmatrix} 0 \\ 0 \\ B/2 + 5C/6 + D/10 \\ A + B/2 + C/6 + 9D/10 \end{pmatrix} \quad (6.4)$$

We see that the populations of the $F = 1^-$ and $F = 0$ states vanish completely, while the population of the other two states increases. This prediction is shown in figure 6.6, together with the experimental results of optical pumping with a detuning of $\Delta_{S\to W} = 2.6$ GHz. Experiment and theory agree very well, taking into account that the prediction assumes a state switching efficiency of 100 percent.

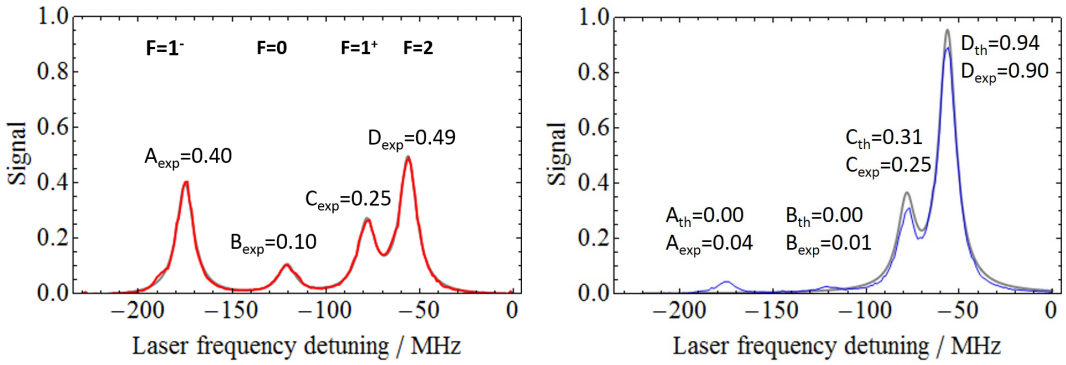

Figure 6.6: Left: Measured hyperfine spectrum (red) with fit (grey). Right: Measured spectrum after optical pumping from sfs to wfs states (blue) and predicted spectrum for optical pumping with unity efficiency (grey). Heights from fit and prediction are given, labelled with subscripts *exp* and *th* respectively.

Pumping from weak field seeking to strong field seeking states

Detuning the pumping laser to the red of the A-X(0-0) transition addresses weak field seeking states. Like before, we determine the change in the population of the hyperfine spectrum by tracking each sublevel and its transition and decay probabilities. The result for the steady state population is

$$P_{\text{steady},w} = \hat{M}_w P_i = \begin{pmatrix} 1 & 0 & 0 & 3/5 \\ 0 & 1 & 1/3 & 1/10 \\ 0 & 0 & 7/12 & 1/10 \\ 0 & 0 & 1/12 & 1/5 \end{pmatrix} \cdot \begin{pmatrix} A \\ B \\ C \\ D \end{pmatrix} = \begin{pmatrix} A + 3D/5 \\ B + C/3 + D/10 \\ 7C/12 + D/10 \\ C/12 + D/5 \end{pmatrix} \quad (6.5)$$

This time the $(F = 1^-)$ and $(F = 0)$ populations are increased while the other two are decreased but not completely pumped out. Prediction and experimental results are shown in figure 6.7, agreeing well with each other.

Pumping efficiency: experiment vs scattering rate model

Now that the pumping process seems generally understood, we can determine the pumping efficiency χ by measuring the fraction of the population in the $(F = 1^-)$ state that is pumped out by the blue detuned pump laser (pumping from sfs to wfs states). We define the pumping efficiency as $\chi = 1 - P_f/P_i$, where P_i and P_f

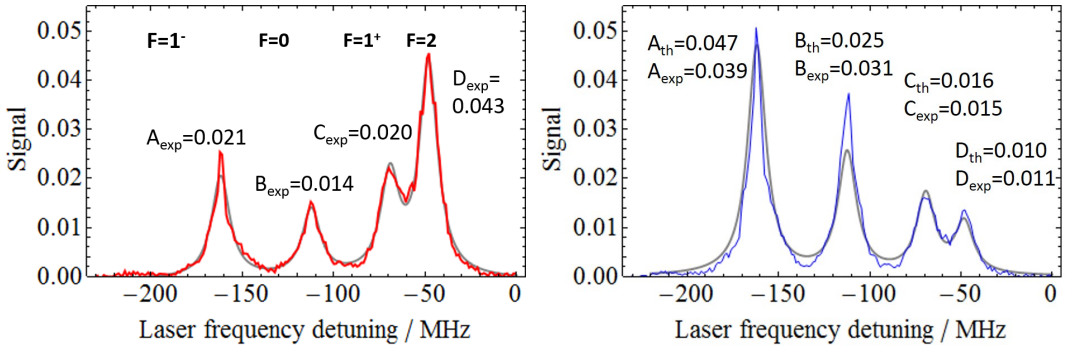

Figure 6.7: Left: Measured hyperfine spectrum (red) with fit (grey). Right: Measured spectrum after optical pumping from wfs to sfs states (blue) and predicted spectrum for optical pumping with unity efficiency (grey). Heights from fit and prediction are given, labelled with subscripts *exp* and *th* respectively.

are the initial and final populations of the $(F = 1^-)$ state. Figure 6.8 shows the measured pumping efficiency vs intensity in the pump light for both the small and the large magnets. We reach saturation at about 0.4 W/cm^2 and 0.9 W/cm^2 with the small and large magnets respectively. The maximum pumping efficiency is about 90 percent. This should be sufficient to allow a stable operation of the ZSD. The higher intensity needed for the stronger magnet is explained by the higher magnetic field gradient, which reduces the distance over which the molecules are in resonance and with it the interaction time.

We can model the optical pumping as a binomial process, in which after excitation by a pump photon the molecule has a probability of p to switch its state (from a wfs to a sfs state or vice versa), while with probability $(1-p)$ it will decay back into its initial state. The probability of a successful transition after n scattered photons is given by

$$\chi = 1 - (1-p)^n \,. \tag{6.6}$$

The value of p depends on the specific sublevels (F, M_F) of the molecule and the magnetic field B but can be approximated by $p = 1/2$. This means we require at least $n = 4$ scattered photons for a probability $\chi > 0.93$.

The average number of scattered photons over a time t is

$$\bar{n} = \int_0^t R_{sc}\,\mathrm{dt'} \tag{6.7}$$

with the scattering rate

$$R_{sc} = \frac{\Gamma_{\mathrm{eff}}}{2}\frac{I/I_{\mathrm{sat,eff}}}{1 + I/I_{\mathrm{sat,eff}} + 4\Delta^2/\Gamma^2} \tag{6.8}$$

of a multilevel system. For our system with $n_g = 6$ ground state sublevels connected to $n_e = 4$ excited states we find (see section 2.4.2)

$$I_{\mathrm{sat,eff}} = \frac{2n_g^2}{n_e + n_g} \cdot I_{\mathrm{sat}} = 7.2\, I_{\mathrm{sat}} \tag{6.9}$$

$$\Gamma_{\mathrm{eff}} = \frac{2n_e}{n_e + n_g} \cdot \Gamma = 0.8\,\Gamma. \tag{6.10}$$

The detuning $\Delta = \Delta_{\mathrm{laser}} + \Delta_{\mathrm{Zee}} + k \cdot v$ contains the position dependent Zeeman shift $\Delta_{\mathrm{Zee}}(x') = 14\,\mathrm{GHz/T} \cdot B(x')$, which translates into a time dependence for molecules at a velocity v via $x' = v \cdot t$. We approximate the magnetic field as

$$B(x') = B_{\max} \cdot e^{\frac{-(x')^2}{2\sigma^2}}, \tag{6.11}$$

with the measured values of $\sigma_{\mathrm{small}} = 3.4$ mm, $\sigma_{\mathrm{large}} = 4.3$ mm, $B_{\mathrm{max,small}} = 0.64$ T and $B_{\mathrm{max,large}} = 1.3$ T. By integrating equation 6.7 and inserting the result into equation 6.6 we find the pumping efficiency. Fixing the detuning at the values used in the experiment and varying the pump intensity, our model reproduces the experimental results shown in figure 6.8, except that the effective scattering rate had to be set to $\Gamma_{\mathrm{eff}} = 0.4\Gamma$, a factor of 2 smaller than predicted. This could be partially due to the fact that the optical pumping process is stochastic by nature. A mean number $\bar{n}$ of scattered photons will always include some molecules with very few scatter events, which will decrease the pumping efficiency more strongly than a molecules with above average scattering rate would increase it, due to the diminishing returns of the binomial function.

Another possible explanation is due to the Zeeman shift of the excited state of 0.3 GHz/T [132], which was neglected so far. Our model assumes that a molecule that

was not successfully pumped from one manifold of states to another and returns to its initial manifold of states will be at resonance and can immediately be pumped again. However, since some ground states dominantly couple to the strong field seeking upper states and some to the weak field seeking upper states, a molecule can end up returning to a ground state that is not currently resonant, and might have passed the position of resonance already.

We now fix the intensity and vary the detuning ($I = 0.8$ W/cm^2, small magnets). Figure 6.8 shows the pumping efficiency measured as a function of the detuning, along with the results of the model described above as Δ_{laser} is varied. The experimental data shows a rapid drop in the pumping efficiency at a detuning of about 9 GHz which corresponds to the magnetic field at the top of the potential hill. This is to be expected since the molecules never come into resonance with the light if the light is tuned above the potential hilltop. Our model with the same parameters reproduces the general trend but has a much sharper cutoff near the detuning corresponding to B_{max}. This can be explained by the fact that so far we neglected the transverse magnetic field profile. Molecules that pass the B-field maxima closer to the magnets will experience a higher field and can still be pumped when molecules at lower fields on the beam axis have fallen out of resonance. The frequency width of the slope of about 1 GHz corresponds to a magnetic field difference of 0.1 T, which agrees well with simulations of the transverse magnetic field profile in [132].

Interference from the Q(1) transition

One challenge at high magnetic fields is that additional rotational transitions can come into resonance. In CaF we work on the P(1) transition, i.e. the transition starting in $N = 1$ and reducing the rotational quantum number by 1 to $N = 0$ in the upper state[3]. The $N = 1$ and $N = 0$ rotational levels of the A state are separated by 29 GHz. Since in a magnetic field the separation between wfs and sfs ground states increases with 28 GHz/T, at about 1.04 T the P(1) transition frequency from a sfs state and the Q(1) transition frequency ($N = 1 \rightarrow N = 1$) from a wfs state are

[3]this is a simplification, the A state does not actually have a well defined quantum number N (see section 2.1.3)

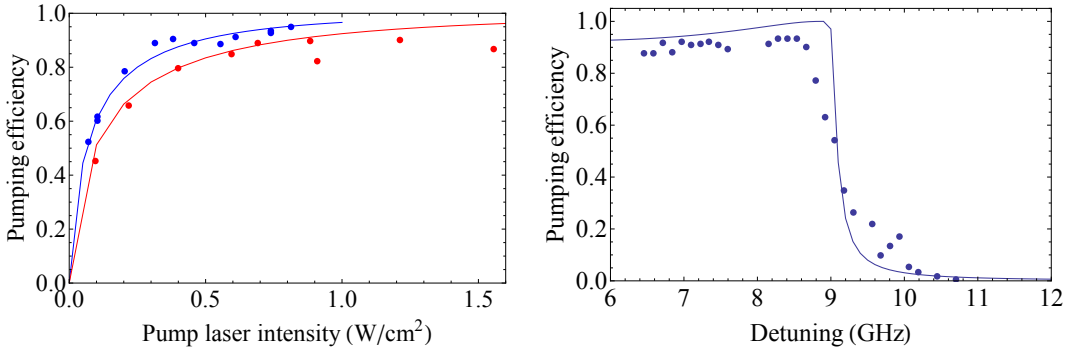

Figure 6.8: Left: Pumping efficiency vs laser intensity in the pump beam. Blue points are measurements taken with small magnets ($B_{\max} = 0.64$ T) at $\Delta_{S\to W} = 7$ GHz, red is with large magnets ($B_{\max} = 1.3$ T) at $\Delta_{S\to W} = 5$ GHz). Solid lines are theoretical predictions (see text). Right: Pumping efficiency vs detuning of the pump light, at $I = 0.8$ W/cm^2 with small magnets.

crossing (see figure 6.9). If the detuning of the pump laser is chosen at a value larger than this critical crossing frequency, it will address multiple transitions at different Zeeman shifts (and positions) in the magnet.

For example, say the detuning is chosen as +17 GHz (shown by the red dashed line in figure 6.9). A molecule entering the magnet will first come into resonance with the Q(1) transition at a magnetic field strength of $B = 0.9$ T and will be optically pumped out of the wfs states into the $N = 1$ level of the A state, which has positive parity. From there it can decay into the $N = 1$ or $N = 3$ levels of the X state, both of which have negative parity. Assuming equal branching ratios, 50% of the population will be lost into states dark to our lasers, while the remaining 50% will switch from wfs to sfs with a probability $p = 0.5$. If a molecule didn't switch the first time, a second excitation will result in a loss of 50% of the remaining population again. The total fraction of molecules lost into $N = 3$ can be calculated as a geometric series as $0.5 + 0.5^3 + 0.5^5 + ... = 0.5 \cdot \sum_{k=0}^{\infty} 0.5^{2k} = 2/3$. This means only $r_Q = 1/3$ of the population remains in $N = 1$ after optical pumping on the Q(1) transition.

After all molecules are pumped out of the wfs states, at $B = 1.2$ T the population remaining in $N = 1$ will be optically pumped as usual on the P(1) transition, without losses, and transferred back into wfs states. Finally, when leaving the deceleration magnet, the molecule will pass a position with $B = 0.9$ T again and will be

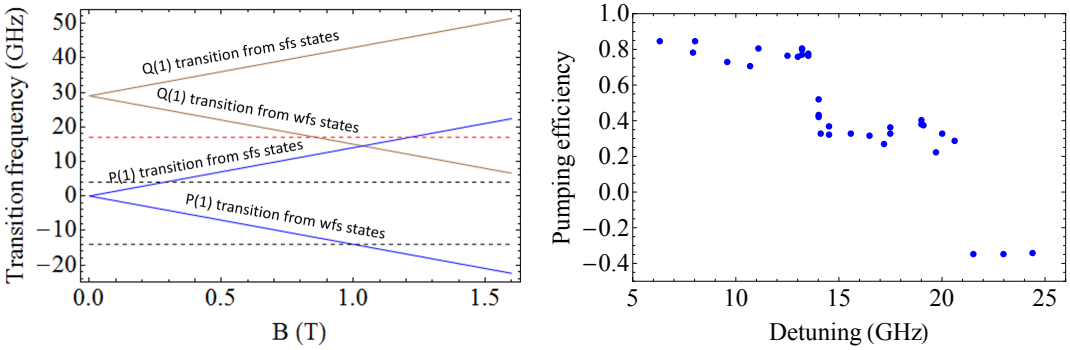

Figure 6.9: Left: Rotational transition frequencies in CaF (relative to the P(1) transition at $B = 0$) vs. magnetic field strength. Black dashed lines show the pumping frequencies needed for the ZSD, the red dashed line shows $\Delta = 17$ GHz detuning. Right: Measured pumping efficiency with large magnets. The drop in efficiency at 14 GHz detuning is caused by the Q(1) transition (see text).

transferred back into sfs states with losses into other rotational states. The whole pumping sequence leads to large losses of population which makes a normal operation of the ZSD impossible.

Figure 6.9 shows a measurement of the pumping efficiency vs detuning with large magnets ($B_{\max} = 1.3$ T). The data shows a first drop in the efficiency (measured as fraction pumped out of $(F = 1^-)$) at 14 GHz, corresponding to the point from where the Q(1) transition will be in resonance at lower B fields than the P(1) transition (where the blue and brown lines cross in figure 6.9). At about 20 GHz, corresponding to a magnetic field of $B_{\max} = 1.3$ T, we see another drop in the efficiency since here the P(1) transition falls completely out of resonance. This is the same effect as seen in figure 6.8, but now pushed to higher detuning because of the stronger field of the larger magnets. The Q(1) transition is still driven and transfers the population into sfs states, which explains the negative pumping efficiency of about -0.4, corresponding to an enhancement of the population in the $(F = 1^-)$ hyperfine state by 40 %. This enhancement value makes sense, since in the same pumping process on the P(1) transition we observe an enhancement of about 120% (see figure 6.9), and 2/3 of these transferred molecules are lost to other rotational states in the Q(1) transition (see appendix C).

We can add the losses to our model to predict the experimental results of optical

pumping above the critical frequency. In the simplest approximation, the optical pumping of wfs states on the Q(1) transition can be described by multiplying the optically pumped populations of theses wfs states with the factor $r_Q = 1/3$ (the fraction that remains in $N = 1$). The sfs states, which are not addressed by the lasers in this pumping step, don't exhibit losses. In the matrix in equation 6.5, they correspond to the diagonal elements. We hence multiply only the off-diagonal elements of the matrix $\hat{M}_w$ with r_Q, resulting in the matrix $\hat{M}_Q$, which describes the pumping from wfs to sfs states on the Q(1) transition:

$$P_{Q(1)} = \hat{M}_Q P_i = \begin{pmatrix} 1 & 0 & 0 & 3/5 \cdot r_Q \\ 0 & 1 & 1/3 \cdot r_Q & 1/10 \cdot r_Q \\ 0 & 0 & 7/12 & 1/10 \cdot r_Q \\ 0 & 0 & 1/12 \cdot r_Q & 1/5 \end{pmatrix} \cdot \begin{pmatrix} A \\ B \\ C \\ D \end{pmatrix} = \begin{pmatrix} A + 3D/5 \cdot r_Q \\ B + (C/3 + D/10) \cdot r_Q \\ 7C/12 + D/10 \cdot r_Q \\ C/12 \cdot r_Q + D/5 \end{pmatrix}$$

As before the pumping of sfs states on the P(1) transition is described by equation 6.4. Assuming a typical initial population $P_i = (1, 0.5, 1, 2)$ and $r_Q = 1/3$, a single pumping step on the Q(1) transition gives $\hat{M}_Q P_i = (1.4, 0.68, 0.32, 0.43)$. We find a population of $A = 1.4$, corresponding to the enhancement of the $(F = 1^-)$ hyperfine peak by 40% at detunings above 20 GHz. Similarly, at detunings between 15 and 20 GHz we expect a population of $\hat{M}_Q \hat{M}_s \hat{M}_Q P_i = (0.43, 0.14, 0.23, 0.45)$. A population of $A = 0.43$ corresponds to a pumping efficiency of $\chi = 0.57$, higher than the value of about 0.35 observed in the experiment (see figure 6.9). However, this prediction so far assumes 100% pumping efficiency. If we include the pumping efficiency $p = 0.8$ in each pumping step, we get $\hat{M}_Q \hat{M}_s \hat{M}_Q P_i = (0.59, 0.25, 0.34, 0.76)$, hence $A = 0.59$ and a pumping efficiency of 0.41, quite close to the experimental results.

In conclusion, pumping to other rotational states should be avoided when running our decelerator. Fortunately the detunings of $\Delta_{W\to S} = -14$ GHz and $\Delta_{S\to W} = +3$ GHz needed for the ZSD with CaF don't drive the Q(1) transition (see figure 6.9). This could be different for other molecules and should be kept in mind.

6.3.6 Next steps

We are currently setting up the full Zeeman-Sisyphus decelerator and will test it in the CaF or YbF beamline in our group. It is especially interesting for YbF, since here laser cooling is more difficult due to less favourable Franck-Condon factors. A slow beam of YbF could enhance the sensitivity in the search for the electron's electric dipole moment (see section 1.1.3).

6.4 Chirped radiation pressure slowing of CaF

The final result of this thesis, the realisation of a magneto-optical trap of CaF molecules, is built on the successful deceleration of the molecules below the capture velocity by chirped laser slowing. Since these experiments will be described in detail in the thesis of my PhD colleague Hannah Williams, only the main results as summarised in our publication [82] will be given here.

6.4.1 Setup and method

The setup is shown in figure 6.10. CaF molecules are produced in a buffer gas source (see chapter 3) at $t = 0$ and $x' = 0$ and travel through the slowing chamber towards the probe region at $x' = 130$ cm (PMT 3). On the way they are decelerated by a counter-propagating laser beam containing the wavelengths $\lambda_{\mathcal{L}^s_{00}} = 531$ nm (main slowing laser, P=100 mW) and $\lambda_{\mathcal{L}^s_{10}} = 628$ nm ($v = 1$ repump laser, $P = 100$ mW), with sidebands as shown in figure 6.10. With these two lasers about 3×10^4 photons can be scattered before half of the molecules have decayed into higher lying vibrational states. A magnetic field of about 0.5 mT is applied along the chamber to remix dark states (see chapter 2.4.4). The molecules are detected by laser-induced fluorescence detection 1.3 m from the source. The probe laser either crosses the molecular beam at 90 degrees, in which case the measurement is Doppler-insensitive, or it crosses at 60 degrees giving a Doppler-sensitive measurement. The probe laser is scanned over the hyperfine components of the $N = 1$ state. By comparing the spectrum obtained using the two probe lasers, we are able to determine the velocity distribution. More details of the method are given in [82].

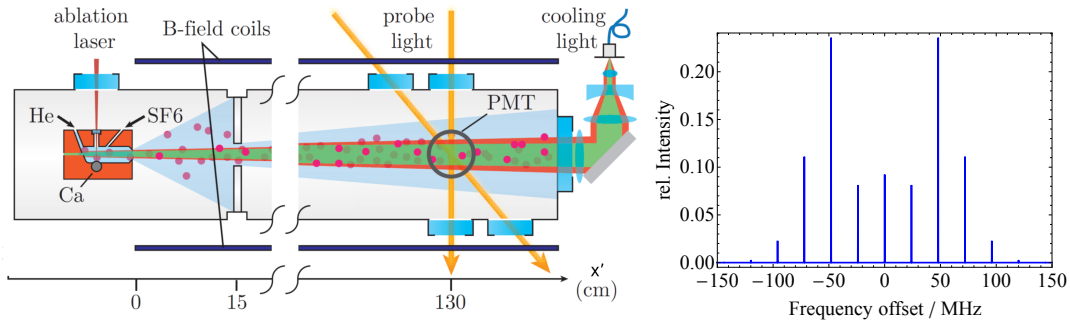

Figure 6.10: Left: Setup of the chirp slowing experiment (see text). Adapted from [82]. Right: Sideband structure used for both the main slowing laser $\mathcal{L}^s_{00}$ and the repump laser $\mathcal{L}^s_{10}$.

6.4.2 Results

The first results for chirped laser slowing of CaF are shown in figure 6.11. Here the slowing beam is collimated with a diameter of $d_{1/e^2} = 6$ mm. The main slowing laser initially addresses molecules with a velocity around $v_{\text{start}} = 178$ m/s. Without chirping, the molecules are decelerated to about 100 m/s. With increasing chirp rate (and the same total chirp duration of 6 ms), the slow peak is pushed to lower velocities down to 50 m/s. At the same time the velocity width of the slowed bunch is reduced, indicating longitudinal cooling to about 100 mK, limited by the resolution of our detection method. Losses in molecule number are due to transverse heating and more importantly natural increase in divergence, since the transverse velocity spread is unchanged while the longitudinal velocity is decreased. Numerical simulations (done by Noah Fitch) that include these effects reproduce our experimental results very well without including additional losses. Independently, we searched for losses to the $N = 0$ and $N = 2$ rotational states and to the $v = 2$ vibrational state, by scanning a probe laser over transitions from these states. We found that these were all very small.

Figure 6.12 shows optimised chirp slowing to velocities of $v_{peak} = 15 \pm 2.5$ m/s. To achieve this, the beam is modified to now converge from $d_{1/e^2} = 18$ mm at $x' = 1.3$ m to $d_{1/e^2} = 3$ mm at the source. This adds a transverse force which helps to collimate the molecular beam and increases the number of molecules at the detector by roughly a factor of 2. The timing of the chirp is changed so that the free expan-

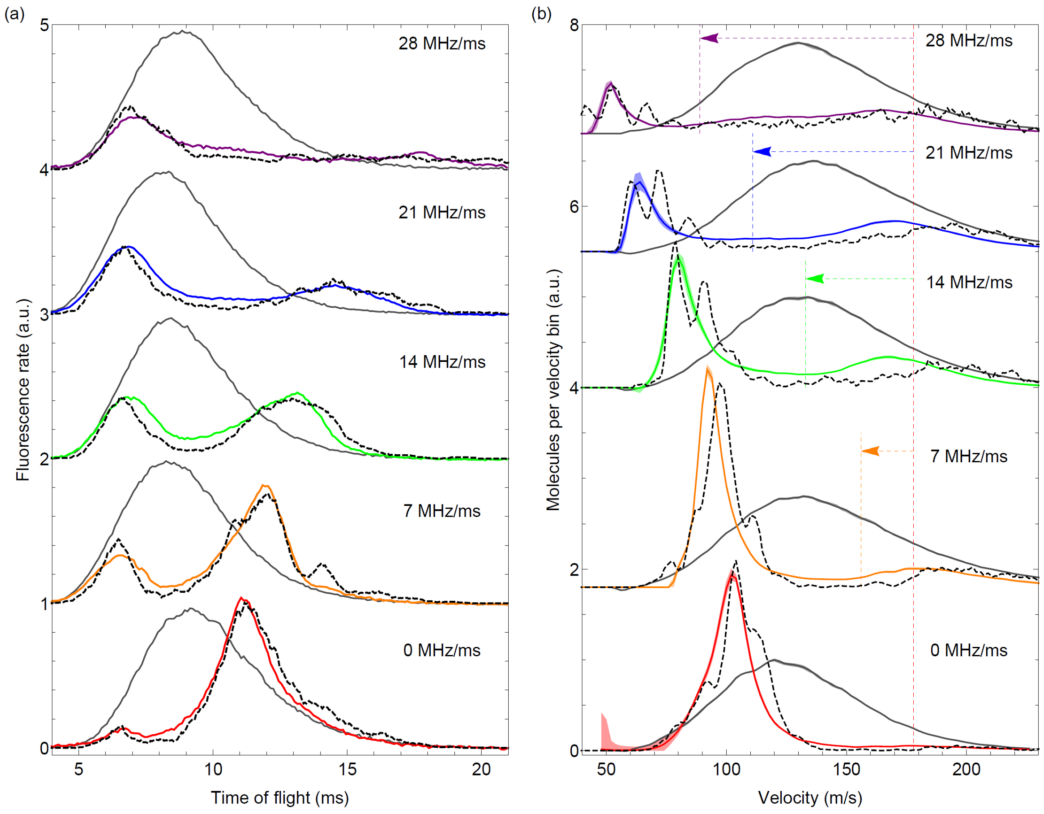

Figure 6.11: Time-of-flight profiles (left) and velocity distributions (right) of the molecular pulse in the chirp slowing experiment. The main slowing laser is initially addressing a velocity of 178 m/s, and is then chirped with various chirp rates over a duration of 6 ms. The black solid lines show the molecular pulse without slowing light applied, while the coloured solid lines show the pulse with slowing light applied at different chirp rates. The black dashed lines show numerical simulations. The widths of the coloured lines in the right figure indicate the uncertainty in determining the velocity distribution. Adapted from [82].

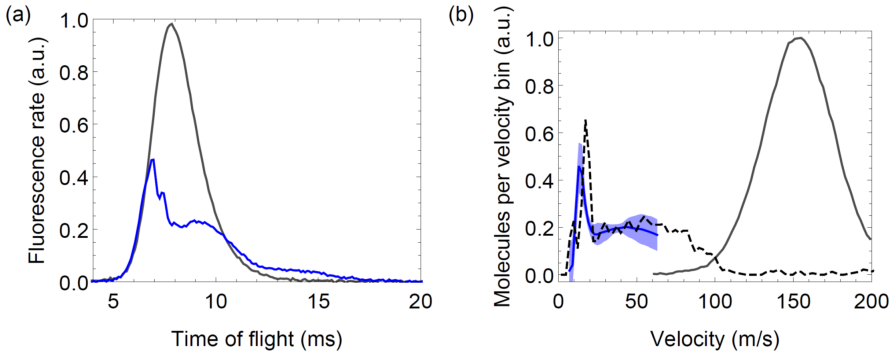

Figure 6.12: Optimised chirp slowing down to 15 m/s (see text). The black solid lines show the molecular pulse without slowing light applied, and the black dashed lines show numerical simulations. Left: Time-of-flight profiles. Right: Velocity distributions. The coloured bands indicate the uncertainty in determining the velocity distribution. Adapted from [82].

sion time between the end of the chirp and the detection is minimised. The chirp sequence is modified by first applying the slowing laser at a constant frequency for 1 ms before we start the linear chirp. We estimate that we slow about 10^6 molecules to velocities of 15 ± 2.5 m/s in a volume of 1 cm^3 at $x' = 1.3$ m. Molecules at these velocities should be trappable in a MOT.

We compare the chirp slowing method to the white light slowing method and find that while both work similarly well down to velocities around 50 m/s, we were not able to produce molecules near the capture velocity with white light slowing. Our explanation, backed by numerical simulations, is that in the white light slowing method molecules decelerate rapidly as soon as the light is switched on and many are lost due to divergence since they need to travel a long distance at low velocities [82]. This is in contrast to the chirp method, where the velocity is controlled and the slowest molecules join the slowing process later than the fast ones.

6.5 Conclusion

We find that the radiation pressure slowing method using chirped light is well suited for producing a beam of slow and cold CaF molecules. We were able to produce about 10^6 CaF molecules within the capture velocity and capture volume of a molecular

MOT. The downside of this method is that a large proportion of the initial molecule flux is lost due to divergence and transverse heating, as the method provides no transverse guiding.

The Zeeman-Sisyphus deceleration presented in this chapter might provide a more efficient and effective slowing method, since it combines slowing and guiding simultaneously. First tests are promising, showing a state switching efficiency of over 90 percent. It might even be possible to combine the ZSD with a short initial phase of laser slowing.

Chapter 7

Setting up the MOT chamber

As the design and setup of the MOT chamber is crucial for a successful realisation of a molecular MOT, some of the details will be presented here.

7.1 Overview

Our complete vacuum chamber is shown in figures 7.1 and 7.2, as well as on the photograph in figure 7.3. It consists of three parts: source chamber, slowing chamber and MOT chamber. The three parts are mechanically decoupled from each other via bellows to prevent vibrations from the cryo-cooler influencing the trap. The total distance between the source and the centre of the MOT is 120 cm. The molecules are produced in the buffer gas cell at $t = 0$ and exit it through a 3.5 mm aperture at position $x' = 0$. They travel through an 8 mm aperture at $x' = 25$ cm into the slowing chamber and later into the MOT chamber through a 20 cm long differential pumping tube with 20 mm diameter starting at $x' = 85$ cm. There are photo-multiplier tubes (PMTs) to detect the molecules via laser induced fluorescence at $x' = 20$ cm and $x' = 75$ cm before they reach the MOT chamber. In the MOT they can be detected on a CCD camera or alternatively with an additional PMT (PMT 2) that is inserted instead of it.

The MOT chamber is an 8 inch spherical octagon with a tee on top to attach the turbo pump without obstructing the MOT beams. The anti-reflection coated chamber windows[1] are attached to long nipples to reduce background scattering

[1] Torr Scientific VPZ38QBBAR

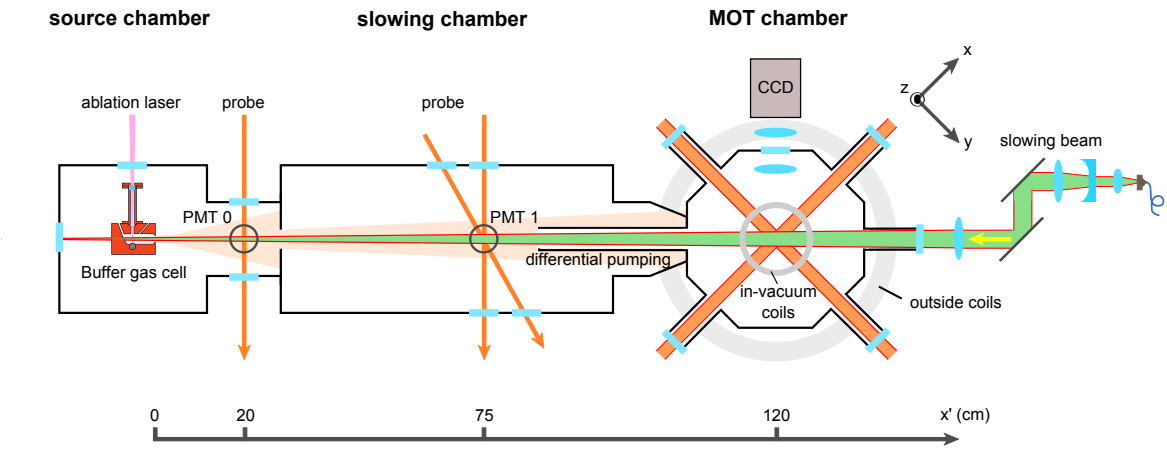

Figure 7.1: Schematic drawing of the experimental setup, top view.

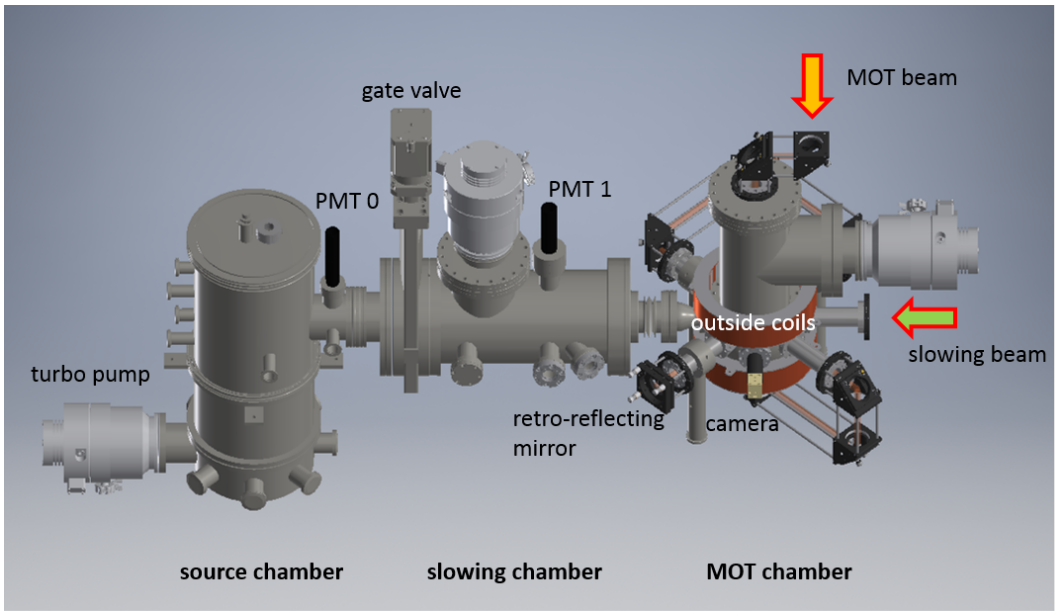

Figure 7.2: Drawing of the experimental setup. The outside MOT coils are shown but were replaced by in-vacuum coils later. MOT and slowing beams are fed in from optical fibres.

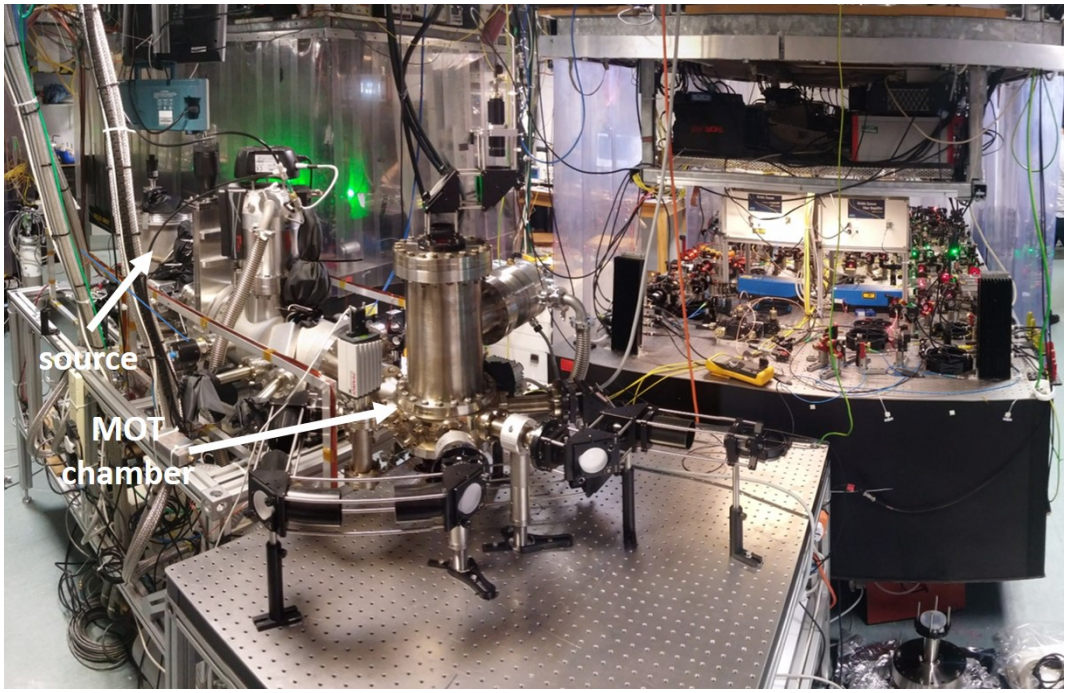

Figure 7.3: Photo of the experiment.

from room light.

7.2 Vacuum preparation

All parts going into the vacuum chamber, as well as the chamber itself, are carefully cleaned. Clean latex gloves should be worn at all times, since a single finger print can ruin the previous cleaning effort. The cleaning procedure starts with an ultrasonic bath in a 60 °C warm solution of water with *Decon 90* detergent to remove grease and oils. This is followed by a second bath in de-ionised water to remove the detergent. Afterwards the parts are wiped with solvent, first with acetone and then methanol, which gets rid of the acetone.

Since the MOT chamber is the most critical part, we pre-bake it for a few days in an oven at 250 °C under vacuum ($< 10^{-2}$ mbar). The high temperatures help to get rid of hydrogen impurities in the stainless steel.

Now the vacuum chamber can be assembled. We use copper gaskets only, as they are bakeable to high temperatures and provide good sealing in the UHV regime. With

a single turbo pump of 250 l/s pumping speed, connected to a pre-vacuum line at 5×10^{-3} mbar (pumped by a small turbo pump, 60 l/s), we reach about 1×10^{-7} mbar in the MOT chamber.

The next step is baking. We bake the whole chamber at a temperature of a slightly above 100 °C for around 1 week. The heat is provided by heating tapes while the chamber is completely covered in tin foil and additional thermally insulating materials. It is important to not let any part (especially the windows) cool down much below the average temperature, since this might lead to accumulation of residual gases there. Both heating and cool down rates should not exceed 1 K/min to reduce mechanical stress in the windows. The maximum baking temperature depends on the materials used, in our case the PEEK in the MOT coils (see section 7.3.2), which enters the glass phase at 143 °C. After cooling down, the pressure now reaches the lower limit of the pressure gauge of 5×10^{-10} mbar. While the experiment is running with a constant flow of 1 sccm of Helium, the pressure in the MOT chamber rises to 2×10^{-9} mbar. As shown experimentally in section 8.3.3, this pressure is low enough to not be the limiting factor in the lifetime of the MOT. The pressure in the slowing chamber during the experiment is 6×10^{-8} mbar.

7.3 MOT coils

Magneto-optical traps require a magnetic field gradient of about 10 G/cm. The usual setup is the anti-Helmholtz-configuration, in which two circular coils of radius r are placed at a distance $d = r$ on top of each other and run with currents I in opposite directions. The axial and radial magnetic field gradients of these coils on axis from the centre are

$$\frac{dB}{dz} \approx 3\mu_0 I \frac{\frac{d}{2} r^2}{((\frac{d}{2})^2 + r^2)^{5/2}}, \tag{7.1}$$

$$\frac{dB}{d\rho} = \frac{1}{2}\frac{dB}{dz}. \tag{7.2}$$

In equation 7.1, the approximation is valid when $z \ll d$. The molecules will be trapped in the zero of the magnetic field in the centre of the coils.

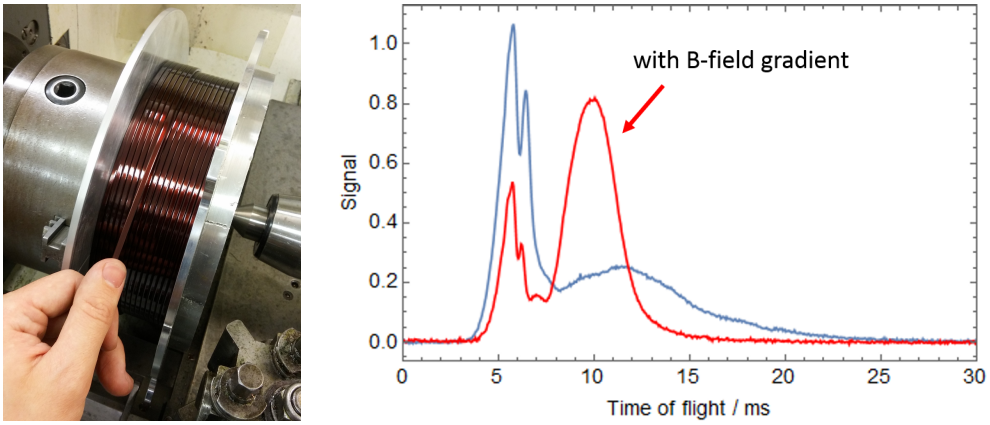

Figure 7.4: Left: The large outside coils are wound by hand. Right: Time of flight measurement of laser slowed molecules in the MOT chamber. When running the coils (red curve), the molecules don't reach the lowest velocities (corresponding to late arrival times) that they reach with the coils switched off (blue curve).

7.3.1 MOT Coils outside the vacuum chamber

The first version of MOT coils were designed to be placed outside the vacuum. They had a radius of $r = 117.5$ mm (averaged over all turns) and consisted of $N = 256$ rounds of copper wire each. Due to geometrical constraints they were placed at a distance of $d = 140$ mm (between the middle of the coils), slightly larger than r. According to equation 7.1 this predicts radial and axial magnetic field gradients of $dB/dz = 1.95$ G/cm and $dB/d\rho = 0.97$ G/cm per 1 A current, which was confirmed by measurement within 3 percent uncertainty.

Unfortunately the Zeeman shift of the coils was found to shift the molecules out of resonance during the chirped laser slowing, so that lowest velocities couldn't be reached anymore (See figure 7.4). The time constant $\tau = L/R$ was too large to switch the coils on only when the molecules reach the MOT region. It was decided to go for smaller coils with lower inductance L, which need to be inside the MOT chamber to reach the same field gradients.

7.3.2 MOT coils inside the vacuum chamber

Moving the coils into the chamber poses a few challenges. Materials with low outgassing rates have to be chosen, ideally allowing baking without damage. The size

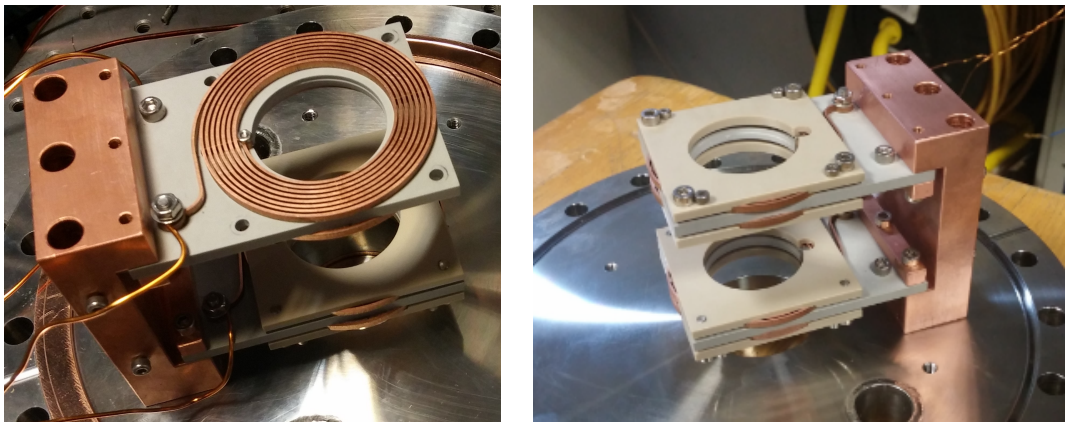

Figure 7.5: Left: In-vacuum coils with removed PEEK plate shows the copper spiral. Right: Complete MOT coil setup.

of the coils can't be too small, since there has to be optical access for all MOT beams and the slowing beam. Another thing to consider is the heat dissipation of the coils: Since there is no air convection like outside the chamber, the coils need to be carefully heatsunk using materials with high thermal conductivity. Figure 7.5 shows our final design. The coil setup consist of 4 copper spirals, 2 connected ones on the top and 2 connected ones on the bottom. The spirals are laser-cut in our mechanical workshop with a thickness of 0.8 mm and a height of 2 mm, with 8 rounds per spiral. The spiral pairs are inserted between a shapal[2] plate and a two PEEK[3] plates (see figure 7.5). The distance of the centre of the shapal plates is $d = 38.3$ mm and the central radius of the spirals is $r = 20$ mm. The shapal plates are mounted onto a copper block, which forms the thermal connection to the bottom flange of the MOT chamber. The top and bottom coils are not connected to each other and can be driven individually.

The magnetic field gradients produced by the setup are measured and found to be $dB/dz = 2.55$ G/cm and $dB/d\rho = 1.26$ G/cm per 1 A applied to all coils. This agrees reasonably with the calculated values of $dB/dz = 2.87$ G/cm/A and $dB/d\rho = 1.43$ G/cm/A. The zero of the magnetic field coincides with the geometrical centre of the

[2]Shapal is a ceramic with excellent machineability, great thermal conductivity and low outgassing.

[3]PEEK (polyether ether ketone) is a polymer with great machineability, but a much smaller thermal conductivity

coils within 0.5 mm.

The total resistance of the coil setup is about 0.04 Ω, so 10 A would dissipate $P = I^2 R = 4$ W of heat. With the thermal conductivity of 92 W/(K m) and a cross-section area of 100 mm^2 at a length of 70 mm, the temperature difference between the shapal plate edges should be 30 degrees. While shapal is a ceramic and highly heat resistant, PEEK enters the glass phase at 143° C. In the experiment we see a pressure rise at the 10^{-7} mbar level when the coils are run continuously for more than 10 minutes which could be due to overheating of the PEEK plates[4]. We avoid this by switching the coils off[5] between experimental shots (2Hz repetition rate, duty cycle¡50%) while they are not needed.

7.4 MOT beams

Due to limited available laser power we choose a single-beam configuration in which the MOT beam is sent through the chamber in 3 directions and then retro-reflected. While this uses the full available power without having to split beams, it has several disadvantages. It complicates the alignment of the laser beams because spatial dimensions are coupled to each other. It also leads to an imbalance in the MOT forces from each beam since each pass through the chamber reduces the laser power by a few percent. We compensate for this by slightly focussing the MOT beam to achieve equal intensity in each beam.

The MOT optics are attached to the MOT chamber in a 2 inch cage mount system for maximum stability. The light is fed in from the top out of a single PM fibre coming from the beam combining system described in chapter 5.5. It is then expanded to the final beam size of 16.2 mm ($1/e^2$ diameter).

7.4.1 Polarisations

Choosing the correct polarisation of the six MOT beams is crucial. Coming from the fibre the MOT beams are linearly polarised. For each pass through the chamber, quarter-wave plates in front of the MOT windows turn this into circular polarisation

[4]This prediction was later confirmed when we opened the chamber, the PEEK had started to melt where it touched the coils. It has now been replaced by shapal plates as well.

[5]coil current is controlled by a KEPCO BOP bipolar power supply.

at entry and turn it back into the initial linear polarisation after exiting the chamber. We here use the definition of the handedness of the circular polarisation as relative to the direction of the k-vector of the laser beam. In this definition, the incoming, vertically downwards pointing beam needs to have the same handedness as the sixth and final pass vertically upwards through the chamber. The 4 horizontal passes on the other hand need to have the opposite circular polarisation. All polarisations are carefully checked before the MOT experiment starts.

The $\mathcal{L}_{00}$ cooling light in the MOT chamber consists of components with different circular polarisations: The frequency sideband addressing the upper $F = 1$ hyperfine level has the opposite handedness compared to the other three frequencies. The reason for this is that most of the trapping force in our MOT come from a dual-frequency effect [76]. The MOT forces will be discussed in chapter 8.1.

7.5 Molecule detection

We detect the CaF molecules in the MOT by imaging their fluorescence at 606 nm onto a camera. There is however a problem: If the molecule numbers are very small, the fluorescence signal could be easily overpowered by a strong background of light scattered from the cooling laser. Since this laser runs at the same wavelength as the fluorescence, unlike the slowing and repump lasers it can't be attenuated by interference filters. We solve this with two methods. First, we use an in-vacuum lens to cover a large solid angle and collect as much fluorescence as possible. This also increases the amount of background photons, but increases the signal to noise ratio since the noise rises with the square root of the background photon number. Secondly and more importantly we blacken the chamber and reduce the background scattering directly, as described in section 7.6.

There is a way to image the molecules almost background-free by transferring them into another state and collecting the fluorescence at a different wavelength while filtering out the cooling light, but this is less direct and reduces the signal level substantially [88].

7.5.1 Imaging setup and detection efficiency

We image the molecules with a simple two lens telescope setup of magnification $M = 0.5$ (see figure 7.8). The in-vacuum lens has a diameter of $d_1 = 50.8$ mm and a focal length of $f_1 = 60$ mm. It is positioned at a distance equal to its back focal length of 49.1 mm from the centre of the MOT chamber. The lens collimates the fluorescence light collected from the molecule cloud, which then passes the chamber window of inner diameter $d_w = 38$ mm. Finally a second lens ($f_2 = 28.6$ mm, $d_2 = 40$ mm) outside the chamber focuses the light onto the chip of a CCD camera, positioned 18.8 mm behind the back face of the second lens. The imaging setup is carefully tested using an LED array as light source before adding it to the chamber. To calculate the solid angle covered by the first lens, we should only take into account the part that later passes through the window of diameter d_w. We get

$$\Omega = \pi \frac{(d_w/2)^2}{f_1^2} = 0.32\,. \tag{7.3}$$

This leads to a geometrical efficiency $\eta_{\mathrm{geo}} = \frac{\Omega}{4\pi} = 0.025$, which was confirmed independently by a ray tracing algorithm. The geometrical efficiency has to be multiplied by the transmission efficiency through window and optics $\eta_t = 0.90 \pm 0.03$ to get the collection efficiency of photons onto the camera, $\eta_{\mathrm{col}} = \eta_{\mathrm{geo}}\eta_{\mathrm{t}} = 0.023 \pm 0.001$. Finally, taking into account that only a fraction $\eta_{\mathrm{qe}} = 0.7$ of the arriving photons gets detected and generates an electron, we get the total detection efficiency

$$\eta_{\mathrm{det}} = \eta_{\mathrm{geo}}\eta_{\mathrm{qe}}\eta_{\mathrm{t}} = 0.016 \pm 0.001\,. \tag{7.4}$$

We hence detect $1.6 \pm 0.1\%$ of all photons emitted by the molecules, assuming isotropic emission. The additional line filter shown in figure 7.8 reduces this to 1.4%, but was added after the measurements presented in this thesis.

7.5.2 CCD Camera

It is crucial to choose a camera suitable for our purpose. A high quantum efficiency and a large sensor are desirable. Most importantly, the noise inherent to the camera's operation should be small enough to not be the limiting factor in the detection.

There are different types of noise:

- **Read noise** is created every time a pixel is read out. Binning pixels electronically before the readout reduces the importance of this noise factor. Read noise is independent of the exposure length.

- **Dark current** is a noise source present over the whole exposure time. It comes from thermally generated electrons in a pixel, so it can be reduced substantially by cooling the chip to a colder temperature.

- **Intensity noise** of the lasers will influence both the background light level and the molecule fluorescence, but with less than 1 percent it should not be the limiting factor here.

- **Shot noise** finally comes from the statistical nature of photon emission itself and can't be avoided. For a background level of N thermal photons in a pixel we expect $\sqrt{N}$ root-mean-square (RMS) noise.

After extensive research a Hamamatsu *ORCA R2* cooled CCD camera was chosen. It has a quantum efficiency of $\eta_{\mathrm{qe}} = 0.7$, meaning that 70% of the photons arriving on the chip will generate an electron and will be detected. The camera has an almost negligible dark current count rate of $D = 0.0005$ electrons/pixel/second while running at -40 °C. The RMS read noise is $N_{\mathrm{r}} = 6$ electrons, which is effectively reduced by factor 64 via binning of 8×8 pixels into one *superpixel*. The chip size is 8.67 mm × 6.60 mm with $1344 \times 1024 = 1.3 \times 10^6$ pixels, or $168 \times 128 = 2.2 \times 10^4$ superpixels.

7.5.3 Expected fluorescence per molecule

How many photons per second of wavelength 606 nm do we expect to detect with the camera from a single molecule? As before we can assume a scattering rate of 1.5×10^6/s . We know that 2.3% of those are collected onto the camera, which is 3.3×10^4 photons per second. Assuming a MOT radius of 2 mm, after demagnification the fluorescence will be imaged onto an area on the chip of 3.1 mm^2 containing 7.4×10^4 pixels. This is $P_{\mathrm{sig}} = 0.45$ photons/s in a single pixel and 28.8 photons/s in a superpixel. Since the MOT lifetime will be limited depending on the number

Figure 7.6: Left: In order of increased blackness from bottom to top: Soot, cupric oxide coated copper, Acktar spectral black foil. Right: Production of cupric oxide coating in a hot solution of NaOH and $NaClO_2$ in distilled water.

of repump lasers and possibly background collisions, let's assume an exposure time of 25 ms. This leads to 0.72 photons per superpixel per molecule in this exposure time.

7.6 Reducing background scattering

The main challenge in detecting our molecules is to reduce the background scattering caused by the cooling laser, since these photons are of the same wavelength as the molecule fluorescence and can't be filtered out. We have tested several methods to blacken the inside of the MOT chamber, which will be presented here.

7.6.1 Comparison of different blackening methods

The choice of a blackening method is mainly limited by its compatibility with ultra-high vacuum (UHV) and its price. The currently best UHV compatible black coating is VANTABLACK, which consists of carbon nanotubes and reflects less than 0.1 percent of visible light, but is unfortunately too expensive for large scale application[6] (though feasible for smaller surfaces). We instead test the following methods, none of which lead to a noticeable rise in pressure at the 10^{-8} mbar level when used in the vacuum chamber:

[6] about 300 pounds for a 100 cm^2 coating. Supplier is Surrey nanoSystems.

- **Soot** from an oxygen-acetylene flame. This is the simplest solution, cheap and available in our workshop. The soot has a matte finish and unfortunately comes off very easily.

- **MH2200 black paint**. This paint is best applied by spraying[7] and is well suited for complex geometries. It does not come off easily when touched.

- **Black foils** supplied by Acktar. They come as coated aluminium foils, well suited for covering flat surfaces, but less convenient for complex objects. We tried Scatter Black, with a matte soot-like finish, and Spectral Black, which has a glossy finish but is chosen because of its superior performance in reducing diffuse scattering.

- **Cupric oxide (CuO)**, which is grown on a copper substrate by immersing it in a heated chemical solution [133]. After initial tests (see figure 7.6) this method was dropped, as the results were slightly less black than the foils and the process requires handling of dangerous chemicals.

In order to compare the blackness of the different methods, one first needs to define it. The usual figures of merit are called hemispherical directional reflectance (HDR) and specular reflectance (SR). HDR is defined as the ratio of all light reflected into the hemisphere to the incoming light hitting a surface at angle θ_i. On the other hand, SR only takes into account the light that is reflected mirror-like at the same angle as the incident beam. At 45°, the specular reflectance of Acktar Spectral Black is measured as 0.6%, while the soot and CuO layers reach values of 0.2%.
In our setup the specular reflectance is of less importance, since there is no situation where light coming from the laser beams would be directly reflected towards the camera in a specular, non-diffuse way. To find the best material to use as a backstop directly opposite the camera, a laser beam at 606 nm is sent onto the test material at an incident angle α while the diffuse reflection towards the surface normal is measured by collecting the light onto the camera with a 1 inch diameter lens placed 10 cm from the sample (see figure 7.7). We find that Acktar Spectral Black performs best at all angles, so it is chosen as the material for the backstop.

[7]Spray painting should be done under the precautions stated in the Material Processing Guide, since the fumes can be a health risk.

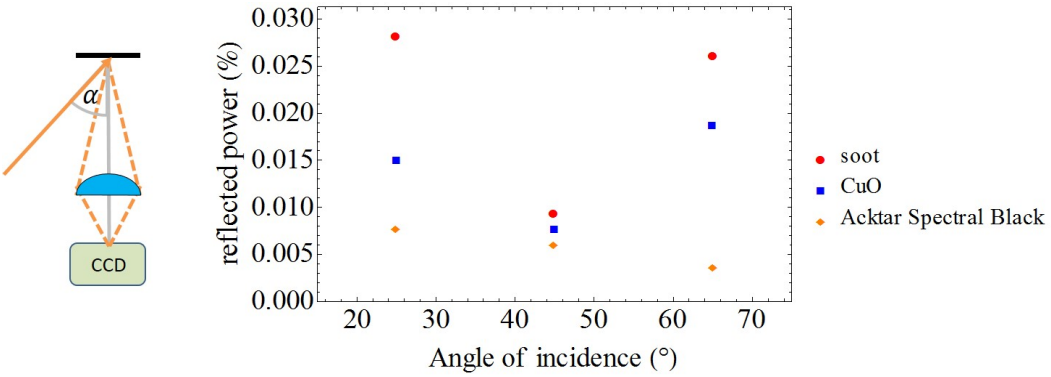

Figure 7.7: Left: Setup for comparing diffuse scattering from a laser at incident angle α onto the camera. The lens collects light from about 1% of the solid angle of the hemisphere. Right: Results of the scattering test, with the Spectral Black foil performing best.

7.6.2 Final setup

The final setup is shown in figures 7.8 and 7.9. We use Acktar Spectral Black foil as a backstop directly opposite the camera by covering the copper heatsink of the MOT coils. The MOT coils are spray-painted with MH2200 black paint. They are then placed inside an aluminium cylinder ($d = 145$ mm), which is spray painted as well and has apertures of 40 mm diameter for all beams. The cylinder is mounted on the bottom flange of our chamber, which is covered by Spectral Black foil. The black cylinder has two functions: It holds the in-vacuum lens and also absorbs stray light in the otherwise highly reflective MOT chamber. The background light is further reduced by a layer of soot along the long nipples and their transition to the chamber, as well as on the differential pumping tube.

7.6.3 Background scattering measurement

Before the MOT chamber is integrated into the experiment, the background scattering levels in the blackened chamber are investigated. First, the calibration of the *Orca R2* CCD camera as given by the manufacturer is independently confirmed by measurement (see Appendix D), resulting in good agreement. The manufacturer's value of 6.3 photons (corresponding to 4.4 electrons) on the chip per count in the software is accepted.

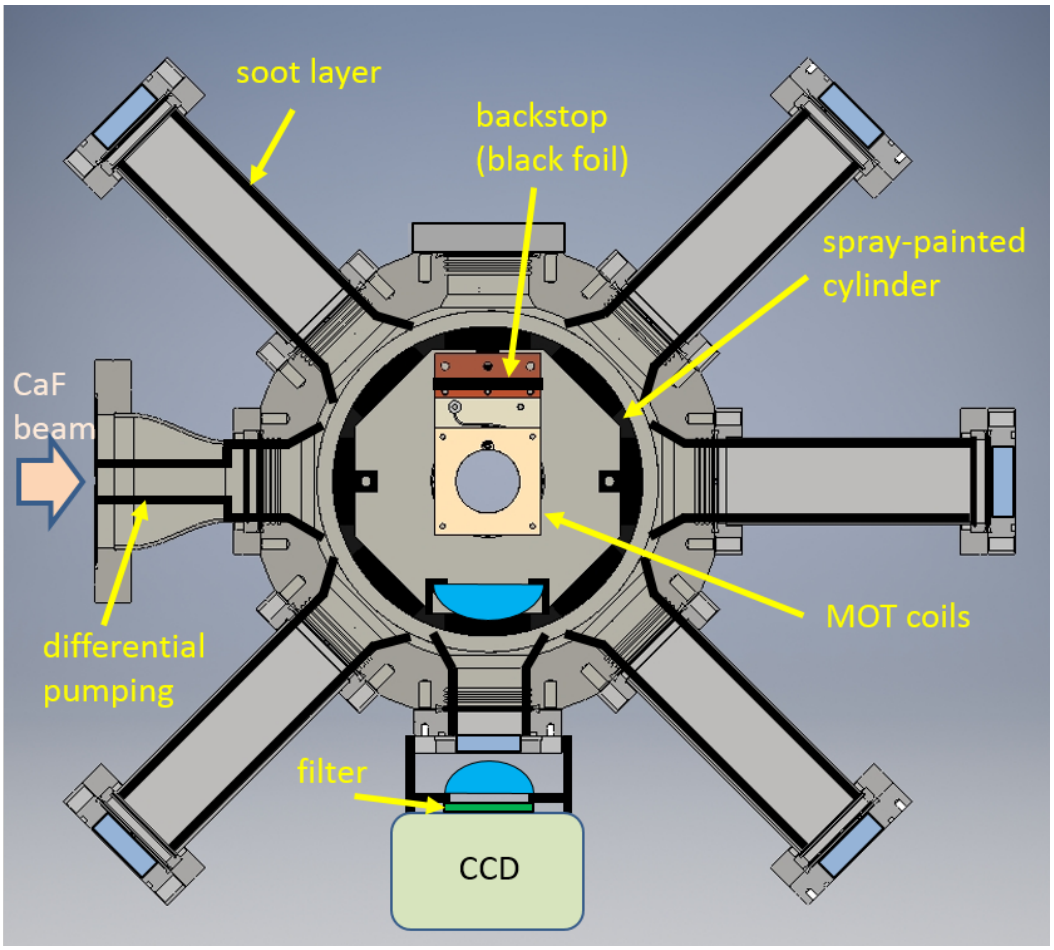

Figure 7.8: Drawing of the MOT chamber with the different blackening methods applied. The MOT coils are spray painted, but shown non-painted for clarity.

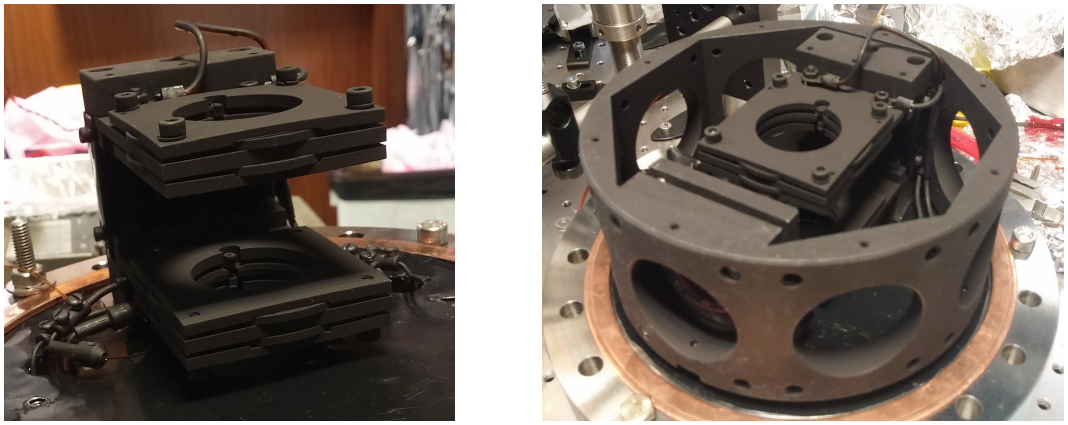

Figure 7.9: Left: spray painted MOT coils with backstop covered with Spectral Black foil. Right: Spray-painted cylinder with in-vacuum lens.

Now the MOT chamber and detection are set up, and the average background level in the central area of the chip (circle with $r = 2$ mm) is measured for various laser powers. We find a background count rate of 211 photons/s per single pixel, or $1.3{\cdot}10^4$ photons/s per superpixel, per 100 mW of laser power in each of the 6 MOT beams. Without the filter in front of the camera, both cooling and repump laser light add to the background. With a total power of 190 mW of cooling and repump light per beam, this leads to $P_{\mathrm{bg}} = 402$ photons/s/pixel (or 2.6×10^4 photons/s/superpixel). In 25 ms exposure this corresponds to 629 photons per superpixel. We hence expect a rms noise level of $\sqrt{629} = 25$ photons, corresponding to 18 electrons, about 3 times the specified read noise of 6 electrons per readout. At short exposure times below 1 ms the read noise can actually be the dominant factor.
The Signal-to-Noise Ratio (SNR) of a superpixel per molecule can be found via the formula [134]

$$\mathrm{SNR} = \frac{M_{\mathrm{bin}} P_{\mathrm{sig}} \eta_{\mathrm{qe}} t}{\sqrt{M_{\mathrm{bin}}(P_{\mathrm{sig}} + P_{\mathrm{bg}})\eta_{\mathrm{qe}} t + M_{\mathrm{bin}} D t + N_{\mathrm{r}}^2}}\,. \tag{7.5}$$

With $M_{\mathrm{bin}} = 64$ pixels in a superpixel at an exposure time of $t = 25$ ms, and given the values of quantum efficiency η_{qe}, dark current count rate D and read noise N_{r} of our camera, we calculate a value of SNR = 0.023 per superpixel per molecule. If we integrate over the area of interest on the chip (assumed as 3.1 mm^2, containing 1100 superpixels), the SNR increases by the square root of the number of superpixels, $\mathrm{SNR}_{\mathrm{total}} = \sqrt{1100} \times 0.023 = 0.76$ per molecule. With the line filter added, the background count rate would be reduced to $P_{\mathrm{bg}} \approx 150$ photons/s/pixel, but the signal would also be reduced by the transmission of 80% at 606 nm. This leads to a slightly increased SNR = 0.028 per molecule in a single superpixel and $\mathrm{SNR}_{\mathrm{total}} = \sqrt{1100} \times 0.028 = 0.94$ integrated over the region of interest. This means that a single molecule in the MOT could possibly be detected, although experimentally challenging. In our experiment, clouds with about 100 molecules are routinely observed and clearly visible in a single shot after background subtraction.

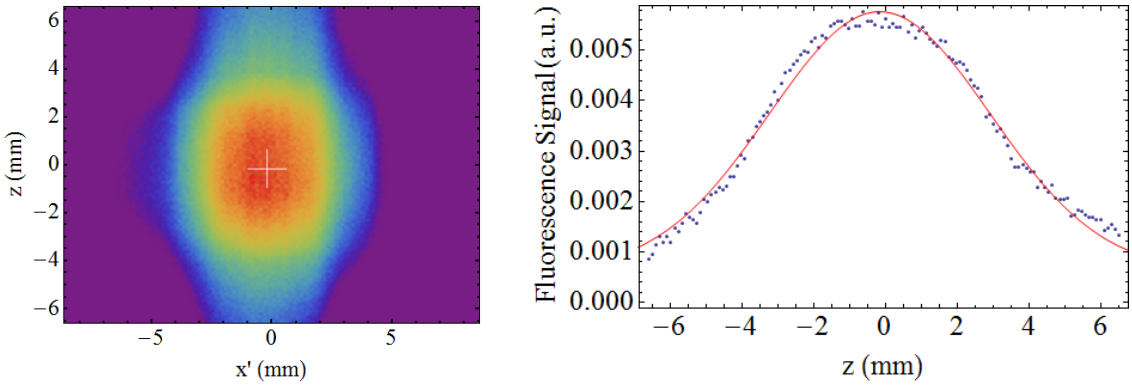

Figure 7.10: Left: Imaging the fast molecular beam in the MOT chamber. Molecules are flying from the right to the left and fill the whole imaged area, but are only detected where the probe beam hits them. Right: Vertical cut through the image at the position marked with the white cross, with Gaussian fit.

7.7 Imaging the molecular beam in the MOT chamber

A good first test that a cloud of trapped molecules would actually be detected on the CCD camera is to try detecting the fast molecular beam when it passes through the MOT area with all MOT beams present. With the MOT light on resonance, mainly the vertical beam will scatter photons, while the horizontal beams will be shifted out of resonance due to the Doppler shift, since they enter at an angle of 45 degrees to the molecular beam. While the molecule number in a MOT might be several orders of magnitude smaller than in the beam, trapped molecules will each scatter many more photons, especially when all 3 repump lasers are applied. With an expected lifetime of tens of ms compared to about 10 μs that a molecule at 150 m/s needs to cross the MOT area, detecting the molecules in the beam should be about as challenging as detecting the molecules in a MOT.

Figure 7.10 shows the imaged fast molecular beam in the MOT chamber (using 8×8 binning and 10 ms exposure). The diameter of the MOT beams is reduced to see the exact beam position on the camera. In the picture (and all following CCD images) the molecular beam enters from the right and gravity points downwards. The molecules fill the whole field of view, but are only detected where the vertical MOT beams hit them.

7.8 Summary and conclusion

This chapter has provided details on the MOT chamber used for making a MOT of CaF molecules. Let's summarise the results:

- A MOT chamber has been set up and baked and the final pressure is below 5×10^{-10} mbar (2×10^{-9} mbar while the experiment is running). A differential pumping stage separates it from the slowing chamber, where the pressure is 6×10^{-8} mbar during the experiment.

- In-vacuum MOT coils in anti-Helmholtz configuration have been installed, which provide 2.55 G/cm/A in axial direction (1.26 G/cm/A radially). The maximum B-field gradient is limited by the heating of the coils, but at least 20 A are possible, giving 50 G/cm.

- An imaging system with magnification of $M = 0.5$ and a total detection efficiency of 1.6% onto a CCD camera has been built and characterised.

- The inside of the chamber has been blackened by various methods, achieving a background count rate of 402 photons/s per single pixel on the camera chip with 190 mW laser power in each MOT beam. The expected fluorescence signal on the camera from a single molecule is 0.5 photons/s per pixel, leading to a SNR of about 1 (after binning the pixels and integrating over the whole region of interest).

- The optical setup for the MOT beams (in one-beam configuration) has been installed and the polarisations have been carefully checked.

- The fast molecular beam has been imaged with the camera to confirm the detection sensitivity.

In conclusion, we are now ready to make a MOT of CaF, provided that sufficiently slow molecules can be delivered to the centre to the MOT chamber.

Chapter 8

A magneto-optical trap of calcium fluoride molecules

This chapter presents the main result of this thesis, a magneto-optical trap (MOT) of CaF molecules. It begins with a brief explanation of the difference between type I MOTs (the usual choice for atoms) and type II MOTs (used for molecules). Next, the experimental procedure of making a molecule MOT will be explained. Finally, the most important properties of the trap are measured.

8.1 Forces in a type II MOT

Magneto-optical traps can be classified as either type I or type II. In a type I MOT, the total angular momentum F_u of the upper state of the laser cooling transition is larger than the angular momentum F_l of the lower state, $F_u > F_l$, while for type II MOTs the opposite is true, $F_u \leq F_l$. As we will see, this difference has consequences for the polarisations and detunings needed to achieve a trapping force. Molecular MOTs always use type II MOT transitions because they use the rotationally closed $N = 1 \rightarrow N' = 0$ transition.

Let's first look at type I MOTs, the "normal" case, used in atomic MOTs all over the world[1]. A type I MOT does not have dark states, since for every polarisation, all the ground state sublevels ($m_F = -F, ..., F$) can be addressed. Figure 8.1 a.) shows

[1] type II atomic MOTs have been demonstrated, but exhibit lower number densities and larger temperatures [49]

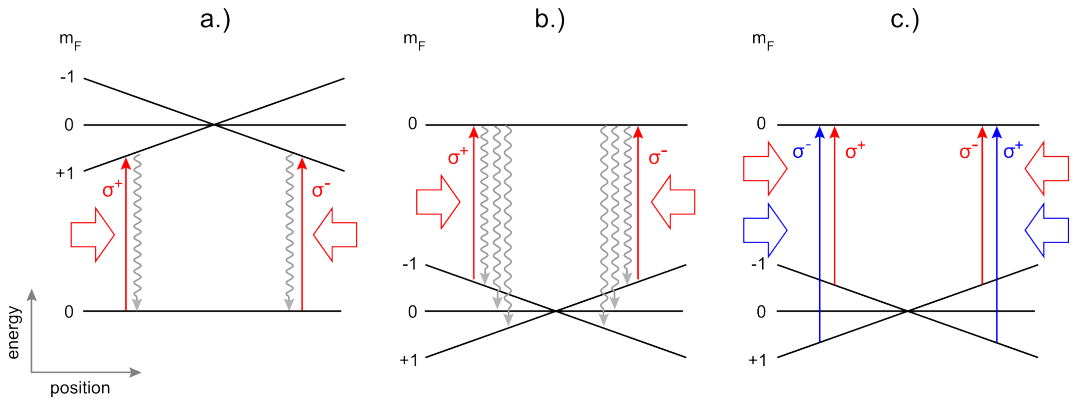

Figure 8.1: MOT scheme for type I and type II MOTs. **a.)** Type I MOT with $F_u = 1$ and $F_l = 0$. The excited state levels are shifted in energy proportional to the position dependent magnetic field and their magnetic quantum number m_F. Counter-propagating beams of opposite polarisation (solid arrows) create a confining force. **b.)** Type II MOT with $F_u = 0$ and $F_l = 1$. Here the ground state sublevels are shifted, and all three levels can be populated by spontaneous decay (wavy arrows), leading to zero net force (see text). **c.)** Same as b.), but with an additional blue detuned frequency of opposite polarisation in each MOT beam, leading to a net confining force.

the standard MOT scheme for a type I MOT with $F_u = 1$ and $F_l = 0$, assuming positive g-factors. There is only one ground state level, while in the excited state there are three levels, which are shifted in energy proportional to the B-field $B(z) = \frac{dB}{dz} z$ and their magnetic quantum number m_F. For a molecule at positive z position, the $m_F = -1$ sublevel of the excited state is shifted into resonance with the red detuned light, so it will dominantly scatter photons from the σ^- laser beam. Since this beam is pointing in the negative z direction, the molecule is pushed towards the center of the MOT. After excitation, the molecule decays back into the $m_F = 0$ ground state. At negative z positions, the whole process is mirrored: Now the $m_F = +1$ state is shifted into resonance, leading to a confining force from the σ^+ beam, which counter-propagates to the σ^- beam.

The situation is quite different if we look at a type II MOT with $F_u = 0$ and $F_l = 1$ (figure 8.1 b). Applying the same red detuned, counter-propagating lasers of opposite handedness does not lead to a confining force. For example, consider a molecule at positive z position in the $m_F = +1$ ground state. The molecule will ini-

tially absorb a photon from the confining σ^- beam, which excites it to the $m_F = 0$ upper state. From there it can decay into any of the three magnetic sublevels. If it decays into the $m_F = -1$ state, it cannot be addressed by the σ^- beam, but will instead absorb a photon from the anti-confining σ^+ beam to reach the $m_F = 0$ upper state. Since the σ^+ light is far detuned from the blue shifted state, this will take a long time, but will nevertheless occur eventually. If the molecule decays into $m_F = 0$ at some point, it will be dark to both lasers, but will eventually turn bright again, for example via Larmor precession in the magnetic field of the MOT. Since the spontaneous decay into the $m_F = -1$ and $m_F = +1$ is equally likely, there is no net confining force on the molecule, as they scatter an equal number of photons from confining and anti-confining beams. It has been shown that the same kind of symmetry leads to zero net force whenever the upper state Landé factor g_u is zero [63] (even in type I MOTs). This is problematic, since the $A^2\Pi_{1/2}$ state has a g factor very close to zero.

There is a way to create a net confining force in our type II MOT (even with $g_u = 0$). As shown in figure 8.1 c.), we can add an additional laser frequency in each beam, which is blue detuned and has a polarisation opposite to the already existing red detuned component. Considering the same situation, with a molecule at positive z position in $m_F = +1$, there are now two laser beams with σ^- polarisation that could excite it to the upper state. However, at this position the confining red detuned beam is closer to resonance than the anti-confining blue detuned one, and the molecules will dominantly scatter from it. As before, after excitation the molecule can decay into $m_F = -1$. This time however, there is a confining beam with σ^+ polarisation, which at this position is closer to resonance than the red detuned, anti-confining σ^+ beam. This leads to a net confining force. This explanation is simplified, as it does not take into account the Doppler shifts of moving molecules or the magnitude of the g factors of the states. A more complete description of this dual-frequency force based on rate equations can be found in [76]. Nevertheless we have presented a simple qualitative explanation of how to produce confining forces in a type II MOT where $g_u = 0$, without having to modulate the polarisations of the lasers and the magnetic fields (as done in [36]).

In our CaF MOT we use 4 laser frequencies with polarisations as shown in figure

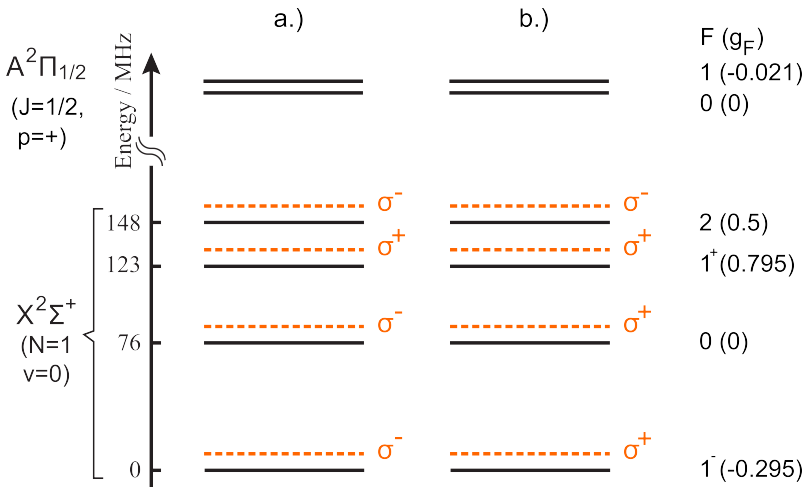

Figure 8.2: Hyperfine levels of the $X^2\Sigma^+$ state of CaF with choice of polarisation for the cooling laser. a.) polarisations used for trapping throughout this thesis. b.) optimum polarisations as proposed in [76], which however would lead to waste of laser power through beam combining. Energy separation and Landé factors g_F of each state are given [37].

8.2 a.), which all have a common red detuning of $\Delta = -0.75\Gamma$ to the four hyperfine levels of the $X^2\Sigma^+(N = 1)$ state. Our choice of polarisations differs from the optimum choice as proposed in [76] and shown in figure 8.2 b.), but it is simpler to produce without losing a lot of laser power via beam combining (see section 5.5), and was simulated to give similar trap properties. Since the $F = 2$ and $F = 1^+$ levels are separated by only 3Γ (=25 MHz), the $F = 2$ state is effectively addressed by both a red and a blue detuned laser, which have opposite handedness. According to the model in [76], this dual frequency effect contributes most of the trapping force on the $A - X$ transition. When it was switched off in the model by artificially increasing the separation between the hyperfine states, the maximum acceleration was reduced by a factor of six.

The same paper also investigates whether a MOT of CaF runs better on the $A^2\Pi_{1/2} \rightarrow X^2\Sigma^+$ or the $B^2\Sigma^+ \rightarrow X^2\Sigma^+$ cooling transition [76]. It finds that the $A - X$ transition is favoured due to a higher capture velocity (20 m/s compared to 10 m/s on $B - X$) while both have comparable trapping and damping forces. We therefore choose the $A - X$ transition for trapping, even though the less favourable Franck-Condon factors require us to use 3 repump lasers instead of possibly only one.

8.2 Check-list for making a molecular MOT

Let's summarise the things that should be checked when looking for the first MOT signal.

- Molecular source, skimmer, slowing laser beam and center of the MOT coils are well aligned on one axis.
- The pressure in the MOT and slowing chamber is low enough, while the source is running (about 10^{-9} mbar in the MOT chamber and 10^{-7} mbar in the slowing chamber are fine).
- The polarisations of the MOT beams are correct.
- MOT beams are balanced in intensity and well aligned (use irises). With large beam diameters the overlap is less critical.
- The B-field magnitude and direction of the MOT coils is correct (or just alternate between both directions between shots).
- B-field for remixing dark states along slowing chamber is sufficient.
- The detection (PMT or CCD camera) is sensitive enough, can detect the molecular beam.
- The molecular source is as bright and slow as possible.
- The laser slowing works down to velocities of about 15 m/s. The slowing light should be turned off afterwards, as it disturbs the trapping process.
- Cooling and repump lasers are all locked at the right detuning, have correct sidebands and are stable (check via spectroscopy).

Given that all these requirements are fulfilled, the MOT should just work. With our very stable setup, from the molecular source to the optical setup, the vacuum system and detection, we routinely trap molecules within the first hour in the lab, leaving a lot of time for further experiments.

8.3 Results

8.3.1 First magneto-optical trapping of CaF

The first CaF MOT was detected with a photo-multiplier tube (PMT) instead of the camera, although it was soon found that the camera detects the molecules equally well. Figure 8.3 shows the time-of-flight fluorescence signals of a molecular beam pulse passing through the MOT region. The grey dashed line shows the free molecular beam, without slowing lasers applied. The red line shows the molecular pulse being slowed via the frequency chirped slowing method (as described in section 6.4 and [135]), but not trapped in the MOT because the MOT magnetic field is in the wrong direction. Finally, the blue line shows trapped molecules (still fluorescing after $t = 30$ ms), with the MOT magnetic field in the correct direction. Blue and red data originate from the same experimental run, in which the direction of the current is switched in alternating shots to see the trapping more clearly.
In both the MOT and the anti-MOT case, the cooling laser $\mathcal{L}_{00}$ and the first two repump lasers $\mathcal{L}_{10}$ and $\mathcal{L}_{21}$ are present at all times, at powers of 80 mW, 100 mW and 10 mW per beam in the chamber, respectively. Unless noted otherwise, these powers are used in all following MOT experiments. The repump lasers are on resonance while the cooling laser is red detuned by $\Delta \approx -\Gamma$.

We confirm the MOT by taking a picture with the CCD camera. With the magnetic field fixed in the correct MOT configuration, the CCD camera is triggered at $t = 20$ ms for an exposure time of $t_e = 25$ ms, averaged 100 times. The result is shown in figure 8.3, after subtraction of the background (where the ablation laser is switched off). We clearly see the molecular cloud, so the first trapping of CaF in a MOT is confirmed! Optimisation steps and the preliminary MOT properties will be presented in the next sections.

8.3.2 Initial observations

We first optimised the MOT for maximum brightness of the molecular fluorescence on the CCD camera. The optimum detuning of the cooling laser is found to be $\Delta = -0.75\Gamma$, with $\Delta = 0$ defined as the point where the MOT becomes unstable and only forms in 50% of the shots. We observe trapped molecules at detunings between

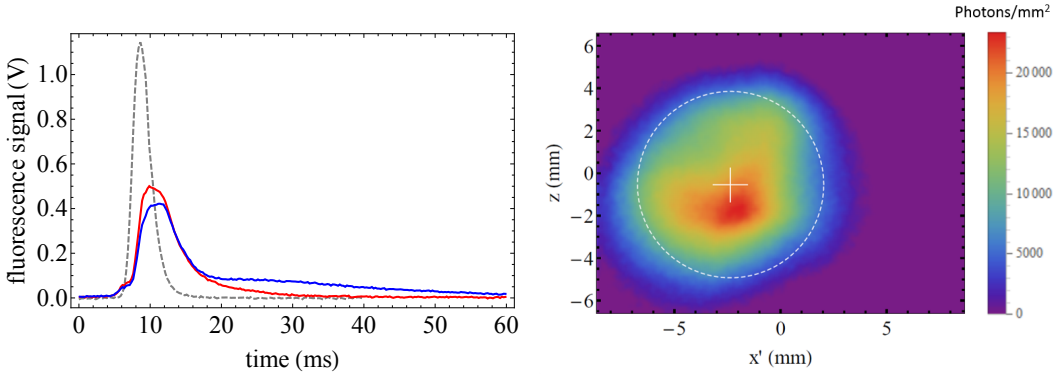

Figure 8.3: Left: Time of flight fluorescence signal of the first MOT of CaF. The blue line shows trapped molecules. The red line shows the signal when the MOT magnetic field direction is reversed so that a MOT cannot form. The gray dashed line shows the molecular beam without slowing. Comparison of MOT and anti-MOT signals shows that trap loading starts at about $t = 16$ ms, right after the slowing chirp sequence ends at $t = 15$ ms. Right: First image of the MOT on the CCD camera (25 ms exposure, starting at $t = 20$ ms, 100 times averaged, background subtracted). The colour scale from purple to red shows the amount of fluorescence collected during the exposure time. The white cross marks the center of the cloud, determined by Gaussian fits in z and x' direction. The white circle has a diameter equal to the average $1/e$ width of the fits, $d_{1/e} = 8.8$ mm. The integrated fluorescence of the cloud corresponds to 752 ± 47 molecules (see section 8.3.4).

0 and -1.8Γ. Higher laser powers of the cooling laser give higher fluorescence signals, which could however just be due to higher scattering rates[2]. The alignment of the laser beams is not too sensitive, probably due to our large beam diameters. The B-field gradient is not very critical either: values between 20 G/cm and 40 G/cm in the axial direction all produce similar results, with an optimum at 29 G/cm. The most critical parameters are those related to the source (optimising ablation) and the slowing process (amplitude and timing of the chirp).

We installed shim coils in the horizontal dimensions to move the zero of the magnetic field, while in the vertical direction we can do the same by slightly changing the balance in current between the MOT top and bottom coils[3]. The shim coils are optimised to give the maximum signal, which coincides well with overlapping the molecular cloud with the centre of the six MOT beams on the camera (found by imaging the molecular beam, as in figure 7.10).

8.3.3 Lifetime and scattering rate

The first thing to measure is the 1/e lifetime τ of the molecules in the MOT. There are several loss mechanism to be considered. First of all, every spontaneous decay into a state that is dark to our MOT lasers leads to loss of the molecule (mainly higher vibrational states). Secondly, collisions with the background gas in the MOT chamber can remove the molecules from the trap. The third mechanism we consider is the loss of the fastest molecules in the tail of the Maxwell-Boltzmann distribution, which can have enough energy to escape if the trap is not too deep. With these three loss channels, the total lifetime is given by

$$\tau = \left(\tau_{\mathrm{col}}^{-1} + \tau_{\mathrm{vib}}^{-1} + \tau_{\mathrm{ev}}^{-1}\right)^{-1} \tag{8.1}$$

where τ_{vib}^{-1} describes the loss rate due to decays into higher lying vibrational states, τ_{col}^{-1} is the loss rate due to collisions with the background gas, and τ_{ev}^{-1} is the loss rate due to evaporation of the fastest molecules from the trap.

With only 2 repump lasers, we expect decays to higher vibrational levels to be the

[2] It isn't, as we find later: A higher cooling laser intensity increases the number of molecules in the trap up to $I = 500\mathrm{mW/cm}^2$.

[3] we later added a third shim coil, but not for the data presented in this thesis

dominant loss channel. The molecules scatter about $3 \cdot 10^4$ photons before all but a remaining proportion of 1/e has decayed into the $v = 3$ vibrational state (where they are lost from the cycle). At a scattering rate of 1.5×10^6 s^{-1}, this predicts a lifetime of $\tau_{\mathrm{vib}} \approx 22$ ms, neglecting other loss channels. Adding the repump laser $\mathcal{L}_{32}$ should increase this lifetime to $\tau_{\mathrm{vib}} \approx 550$ ms, assuming the branching ratios presented in section 2.3 are correct. At this point the lifetime τ should be limited by other loss channels.

The collision rate with the background gas can be approximated by

$$\tau_{\mathrm{col}}^{-1} \approx \sigma_{\mathrm{bg}}\, n\, v_{\mathrm{bg}} = \frac{\sigma_{\mathrm{bg}} p \sqrt{2\pi k_{\mathrm{B}} T / m_{\mathrm{bg}}}}{k_{\mathrm{B}} T} \tag{8.2}$$

with the pressure p, number density n, collisional cross-section between CaF molecule and background gas σ_{bg} and mass m_{bg} and velocity v_{bg} of the background gas at temperature T. Assuming the main background gas to be He ($\sigma_{\mathrm{bg}} \approx 10^{-18}$ m, $m_{\mathrm{He}} = 4$ amu) at $T = 300$ K, at a background pressure of $p \approx 2 \cdot 10^{-9}$ mbar, we estimate a collisional rate of $\tau_{\mathrm{col}}^{-1} \approx 0.096$ s^{-1}, leading to $\tau_{\mathrm{col}} \approx 10.4$ s. This estimation agrees with our observation that the lifetime of the molecules in the MOT does not change significantly when we intentionally increased the background pressure by an order of magnitude. The losses through collisions with the background gas can be mostly neglected at this point.

Another cause of loss of molecules from the trap is evaporation. If the trap depth U of the MOT is not much larger than the kinetic energy $k_{\mathrm{B}}T$ of the trapped molecules, the fastest molecules in the long tail of the Maxwell-Boltzmann distribution can escape the trap. After this the remaining molecules will quickly thermalise via the molecule-light interactions, so that a constant temperature and loss rate can be assumed. The radial temperature of the molecules is measured to be $T \approx 9$ mK (see section 8.3.5). The trap depth is approximately $U = \frac{1}{2} m \omega_\rho^2 (d_\lambda/2)^2$, where the spring constant is assumed constant up to an effective beam diameter d_λ, which we assume to be the 1/e diameter of the MOT beams. The radial trap frequency ω_ρ is used because the trap is shallower in radial than in axial direction. With $\omega_\rho = 2\pi \times (130 \pm 7)$ Hz (see section 8.3.6) and $d_\lambda = 11.4$ mm we estimate $U = k_B \times (77 \pm 9)$ mK, which is only about 8 times the kinetic energy of the molecules. We can estimate the loss

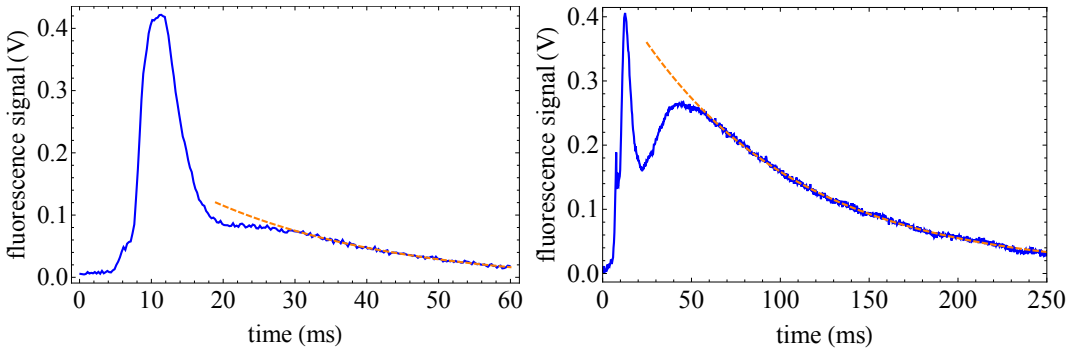

Figure 8.4: Left: Fluorescence signal of the MOT using only the $\mathcal{L}_{00}$, $\mathcal{L}_{10}$ and $\mathcal{L}_{21}$ lasers. The exponential fit gives $\tau = 30 \pm 3$ ms. Right: Same experiment with the third repump laser $\mathcal{L}_{32}$ added. Now the fit gives $\tau = 90 \pm 2$ ms. In both graphs the blue solid line is the time-of-flight data and the orange dashed line is the fit.

rate by $\tau_{\text{ev}}^{-1} = \frac{2\omega_\rho}{\pi} e^{-U/(k_{\text{B}}T)} = 0.1^{+0.5}_{-0.09}$ s^{-1} as done previously in [61]. This means that we predict a total lifetime according to equation 8.1 of $\tau = 22 \pm 1$ ms for a MOT using only the $\mathcal{L}_{00}$, $\mathcal{L}_{10}$ and $\mathcal{L}_{21}$ lasers, and a lifetime of $\tau = 520^{+20}_{-107}$ ms when the third repump laser $\mathcal{L}_{32}$ is added. The error on these predictions is large, since the loss rate depends exponentially on the trap depth, which isn't directly measured and could be over- or underestimated.

Figure 8.4 shows a lifetime measurement, where we record the time-of-flight fluorescence signal (blue curve) of the MOT with the PMT. In the left graph only the $\mathcal{L}_{00}$, $\mathcal{L}_{10}$ and $\mathcal{L}_{21}$ lasers are present. An exponential fit (orange line) to the falling slope of the form $f(t) = a + b \cdot e^{-t/\tau}$ gives $\tau = 30 \pm 3$ ms. On the right graph the $\mathcal{L}_{32}$ repump laser is added, which results in an increased lifetime of $\tau = 90 \pm 2$ ms. The power of the cooling laser is about 80 mW per beam in both cases, corresponding to a total intensity of about 400 mW/cm^2 in the chamber. Without the $\mathcal{L}_{32}$ repump, the lifetime is similar to the value estimated above and is dominated by decay to the $v = 3$ state. With the $\mathcal{L}_{32}$ repump added, the measured lifetime is smaller than predicted above (even given the large uncertainties on the prediction). This suggests that there might be an additional process limiting the lifetime, or that the assumptions in the calculation of the evaporation loss rate (e.g the effective trap diameter) were not correct.

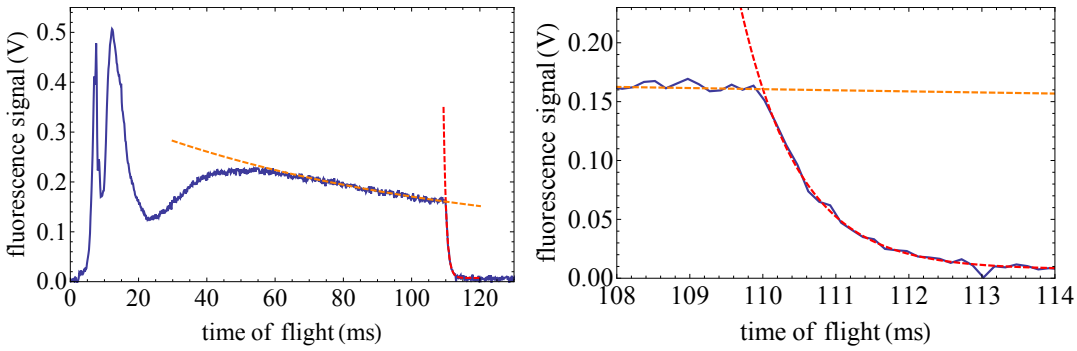

Figure 8.5: Left: Time of flight fluorescence signal in the MOT chamber, showing the initial loading phase (between $t = 20$ ms and $t = 50$ ms), followed by a slow decay up to $t = 110$ ms. At this time the $v = 2$ repump laser is switched off and molecules are optically pumped into the $v = 2$ vibrational state. The fast signal decay can be used to measure the scattering rate. The dashed lines show exponential fits with time constants of $\tau_1 = 93 \pm 12$ ms (orange) and $\tau_2 = 814 \pm 2\,\mu$s (red). Right: Zoom into the slope of the fast decay.

It is of highest importance to determine the scattering rate of the molecules in our MOT, since it allows us to calculate the number of molecules from the number of collected photons. We measure the scattering rate by first loading a MOT with the cooling laser and all three repump lasers present and then quickly switching off the $v = 2$ repump laser $\mathcal{L}_{21}$. This leads to a rapid decay of the fluorescence signal due to optical pumping into the $v = 2$ vibrational state on the time scale of one ms. The optical pumping rate is proportional to the scattering rate and inversely proportional to the known branching ratio into $v = 2$ (see section 2.3.1). For an exponential decay of the fluorescence signal with lifetime τ, the scattering rate is simply $\Gamma_{sc} = 1/(q_{02}\tau)$. Figure 8.6 shows the results of this measurement. The MOT is loaded as usual with $P = 80$ mW in the cooling laser and shows slow decay with a time constant of $\tau = 93 \pm 12$ ms, with the fit shown by the orange line. Then at $t = 110$ ms the repump laser $\mathcal{L}_{21}$ is switched off, resulting in rapid decay of the signal. An exponential fit (red dashed line) gives a time constant of $\tau = 814 \pm 2\,\mu$s. With the branching ratio of $q_{02} = 0.12\%$ this results in a scattering rate of $\Gamma_{\mathrm{sc}} = (1.47 \pm 0.01) \times 10^6$ s^{-1}.

We repeat the experiment for various laser intensities I of the cooling laser. The

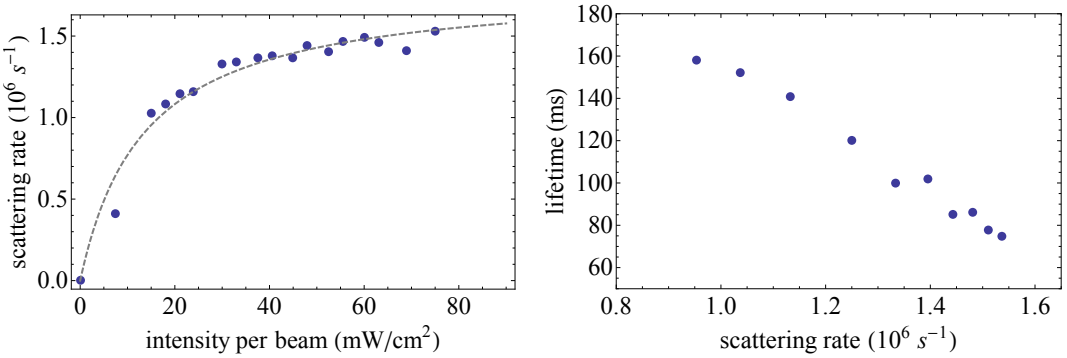

Figure 8.6: Left: Scattering rate of molecules in the MOT plotted against intensity per beam of the cooling laser $\mathcal{L}_{00}$. The dashed line is a fit according to equation 2.31, giving $\Gamma_{\text{eff}} = 2\pi \times (0.58 \pm 0.02)\text{MHz} = (0.070 \pm 0.002)\,\Gamma$ and $I_{\text{sat,eff}} = (5.1 \pm 0.8) I_{\text{sat}} = 25.0 \pm 3.6$ mW/cm^2. Right: Lifetime of the MOT vs scattering rate.

result is shown in figure 8.6. The gray dashed line is a fit according to equation 2.31, giving $\Gamma_{\text{eff}} = 2\pi \times (0.58 \pm 0.02)\text{MHz} = (0.070 \pm 0.002)\,\Gamma$ and $I_{\text{sat,eff}} = (5.1 \pm 0.8) I_{\text{sat}} = 25.0 \pm 3.6$ mW/cm^2. These values are about a factor of 2 smaller than expected from theory.

Finally we measure the lifetime of the MOT (with all three repump lasers) at different cooling laser intensities, which can now be translated into a scattering rate. In figure 8.6 on the right we see that the lifetime decreases strongly with increasing scattering rate. This seems to suggest a loss mechanism related to spontaneous decay into a dark state. However, different laser intensities lead to different temperatures of the molecules in the trap and different trap depths, which would change the evaporation rate of the hottest molecules from the trap, as explained earlier in this section. Further investigation will be needed to determine the loss mechanism.

8.3.4 Molecule number

Now that the scattering rate of the molecules is known, we can determine the number of molecules N_{MOT} in the MOT. For short exposure times t_{exp} (neglecting molecule losses from the trap during exposure) it is calculated by

$$N_{\text{MOT}} = \frac{N_{\text{ph,chip}}}{t_{\text{exp}} \eta_{\text{det}} R_{\text{sc}}}\,, \tag{8.3}$$

where $N_{\mathrm{ph,chip}}$ is the total number of photons detected on the chip in the exposure time, R_{sc} is the scattering rate and $\eta_{\mathrm{det}} = 1.6 \pm 0.1\%$ is the detection efficiency (see section 7.5.1). The number $N_{\mathrm{ph,chip}}$ is obtained by summing over the counts (after subtracting the background) in each pixel of the region of interest on the chip, and multiplying the total counts by the conversion factor $c = 4.4$. This conversion factor was provided by the manufacturer and has been independently confirmed by us in a calibration measurement, presented in appendix D.

It is important to choose a reasonable region of interest (ROI) over which the camera counts are summed up. Simply summing up the counts of all the pixels of the camera chip risks mistaking background light (which hasn't been perfectly subtracted) for molecule fluorescence, resulting in artificially high molecule numbers. On the other hand, summing over a region of interest that is too small will not count all the molecules in the MOT. The problem is solved in two steps, shown in figure 8.7, with data corresponding to the left image in figure 8.8. First we plot the number of collected photons $N_{\mathrm{ph,chip}}$ within a circle centred in the centre of the MOT vs the area of this circle. As expected, the photon number rises strongly in the beginning (when counting actual molecule fluorescence) and later shows a linear slope, collecting background light proportional to the collection area. The slope is determined by a linear fit $f(x) = mx + b$ over the last data points, in this case giving $m = (1.66 \pm 0.01) \times 10^5$. Now the linear slope $f(x) = mx$ is subtracted from the left graph, removing the effect of the background. The resulting curve approaches a constant value of $N_{\mathrm{ph,chip}} = (1.83 \pm 0.02) \times 10^7$ photons, determined by a fit on the last values in the graph. With $t_{\mathrm{exp}} = 100$ ms this corresponds to $(7.6 \pm 0.5) \times 10^3$ molecules.

The number of trapped molecules depends on many experimental parameters of the MOT, as well as the performance of the source and efficiency of the deceleration. With the same experimental parameters, the molecule number can vary by up to 25% from one day to another. A detailed characterisation of the MOT can be found in our recent publication [136] and will be the subject of a future PhD thesis. Instead we just present the highest number of trapped molecules at this time, which is $N_{\mathrm{MOT}} = (7.6 \pm 0.5) \times 10^3$ molecules for the molecular cloud shown in figure 8.8 on the left. This molecule number is the average number over the whole exposure time $t_{\mathrm{exp}} = 100$ ms, neglecting the losses from the trap during exposure. If we take

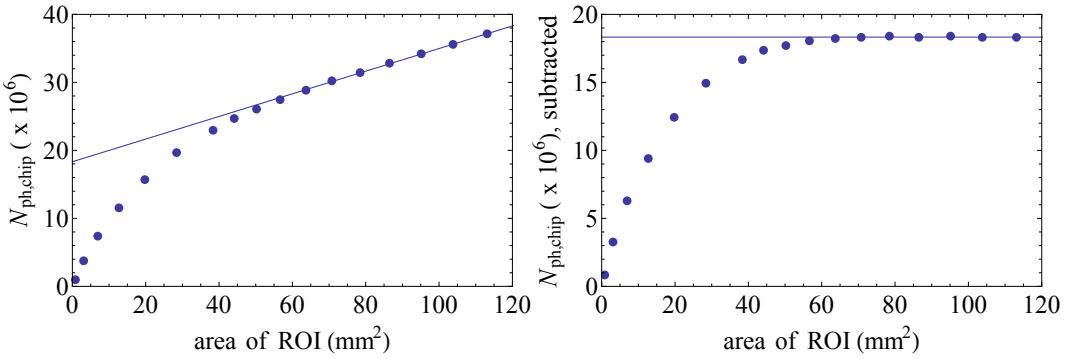

Figure 8.7: Determination of the molecule number in the MOT. Left: Number of collected photons within a circle of area A vs area of the circle, with linear fit (see text). Right: Same as left, but with the linear slope subtracted, removing the background photons.

losses into account, with a time constant of $\tau = 90$ ms, the resulting initial molecule number (at the start of the exposure) is $N_{\mathrm{MOT}} = (1.2 \pm 0.1) \times 10^4$.

On the right side of figure 8.8 we see a molecular cloud with only $N_{\mathrm{MOT}} = 121 \pm 8$ molecules, imaged for 10 ms, which demonstrates the exceptional sensitivity of our detection setup. Both images have their backgrounds subtracted. In both images the cooling laser has the full power of 80 mW per beam, all three repump lasers are present, and the magnetic gradient is $dB/dz = 29$ G/cm. After the optimization process the molecular cloud is significantly smaller and denser relative to the first MOT shown in figure 8.3, which could be explained by a lower temperature.

8.3.5 Temperature

We determine the temperature of the molecules in the MOT by observing their free expansion after we release them from the trap. The result is shown in figure 8.9. The molecules are released at $t = \tau_0$ by turning off the cooling laser and magnetic field, followed by a free expansion for a variable duration τ_{free}. Finally they are imaged with an exposure time of $t_e = 1$ ms by turning the MOT lasers back on. Since during the exposure time the molecular cloud is still expanding, we define the effective free expansion time $\tau = \tau_{\mathrm{free}} + t_e/2$ as half way through the exposure phase. During the exposure, there is no magnetic field (so no trapping) and the damping

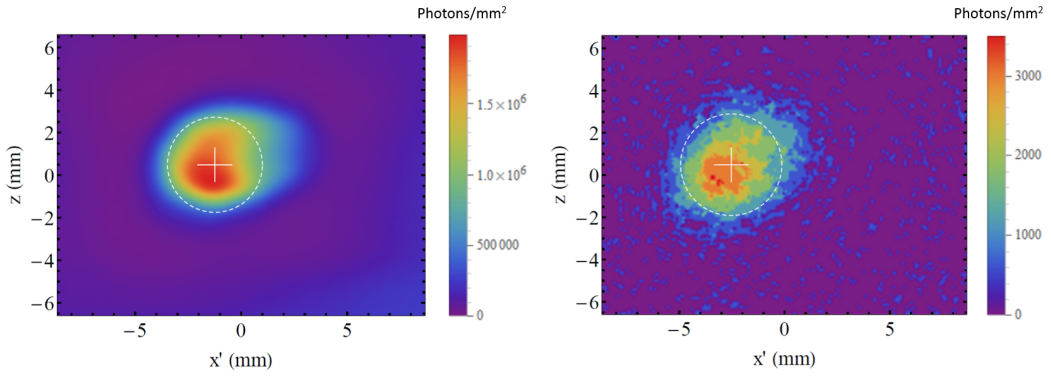

Figure 8.8: Images of the MOT with all repump lasers present. Left: Image of the MOT taken at $t = 20$ ms with $t_{\mathrm{exp}} = 100$ ms exposure time, containing $(7.6 \pm 0.5) \times 10^3$ molecules. The white circle shows the 1/e diameter $d_{1/\mathrm{e}} = 4.5$ mm of the cloud. Right: Image of the MOT, taken at $t = 330$ ms after most molecules have left the trap ($t_{\mathrm{exp}} = 10$ ms). The white circle shows the 1/e diameter $d_{1/\mathrm{e}} = 4.5$ mm and the MOT contains only 121 ± 8 molecules, demonstrating the exceptional sensitivity of our detection setup. Both images have their backgrounds subtracted.

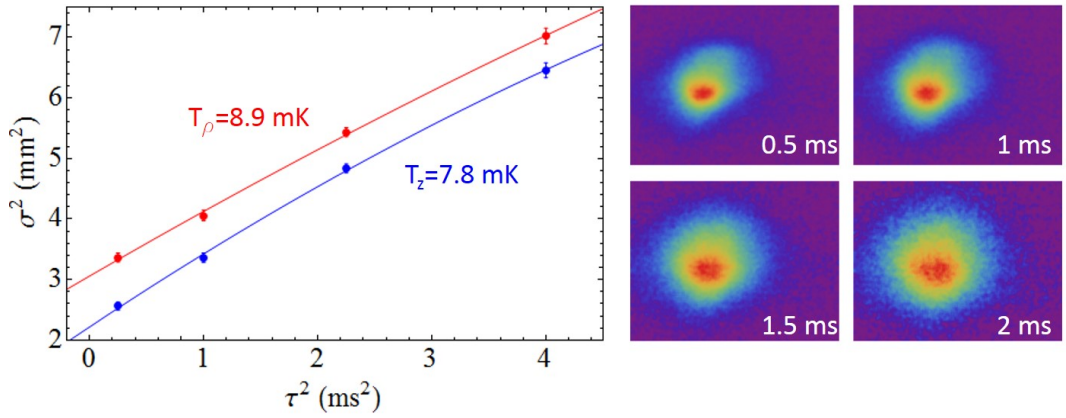

Figure 8.9: Temperature measurement of the MOT. Left: Square of the axial (blue) and radial (red) widths σ of the molecular cloud vs square of the free expansion time τ. The fits give $T_\rho = 8.9 \pm 0.9$ mK and $T_z = 7.8 \pm 1.0$ mK. Right: Images of the cloud after different expansion times, with 1 ms exposure time.

forces are small enough to be neglected.

Standard theory predicts that a thermal cloud with a Gaussian density distribution of rms radius σ_0 and temperature T should expand as $\sigma^2(\tau) = \sigma_0^2 + k_B T \tau^2/m$. The usual method to find the temperature is therefore to plot the square of the width σ against the square of the expansion time τ, and then fit a linear function to it. However, we found that at our temperatures of around 10 mK, the data is better described by a quadratic fit of the form $\sigma^2(\tau) = \sigma_0^2 + k_B T \tau^2/m + a_2 \tau^4$. The reason is that the MOT beams have a size comparable to the width of the expanding cloud, and molecules at the edge of the MOT beams will show reduced fluorescence due to a lower intensity. The quadratic fits are shown in figure 8.9 for the radial (red) and axial (blue) dimension. We find a radial temperature of $T_\rho = 8.9 \pm 0.9$ mK and an axial temperature $T_z = 7.8 \pm 1.0$ mK. It is common to present the total temperature as $T = T_\rho^{2/3} T_z^{1/3}$, giving $T = 8.5 \pm 1.0$ mK. The images next to the graph show the cloud after different expansion times. Each image is the average of 50 repeated shots of the experiment.

8.3.6 Trap frequency and damping constant

We measure the radial and axial trap frequencies of our MOT by temporarily displacing the molecular cloud in the corresponding direction and observing the damped oscillation due to confining and friction forces. The equations of motion of the centre of mass in direction x (e.g. $x = \rho$ or $x = z$ for radial/axial motion) are described in the harmonic oscillator approximation as

$$\ddot{x} + \beta \dot{x} + \omega^2 x = 0 \,, \tag{8.4}$$

where ω is the trap frequency and β is the damping constant. From the trap frequency we can calculate the spring constant $\kappa = m\omega^2$. Since the axial magnetic field gradient is two times bigger than the radial gradient, we expect $\kappa_z = 2\kappa_\rho$ and $\omega_z = \sqrt{2}\omega_\rho$. The damping constant should be equal, $\beta_\rho = \beta_z$, as it does not depend on the magnetic field gradient. The solution to equation 8.4 is

$$x(t) = a \exp^{-\frac{\beta}{2}t} \cos\left(\omega_{\mathrm{obs}} t - \phi\right) , \tag{8.5}$$

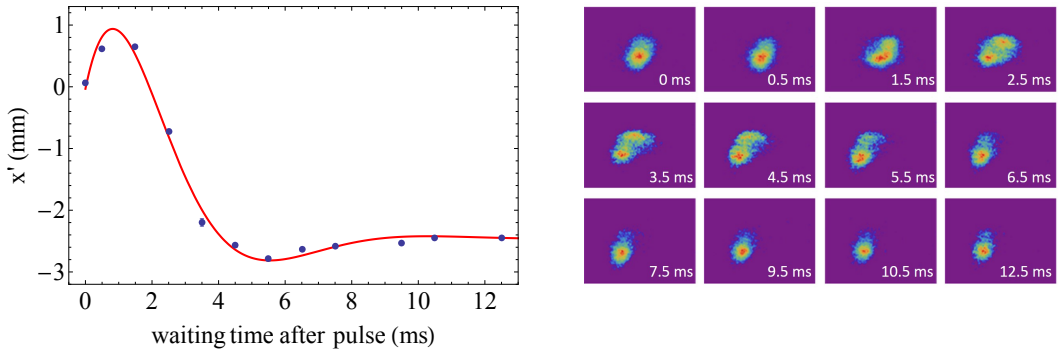

Figure 8.10: Left: Radial oscillation of the molecular cloud in the trap after a push with the slowing laser. The error bars are determined from Gaussian fits to the fluorescence images, and where they are not visible, they are smaller than the data points. The fit gives $\beta = 956 \pm 120$ s^{-1} and $\omega_\rho = 2\pi \times (130 \pm 7)$ Hz. Right: Images of the cloud after different waiting times.

with the experimentally observed oscillation frequency $\omega_{\text{obs}} = \sqrt{\omega^2 - \frac{\beta^2}{4}}$.

Radial oscillation

The radial trap frequency and damping constant are measured by loading a MOT (with $P_{\mathcal{L}_{00}} = 80$ mW per beam) and then pushing the molecular cloud out of its equilibrium position by pulsing on the slowing laser $\mathcal{L}^s_{00}$ (running on the B-X transition). The length of the pulse is 600 μs and the power is $P_{\mathcal{L}^s_{00}} = 100$ mW with the slowing beam diameter of $d_{1/e^2} = 18$ mm. After a waiting time t_{wait} the molecular cloud is imaged with an exposure time of $t_{\text{exp}} = 1$ ms and the centre of the cloud is determined by a Gaussian fit. As we can see in the fluorescence images in figure 8.10 on the right, the cloud can split into different parts, which makes this measurement difficult and the outcome only preliminary. The resulting radial oscillation of the cloud is shown in figure 8.10 on the left. Each data point is the average of 50 images. The fit according to equation 8.5 (red line in the figure) gives $\beta = (9.6 \pm 1.2) \times 10^2$ s^{-1} and $\omega_\rho = 2\pi \times (130 \pm 7)$ Hz.

Axial trap frequency

Since in our setup there is no simple way to push the molecules in the axial direction with a laser, we use the magnetic field of the MOT coils instead. The MOT is loaded

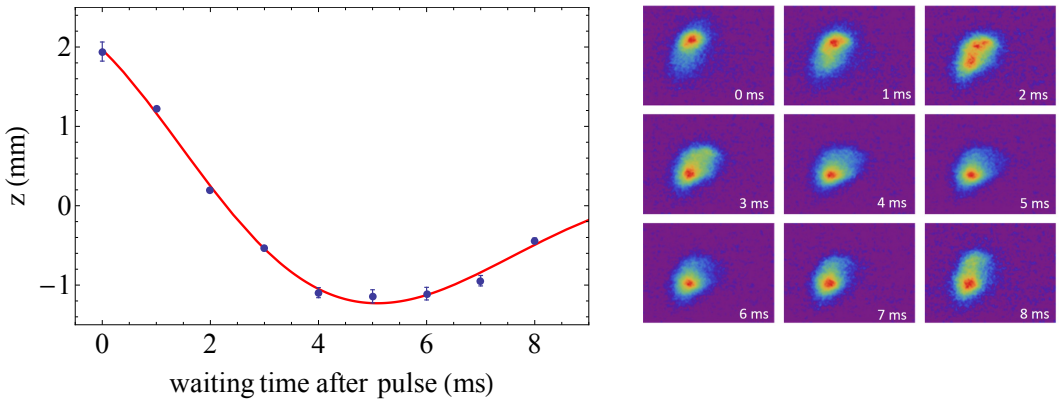

Figure 8.11: Left: Axial oscillation of the cloud after a displacement via a magnetic pulse. The fit (red line) gives $\beta = 315 \pm 120$ s^{-1} and $\omega_z = 2\pi \times (84 \pm 12)$ Hz. The error bars are determined from Gaussian fits to the fluorescence images and are sometimes smaller than the data point. Right: Images of the cloud after different waiting times.

and the current running through the top coil of the MOT is pulsed to a higher value for a duration of 2 ms. This displaces the zero of the magnetic field on the z axis, which results in an acceleration and subsequent oscillation after the current is returned to its starting value. The axial position of the cloud after a waiting time t_{wait} is shown in figure 8.11. Again, each data point is the average of 50 images. The fit according to equation 8.5 (red line in the figure) gives $\beta = 315 \pm 120$ s^{-1} and $\omega_z = 2\pi \times (84 \pm 12)$ Hz.

We note that this measurement is preliminary and should be repeated, ideally with a short laser pulse pushing the cloud. It is suspicious that the radial and axial damping coefficients differ by a factor of three (they should be equal) and that the axial oscillation frequency is smaller than the radial one (should be larger by a factor $\sqrt{2}$). One reason could be that the magnetic field does not switch instantaneously with the current pulse, but instead changes more slowly or even overshoots the intended values (possibly due to eddy currents). We have observed such behaviour before, on the time scale of a millisecond.

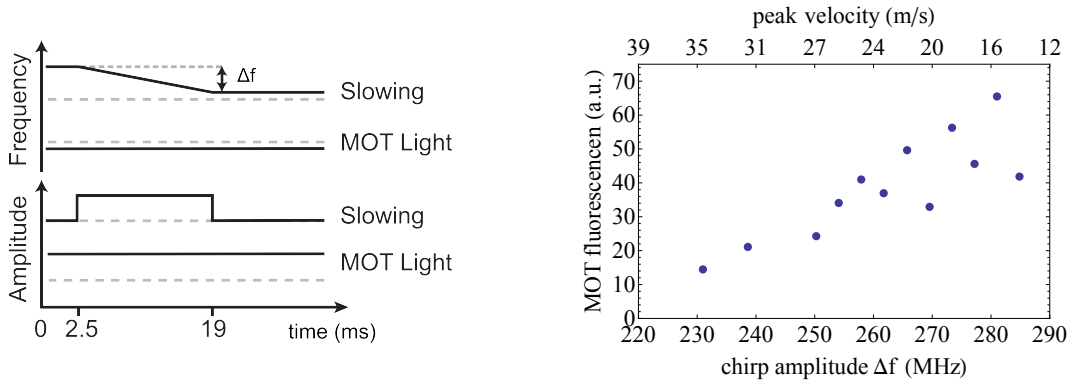

Figure 8.12: Left: Frequency (top) and amplitude (bottom) of the slowing and MOT lasers over time in the experiment. Right: Fluorescence of the MOT (proportional to number of captured molecules) at different chirp amplitudes (bottom horizontal scale). The top scale of the horizontal axis shows the corresponding peak velocity to which the molecular pulse is slowed.

8.3.7 Capture velocity

The exceptional control over the velocity of our molecular beam via chirp slowing should allow a measurement of the capture velocity. We simply vary the chirp amplitude Δf of the main slowing laser (starting from the same frequency and chirping for the same duration) and record the number of trapped molecules in the MOT. Figure 8.12 shows the frequency and amplitude of the MOT light and slowing light for this experiment. The MOT light is left at a constant amplitude and frequency. The slowing light is on between $t = 2.5$ ms and $t = 19$ ms. In this period it is chirped from an initial frequency f_0 to a final frequency $f_0 - \Delta f$. By changing the value of Δf we vary the final velocity distribution. The peak velocity of the slowed molecular pulse (with a width of $\sigma \approx 5$ m/s) is calibrated by Doppler sensitive measurements and shown in figure 8.12 on the top horizontal scale. The data suggests that trapping is possible over a range of velocities, but works best when the molecules are slowed to below 15 m/s. However, this measurement is preliminary and should be repeated.

8.4 Summary

In this chapter we have presented the first demonstration of a MOT of CaF. At full laser power the trap has a radial trap frequency of $\omega_\rho = 2\pi \times (130 \pm 7)$ Hz and a radial damping constant of $\beta = (9.6 \pm 1.2) \times 10^2$ s^{-1}. The highest number of trapped molecules observed is $(7.6 \pm 0.5) \times 10^3$, and the temperature of the molecules is 8.5 ± 1.0 mK. The lifetime of the trap is around 100 ms and depends strongly on the power of the cooling laser. The capture velocity is about 15 m/s at full laser power. All these results are preliminary, but nevertheless they present a first characterisation of our MOT of CaF.

Chapter 9

Outlook

This thesis reports on the successful deceleration and magneto-optical trapping of CaF molecules, which is the second demonstration of a molecular MOT, following first results with SrF molecules in Yale [61]. About 1×10^4 CaF molecules were trapped for around 100 ms at temperatures of about 10 mK. With peak densities around $n = 10^5$ cm^{-3} this corresponds to a phase-space density of $\rho \approx 1 \times 10^{-15}$. While this result marks the end of my PhD research, it is just the beginning of many experiments to come, some of which have been started or already realised by my colleagues during the writing phase of this report. The setup has turned out to be very reliable, reproducing trapped molecules on a daily basis and allowing us to investigate further cooling and trapping methods. Without going too much into details, I will summarise some of those results, and present future research directions. More details can be found in our recent papers [37, 136].

9.1 Transverse cooling of the beam

The number of molecules in the trap depends critically on how many arrive in the capture volume ($\sim$1 cm^3) with velocities below the capture velocity ($v_c \approx 15$ m/s). Apart from the Zeeman-Sisyphus decelerator presented in chapter 6.3, transverse cooling of the beam near the source is currently investigated. We expect about 2-5 times more molecules in the capture region, which would otherwise miss it due to high transverse velocities. Transverse laser cooling of a molecular beam has been previously demonstrated in [54], where they observed both Doppler and sub-Doppler

forces depending on the strength of the applied B-field.

9.2 Sub-Doppler cooling

Doppler cooling is limited to the Doppler temperature $T_D = \hbar\Gamma/2k_B$, about 200μK for CaF on the A-X transition, due to diffusive heating from random spontaneous emission of photons. One way to cool below this limit is polarisation gradient cooling in an optical molasses [137]. This turns out to be simple: In the $\sigma^+\sigma^-$-configuration, where the polarisations are identical as in the standard MOT setup[1], all we need to do is to turn off the magnetic field of the MOT coils (and potentially cancel out fringe fields) and switch the cooling laser to a suitable detuning. While type-I MOTs (see section 8.1) require a red detuned molasses for cooling, type-II MOTs like ours need a blue detuned molasses [138]. A red detuned molasses instead actually heats our molecules, and this seems to be the reason why we don't reach temperatures closer to T_D in our red detuned MOT: Doppler cooling is in competition with sub-Doppler heating, leading to an equilibrium velocity corresponding to a temperature above T_D. This equilibrium velocity decreases with decreasing intensity of the cooling beams. Sub-Doppler cooling can therefore be done in a two-step procedure: First the molecules are trapped in a red detuned MOT and the cooling laser power is ramped down. Secondly, the B-field is set to zero and the cooling laser is shifted to the blue, at a higher power, to do polarisation gradient cooling. Using this protocol we were able to cool CaF molecules to a final temperature of 52 μK, at a phase space density of $\rho \approx 3 \times 10^{-12}$ [37]. This should be sufficiently cold and dense to allow further applications, as explained in the following sections.

9.3 Loading conservative traps

Loading CaF molecules into conservative traps would be a great step towards evaporative cooling. There are different trap types available, which could be loaded from our molecular MOT at sub-Doppler temperatures by simply overlapping them in space.

[1] another possible choice of polarisations of two counter-propagating beams is linear polarisations perpendicular to each other ($lin\perp lin$)

9.3.1 Dipole traps

Dipole traps use the ac Stark shift of a molecule in a far detuned light field [139]. In the case of ground state molecules, a red detuned focussed laser forms an attractive optical dipole potential which is proportional to the ratio of intensity I_j to detuning Δ_j of each transition to the ground state levels. The total dipole potential is given by

$$U_{\mathrm{dip}} \approx \sum_j \frac{3\pi c^2 \Gamma}{2\omega_0^3} \frac{I_j}{\Delta_j} \,. \tag{9.1}$$

For large detunings, the system can be approximated by a two-level system with detuning Δ driven at an intensity I. Heating by the trap light via spontaneous emissions is proportional to $I/|\Delta|^2$, hence a large detuning (typically several THz) is advantageous. This means we need high laser powers and strong focussing of the laser beam to achieve trap depths in the mK regime. A 1 mK deep trap for CaF at $\Delta = 10^6\Gamma$, with $\Gamma = 2\pi \times 8$ MHz, requires an intensity of $I \approx 10^5$ W/cm^2, for example 20 mW focussed to a spot of 5μm diameter. This is easily feasible, and we are currently working on setting up such a trap and loading it from our MOT. The number density of our MOT is small compared to atomic MOTs, but sufficient for first experiments, as it is comparable to the density of the first ever dipole trap loaded from an atomic MOT by Chu *et.al.*[47]. By loading multiple dipole traps, the long-range interactions between CaF molecules could be investigated, and eventually a 2-dimensional array of interacting molecules could simulate quantum systems.

9.3.2 Magnetic traps

Another conservative trap is the static magnetic trap. It uses the Zeeman shift to create a trap potential for molecules with magnetic dipole moments. Only weak-field seeking states can be trapped this way, since there can be no static local field maximum in free space[2]. As discussed in section 6.3, the Zeeman shift of the ground state of CaF is about $h\times$14 GHz/T, corresponding to a trap depth of $k_B \times 0.067$ mK/G. The necessary 15 G magnet field for a trap depth of 1 mK can be easily supplied by

[2]This is the result of Earnshaw's theorem [140].

the MOT coils in our setup. The main challenge is to reduce any current noise in the coils, which would lead to heating. Since the ground state of every molecule is strong-field seeking [141], magnetic traps are subject to losses via inelastic scattering, where one collision partner decays into the ground state and escapes the trap. We are currently investigating magnetic trapping and have loaded traps from our MOT with lifetimes above one second.

9.3.3 Microwave traps

Microwave traps can trap molecules in their absolute ground state, which avoids losses via inelastic collisions. They use the ac Stark shift, similar to optical dipole traps, but on microwave transitions, typically between rotational states [142]. The microwaves are fed into a Fabry-Perot cavity of high quality factor and confine the molecules in the antinodes of the electric field. Microwave traps can be very deep (> 1K) and can have large volumes ($> 1\text{cm}^3$). If the background pressure in the chamber is low enough, molecules can be trapped for several seconds, allowing sympathetic cooling with ultracold atoms [6]. Setting up the microwave poses some geometrical challenges of fitting the resonator in the MOT chamber, but should it in general possible to load a microwave trap from the MOT presented in this work.

9.4 Ultracold collisions with co-trapped rubidium atoms

The number densities in our MOT should allow us to study the collisions between ultracold Rb atoms and CaF molecules. One approach could be to create MOTs of both species in the same chamber and overlap them in a magnetic or microwave trap. Most likely, the highest Rb densities will be reached by first loading a 2D MOT in an extension to the current MOT chamber, and then pushing the atomic cloud towards the MOT center. This also has the advantage of placing the Rb dispenser far away from the molecule MOT centre, possibly separated by a differential pumping stage. Once both Rb atoms and CaF molecules have been loaded into conservative traps, we can investigate the collisional properties and hopefully perform sympathetic cooling to temperatures of a few μK or even below [6]. We are currently working on a design for a MOT chamber for both Rb and CaF and there are no major obstacles

to realising collisional studies at ultracold temperatures in the near future.

9.5 High precision measurements

The work presented in this thesis has increased our understanding of how to laser cool molecules, from the molecular source to the slowing step and the final trap. Our group is working on transferring this knowledge to laser cool YbF molecules, which we already use to measure the electric dipole moment (EDM) of the electron. With the recent first results of transverse cooling of a beam of YbF [143], there should be a path towards a molecular fountain of YbF molecules [10], which would increase the precision of the EDM experiment by several orders of magnitude.

9.6 Outlook of the experiments conducted in Vienna

The buffer gas experiment set up during my secondment, which investigates slow and cold beams with molecules of higher mass than any buffer gas source before, is currently being continued by a PhD student and should hopefully produce bright and slow beams soon. Besides going to different and heavier molecules, a lot of improvements have to be made before the source can be integrated into the KDTL interferometer (or other experiments).

First, the brightness of the beam should be optimised. The velocity selector will be installed and it will be investigated which set of parameters gives a slow yet bright beam. It should be tried to reach the effusive regime, where the forward velocity depends on the mass of the molecule, not of the buffer gas atoms. This is likely to need a more complicated geometry of the buffer gas cell, such as a double stage cell [144]. The potential gain in slowness is enormous, a fully effusive beam at 20 K would give velocities of 17 m/s for gramicidin and 4 m/s for PerCP, at 5 K (using Helium) these numbers would decrease by another factor of 2. Since the minimum de-Broglie wavelength resolvable in the KDTL interferometer is around $\lambda_{DB} \approx 0.5$ pm [96], the maximum allowed velocity for PerCP (32k amu) lies at roughly 30 m/s. A only partly effusive beam should therefore be sufficient. Even for molecules of $m = 10^6$ amu, the allowed velocity lies at 0.8 m/s, which is above the theoretical

effusive speed of 0.4 m/s at 5 K. Unfortunately at these velocities gravity actually starts to be problematic, pulling the beam downwards, so that at this point it might be easier to rebuild the setup for higher resolution.
A very interesting idea to increase the brightness is the use of aerodynamic lenses [145], which consist of a number of apertures along the beam with well defined diameters and distances. They produce a focussing effect, which works especially well for a large mass ratio between buffer gas and molecule. The future will show to which new mass records the current interferometer setup can be pushed, and whether we can confirm or rule out some theories about the transition between the classical and the quantum world.

9.7 Final remarks

The results presented in this thesis show that laser cooling and trapping of certain molecules is feasible with only slightly more complex setups than typical cold atom experiments. While number densities are still orders of magnitudes smaller than for atoms, sub-Doppler temperatures can be reached and very exciting experiments are on the horizon.

Appendices

Appendix A

Calibration of photo-multiplier tubes

Photo-multiplier tubes (PMTs) detect photons via the photoelectric effect. Incident light produces primary electrons in a photo cathode, which by applying high voltage are accelerated towards a dynode, where their impact can produce a number of secondary electrons. These are accelerated again etc., until the electron cascade is detected at the last dynode. While PMTs can count individual photons directly with high frequency, it is convenient to run them in *voltage mode*, which just outputs a voltage proportional to the total photon rate. Translating these voltages into photon numbers requires a calibration. We calibrate the PMTs by counting the number of voltage spikes above a certain level (using a discriminator) per unit time at different intensities of incident light. This number is then plotted versus the voltage measured in voltage mode at the same light intensities and a linear function is fitted to it. It is important to choose the discriminator level correctly, to detect most of the photon events, but not falsely detect spikes from random noise. Using this method, we find a slope of $(1.90 \pm 0.05) \times 10^7$ photons/V.

In order to find the number of photons emitted from molecules in the beam, we also need to know the detection efficiency $\eta = \eta_{\mathrm{qe}}\eta_{\mathrm{geo}}\eta_t$. The quantum efficiency of our PMTs[1] is $\eta_{\mathrm{qe}} = 0.09$, and we assume a transmission $\eta_t = 0.9 \pm 0.03$ of the collection optics. The solid angle of the photon collection is different at the three positions

[1] Hamamatsu R5929

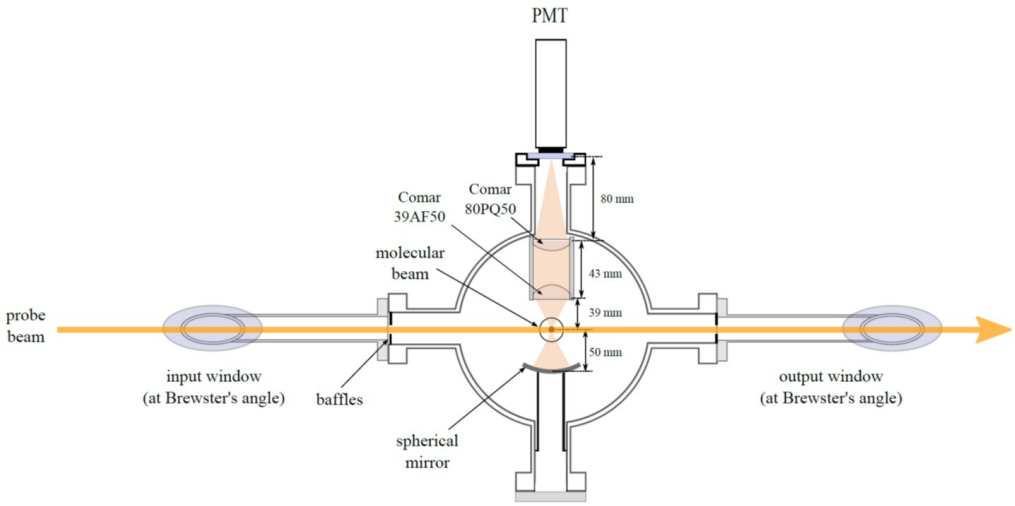

Figure A.1: Setup for detecting the molecular beam at $x = 53$ cm and $x = 130$ cm (vertical cut). The light is collected with a spherical mirror ($r = 50$ mm), placed 50 mm from the beam axis, and a lens ($d = 50$ mm), placed 39 mm from the beam axis. Taken from [66].

along our chamber. At $x = 2.5$ cm from the source, the first PMT is placed on top of the source chamber at a distance of 26 cm from the beam axis. With a diameter of $d = 28$ mm, this results in the geometric efficiency of $\eta_{\text{geo}} = 7.2 \times 10^{-4}$, and a total detection efficiency of $\eta = (5.8 \pm 0.3) \times 10^{-5}$. The PMTs at 53 cm and 130 cm have an identical setup for increased photon collection, consisting of mirror and multiple lenses (see figure A.1). With this setup, we determine the solid angle efficiency to $\eta_{\text{geo}} = 0.125$ and the total detection efficiency to $\eta = (1.01 \pm 0.05) \times 10^{-2}$. The two lenses in the setup lead to a magnification of factor 2. Just before the PMT there is a mask with a rectangular slit of the size 6×10 mm, with the longer side oriented along the probe beam. This means, we detect fluorescence in the chamber in a volume of $5 \times 3 \times 3.5$ mm, where 3.5 mm is the width of the probe beam and the other two values correspond to the demagnified image of the mask. At 53 cm from the source, this corresponds to a solid angle of 6.2×10^{-5} sr.

The last factor in the estimation of the molecule number in the beam is the number of photons emitted per molecule. When detecting with sidebands, but without repump laser present, the molecules can on average scatter a maximum of

30 photons before decaying into a higher lying vibrational state. We calibrate the detection by finding the probe laser power such that the number of photons emitted per molecule is about $p = 1$. In order to determine this power, we first detect a single hyperfine state with the probe laser on resonance but without sidebands. When saturating this transition, all molecules in this specific level will scatter a photon, but most likely no second photon because they quickly decay into a dark state. If we assume that the four hyperfine states of the X state are equally populated, this means 1/4 of all molecules have scattered about one photon each. We now add the sidebands and find the power at which the signal on resonance is four times as big as the saturated signal without sidebands (within a few percent). This should correspond to on average one photon emission per molecule. For the PMT at 53 cm we find that this is the case for $P = 0.5$ mW.

Appendix B

Charcoal shield preparation

The use of cryogenically cooled charcoal as helium adsorption pump is a well studied method in fusion reactor research [94]. The best type of charcoal turns out to be coconut shell charcoal, which is also what we use (mesh size PHO 18×35). The charcoal is glued to a copper shield using a two-component epoxy (Stycast 2850 FT Black Epoxy with catalyst 24LV). The steps are as follows:

1. Use sand paper to roughen up the copper surface.
2. Clean the copper for vacuum as described in chapter 7.2.
3. Apply the prepared epoxy as thin as possible onto the surfaces using a clean brush. A thick layer would cover the charcoal's pores or reduce the thermal connection to the copper.
4. Sprinkle the charcoal onto the epoxy layer, ideally covering it in a single layer.
5. Let the glue dry and bake it according to the epoxy's manual to stop outgassing.

We have found that the full pumping speed of the charcoal will be reached at temperatures below 8 K. During the experiment the shields can fill up with He, which decreases their pumping efficiency. In this case it is sufficient to shortly heat the shields to about $T = 20$ K, so that the He is released and can be pumped by the turbo pumps.

Appendix C

Modeling the optical pumping process

Here we model the population redistribution in the optical pumping process used for the Zeeman-Sisyphus decelerator (chapter 6.3). The optical pumping takes place between 12 magnetic sublevels of the $X^2\Sigma^+(N = 1)$ state, which are pumped via 4 magnetic sublevels of the $A^2\Pi_{1/2}(J = 1/2)$ state. The 12 ground state levels are separated into 6 strong field seeking states (sfs) and 6 weak field seeking states (wfs), and the two groups are energetically separated in a magnetic field. The optical pumping happens either from sfs to wfs states or from wfs to sfs states, depending on the detuning of the pump laser. Figure C.1 shows the transition intensities and branching ratios at $B = 1$ T, adapted from [132]. The columns correspond to the 12 ground state levels and are marked in blue for sfs states and in red for wfs states. The 4 rows correspond to the 4 excited level states.

The transition intensities (figure C.1, top) govern how the population changes in an excitation from the ground to the excited state. For example, looking at the first column of the transition intensity table, we see that the $(F, m_F) = (1^-, 1)$ state will with certainty be excited to the $(F', m_{F'}) = (1, 0)$ level of the A state. The entries in a column are not normalised because they also determine the relative strengths of transitions from different sublevels.

After excitation into the A state follows spontaneous decay, governed by the branching ratio matrix (figure C.1, bottom). For example, looking at the second row, we

Table 1. Transition intensities used in the simulations, calculated in a 1 T magnetic field with linearly polarized light polarized 90° with respect to the strong-field direction. Values less than 1×10^{-4} are shown as zero.

	$(1^-,1)$	$(1^-,0)$	$(1^-,-1)$	$(0,0)$	$(1^+,-1)$	$(1^+,0)$	$(1^+,1)$	$(2,-2)$	$(2,-1)$	$(2,0)$	$(2,1)$	$(2,2)$
$(1,-1)^*$	0	0.0003	0	0.0833	0	0.1656	0	0.0833	0	0.0008	0	0
$(1,0)^*$	0.0835	0	0.0830	0	0.0003	0	0.0007	0	0	0	0.1657	0
$(1,1)^*$	0	0.1662	0	0.0007	0	0.0004	0	0	0	0.0827	0	0.0833
$(0,0)^*$	0	0	0.0007	0	0.1662	0	0.0829	0	0.0831	0	0.0004	0

Table 2. Branching ratios used in the simulation, calculated in a 1 T magnetic field. Values less than 1×10^{-3} are shown as zero.

	$(1^-,1)$	$(1^-,0)$	$(1^-,-1)$	$(0,0)$	$(1^+,-1)$	$(1^+,0)$	$(1^+,1)$	$(2,-2)$	$(2,-1)$	$(2,0)$	$(2,1)$	$(2,2)$
$(1,-1)^*$	0	0.001	0	0.167	0	0.331	0	0.167	0.333	0.002	0	0
$(1,0)^*$	0.167	0	0.166	0	0.001	0.002	0.001	0	0	0.332	0.331	0
$(1,1)^*$	0.333	0.332	0	0.001	0	0.001	0	0	0	0.165	0	0.167
$(0,0)^*$	0	0.001	0.001	0.332	0.332	0	0.166	0	0.166	0	0.001	0

Figure C.1: Transition intensities (top) and branching ratios (bottom) between the 12 ground states (columns) and 4 excited states (rows) on the A-X transition. Sfs states are marked in blue, wfs states in red. Adapted from [132].

see that the $(F', m_{F'}) = (1,0)^*$ state decays with a probability of 33% into the $(F, m_F) = (2,0)$ and $(F, m_F) = (2,1)$ states, while with a probability of 17% the population ends up in the $(1^-,1)$ or $(1^-,-1)$ states. The probabilities summed up over one row add up to 1.

We now have all the information needed to calculate the redistribution from each ground state sublevel into the other sublevels after successive steps of excitation and spontaneous decay. Let's for example consider the pumping process from sfs to wfs states, starting from a population of 1 in the sfs state $(F, m_F) = (0,0)$, described by the vector

$$\vec{v}_{00} = (0,0,0,1,0,0,0,0,0,0,0,0)^T\,, \tag{C.1}$$

where the entries of the vector describe the populations of the states, labelled in the same order as the columns in the transition and branching ratio tables in figure C.1. The model now loops through the following four calculation steps, until the population has reached a steady state:

1. sorting: remove all entries of the population vector $\vec{v}_{00}$ corresponding to wfs states, since these are not addressed, and add these entries to another vector $\vec{v}_f$ describing the final wfs population. If a fraction of the population has been

transferred into a wfs state, it will remain there and not participate in the current pumping process any more.

2. excitation: multiply the population vector $\vec{v}_{00}$ by the transition intensity matrix M_T, given by the entries of the top table in figure C.1, but with each column normalised to 1. The result of the multiplication is the population of the 4 excited states.

3. spontaneous decay: Multiply the vector $\vec{v}_{00}$ by the branching ratio matrix M_B, given by the transposition of the entries of the bottom table in figure C.1. This gives the new distribution of population among the 12 sublevels.

4. either repeat the loop from step 1 or exit it, if a steady state has been reached. The total population is given by the sum of $\vec{v}_{00}$ (population currently being cycled) and $\vec{v}_f$ (population pumped into wfs states previously).

Typically, the population has settled to a steady state after about 10 loops. The result of applying this algorithm on the vector $\vec{v}_{00}$ is

$$\vec{v}_{00,\text{pumped}} = (0, 0, 0, 0, 0, 0.49, 0, 0, 0.49, 0.01, 0.01, 0.01)^T . \tag{C.2}$$

The population is pumped almost completely into the $(F, m_F) = (1^+, -1)$ and $(2, -2)$ states. We can summarise the total population redistribution from one F state to another by following the described algorithm for each of its m_F sublevels. For example, an initial population of 1 in the $F = 1^-$ state, assuming equal distribution between its $m_F = (-1, 0, 1)$ sublevels, would correspond to the starting vector

$$\vec{v}_{F=1^-} = (\frac{1}{3}, \frac{1}{3}, \frac{1}{3}, 0, 0, 0, 0, 0, 0, 0, 0, 0)^T . \tag{C.3}$$

Applying the algorithm for 10 loops, we end up with a population of

$$\vec{v}_{F=1^-,\text{pumped}} = (0, 0, 0, 0, 0, 0.01, 0, 0, 0, 0.49, 0.33, 0.17)^T . \tag{C.4}$$

We find that no population remained in the three $F = 1^-$ sublevels (first three entries) and none was pumped into $F = 0$ (fourth entry), while only 1% found its

way into $F = 1^+$ (entries 5 to 7), and with 99% most was transferred into $F = 2$ (entries 8 to 12). This result corresponds to the first column of the matrix $\hat{M}_s$ in equation 6.4. Repeating the algorithm for all other F states produces the rest of the matrix.

For pumping from wfs to sfs states, the algorithm is almost identical, except that in step 1 now the sfs states will be removed from the population vector, since they will not participate in the pumping any more.

Losses into other rotational states, due to the Q(1) transition coming into resonance, can be introduced by simply multiplying the branching ratio matrix in step 4 by a constant factor r_Q, which describes the probability of decaying back into the rotational state $N = 1$ which is addressed by the lasers (in our case $r_Q = 0.5$). This means that of those molecules which are addressed by the pumping laser and transferred to the excited state, we lose 50% into the $N = 3$ state in the first pumping step. About half of the remaining molecules are successfully pumped (25%) and the other half (25%) decay back into the manifold of states (wfs or sfs) where they started in. In the second pumping step we lose half of those 25% again etc., giving a total loss of $0.5+0.5^3+0.5^5... = 2/3$. This means that only a fraction of $r_{Q,\text{eff}} = 1-2/3 = 1/3$ of the population ends up getting optically pumped. This factor can be included into the optical pumping matrix in equation 6.5 by multiplying it with the off-diagonal elements, which represent the population that got optically pumped from one hyperfine state to another.

Appendix D

Converting CCD camera counts into photon numbers

Each count on the ORCA R2 camera corresponds to a number N_{ph} of photons arriving on the CCD chip. This number is important, since it allows to calculate the total number of molecules in the MOT given that the scattering rate is known (see chapter 8.3.4). Here we compare the information provided by the camera supplier Hamamatsu with our own calibration measurement and find that both agree very well and the calibration is well understood.
According to the camera manual, the total number of photons $N_{\mathrm{ph,tot}}$ corresponding to X counts are calculated via the formula

$$N_{\mathrm{ph,tot}} = \frac{X - X_0}{G} \cdot \underbrace{\frac{\mathrm{FWC}}{X_{\mathrm{max}}} \cdot \frac{1}{\eta_{qe}}}_{N_{\mathrm{ph}}} \tag{D.1}$$

where $X_0 = 100$ is a count offset that is always present, η_{qe} is the quantum efficiency, G is the gain factor (between 1 and 10), FWC is the full well capacity and X_{max} is the maximum number of counts at saturation. The full well capacity describes the maximum number of electrons that can be collected in a pixel and depends on the chosen light mode: In low light mode it is FWC=18000 and in high light mode it is FWC=30000. The maximum number of counts depends on the chosen bit value (BitPerChannel), in 12 bit mode it is $X_{\mathrm{max}} = 2^{12} - 1 = 4095$ and in 16 bit mode it is $X_{\mathrm{max}} = 2^{16} - 1 = 65535$. Using 12 bit, in low light mode, with $G = 1$ and $\eta_{qe} = 0.7$

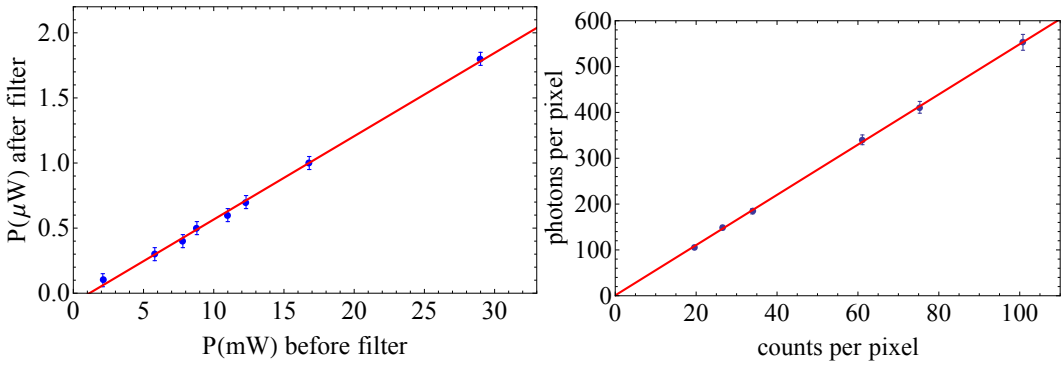

Figure D.1: Left: Calibration of the laser power before and after a neutral density filter. The error bars show estimated measurement errors. The fit gives an attenuation of 0.064 ± 0.002. Right: Counts in the camera software vs number of incoming photons (calculated from the measured power) in 0.5 ms exposure time. The linear fit gives $N_{\mathrm{ph}} = 5.5 \pm 0.2$ photons on the chip per count in the software (error from fit). The error bars of increasing width are due to the linear dependence of the photon number on the measured power, and the calibration error used in this measurement.

then predicts $N_{\mathrm{ph}} \approx 6.3$ photons per count, which generate $6.3 \cdot 0.7 = 4.4$ electrons on the chip.

We perform a calibration measurement to confirm this predicted value. For this, a laser beam at $\lambda = 606$ nm is sent onto the camera chip, which is otherwise shielded from any light. We measure the laser power P to determine the photon flux $\dot{N}_{\mathrm{ph,beam}} = P\lambda/(h\,c)$ in the beam. Since the laser power needs to be very low to not saturate the camera, and the power meter doesn't work well at these low powers, we first determine the attenuation of a neutral density filter placed in the beam path (see figure D.1, left). This way the power before the filter can be measured to determine the power after the filter. The calibration gives an attenuation factor of 0.064 ± 0.002. We then record the counts per pixel on the camera for various laser powers with an exposure time of $t = 0.5$ ms. Figure D.1 shows the result plotted against the photon number per pixel arriving on the chip. A linear fit gives $N_{\mathrm{ph}} = 5.5 \pm 0.2$ photons on the chip per count in the software. The predicted value of 6.3 photons per count is not within the calculated error range, which hints at systematic errors not taken into account. Nevertheless the calibrated value is close

enough to accept the value of 6.3 photons specified by the manufacturer.

The number of measured counts also depends on various parameters, which can be chosen in the camera software HCImageLive.

- Gain: Can be chosen as values between 0 and 255, with 0 meaning no gain and 255 corresponding to a factor 10 increase in counts. The offset X_0 is applied after the gain.
- Binning: The pixels on the camera can be hardware-binned to *super pixels* of 2x2, 4x4 or 8x8 pixels. This increases the counts per pixel by 4, 16, 64 respectively, but not the total counts on the chip. The offset X_0 is applied after binning.
- Exposure time: The total count number is of course proportional to the length of exposure (assuming a constant fluorescence rate).
- Light Mode: We always use the low light mode, since it has a higher sensitivity.
- Speed: We always use the high speed mode (Mode 2).
- BitPerChannel/Depth : We use 12 Bit per channel, and 16 Bit depth.

The camera saves pictures as ".tif" files. Here, the counts in each pixel are represented as a decimal numbers between 0 and 1 and need to be multiplied by $2^{16} - 1 = 65520$ to recover the actual number of counts.

Appendix E

Permissions

AMERICAN PHYSICAL SOCIETY LICENSE TERMS AND CONDITIONS

Jun 26, 2017

This Agreement between Imperial College London -- Moritz Hambach ("You") and American Physical Society ("American Physical Society") consists of your license details and the terms and conditions provided by American Physical Society and Copyright Clearance Center.

License Number	4127781107051
License date	Jun 14, 2017
Licensed Content Publisher	American Physical Society
Licensed Content Publication	Reviews of Modern Physics
Licensed Content Title	Colloquium
Licensed Content Author	Klaus Hornberger et al.
Licensed Content Date	Feb 8, 2012
Licensed Content Volume	84
I would like to...	Thesis/Dissertation
Requestor type	Student
Format	Print, Electronic
Portion	chart/graph/table/figure
Number of charts/graphs /tables/figures	2
Portion description	figure 1, figure 2
Rights for	Main product
Duration of use	Life of Current Edition
Creation of copies for the disabled	no
With minor editing privileges	no
For distribution to	Worldwide
In the following language(s)	Original language of publication
With incidental promotional use	no
The lifetime unit quantity of new product	0 to 499
The requesting person/organization is:	Moritz Hambach
Order reference number	
Title of your thesis / dissertation	Development of a magneto-optical trap of CaF molecules
Expected completion date	Jun 2017
Expected size (number of pages)	150
Requestor Location	Imperial College London Centre for Cold Matter The Blackett Laboratory Prince Consort Road London, SW7 2BW United Kingdom Attn: Imperial College London

JOHN WILEY AND SONS LICENSE TERMS AND CONDITIONS

Jun 26, 2017

This Agreement between Imperial College London -- Moritz Hambach ("You") and John Wiley and Sons ("John Wiley and Sons") consists of your license details and the terms and conditions provided by John Wiley and Sons and Copyright Clearance Center.

License Number	4130110793908
License date	Jun 15, 2017
Licensed Content Publisher	John Wiley and Sons
Licensed Content Publication	Wiley Books
Licensed Content Title	Wiley Encyclopedia of Electrical and Electronics Engineering, 24 Volume Set
Licensed Content Author	John G. Webster (Editor)
Licensed Content Date	Mar 1, 1999
Licensed Content Pages	17616
Type of Use	Dissertation/Thesis
Requestor type	University/Academic
Format	Print and electronic
Portion	Figure/table
Number of figures/tables	1
Original Wiley figure/table number(s)	Figure 7 (in Chapter III-V Compound Semiconductor Optoelectronic Devices)
Will you be translating?	No
Title of your thesis / dissertation	Development of a magneto-optical trap of CaF molecules
Expected completion date	Jun 2017
Expected size (number of pages)	150
Requestor Location	Imperial College London Centre for Cold Matter The Blackett Laboratory Prince Consort Road London, SW7 2BW United Kingdom Attn: Imperial College London
Publisher Tax ID	EU826007151
Billing Type	Invoice
Billing Address	Imperial College London Centre for Cold Matter The Blackett Laboratory Prince Consort Road London, United Kingdom SW7 2BW Attn: Imperial College London
Total	**0.00 GBP**
Terms and Conditions	

TERMS AND CONDITIONS

This copyrighted material is owned by or exclusively licensed to John Wiley & Sons, Inc. or one of its group companies (each a"Wiley Company") or handled on behalf of a society with which a Wiley Company has exclusive publishing rights in relation to a particular work (collectively "WILEY"). By clicking "accept" in connection with completing this licensing transaction, you agree that the following terms and conditions apply to this transaction (along with the billing and payment terms and

Bibliography

[1] DeMille, D. Quantum computation with trapped polar molecules. *Physical Review Letters* **88**, 067901 (2002). arXiv:0109083.

[2] Isenhower, L., Urban, E., Zhang, X. L., Gill, A. T., Henage, T., Johnson, T. A., Walker, T. G. & Saffman, M. Demonstration of a neutral atom controlled-NOT quantum gate. *Physical Review Letters* **104**, 010503 (2010). arXiv:0907.5552.

[3] Schmidt-Kaler, F., Riebe, M. & Gulde, S. Realization of the Cirac Zoller controlled-NOT quantum gate. *Nature* **422**, 408 (2003).

[4] Góral, K., Santos, L. & Lewenstein, M. Quantum phases of dipolar bosons in optical lattices. *Physical Review Letters* **88**, 170406 (2002). arXiv:0112363.

[5] Stuhl, B. K., Hummon, M. T., Yeo, M., Quéméner, G., Bohn, J. L. & Ye, J. Evaporative cooling of the dipolar hydroxyl radical. *Nature* **492**, 396–400 (2012). arXiv:1209.6343.

[6] Lim, J., Frye, M. D., Hutson, J. M. & Tarbutt, M. R. Modeling sympathetic cooling of molecules by ultracold atoms. *Physical Review A - Atomic, Molecular, and Optical Physics* **92**, 053419 (2015). arXiv:1508.03987.

[7] Hudson, E. R., Lewandowski, H. J., Sawyer, B. C. & Ye, J. Cold molecule spectroscopy for constraining the evolution of the fine structure constant. *Physical Review Letters* **96**, 143004 (2006). arXiv:0601054.

[8] Truppe, S., Hendricks, R. J., Tokunaga, S. K., Lewandowski, H. J., Kozlov, M. G., Henkel, C., Hinds, E. a. & Tarbutt, M. R. A search for varying fundamental constants using Hz-level frequency measurements of cold CH molecules. *Nature Communications* **4**, 2600 (2013). arXiv:1308.1496.

[9] Hudson, J. J., Kara, D. M., Smallman, I. J., Sauer, B. E., Tarbutt, M. R. & Hinds, E. a. Improved measurement of the shape of the electron. *Nature* **473**, 493–496 (2011).

[10] Tarbutt, M. R., Sauer, B. E., Hudson, J. J. & Hinds, E. A. Design for a fountain of YbF molecules to measure the electron's electric dipole moment. *New Journal of Physics* **15**, 053034 (2013). arXiv:1302.2870.

[11] Balakrishnan, N. & Dalgarno, A. Chemistry at ultracold temperatures. *Chemical Physics Letters* **341**, 652–656 (2001).

[12] Carr, L. D., DeMille, D., Krems, R. V. & Ye, J. Cold and ultracold molecules: science, technology and applications. *New Journal of Physics* **11**, 055049 (2009). arXiv:0904.3175.

[13] Fioretti, A., Comparat, D., Crubellier, A., Dulieu, O., Masnou-Seeuws, F. & Pillet, P. Formation of Cold Cs_2 Molecules through Photoassociation. *Physical Review Letters* **80**, 4402–4405 (1998).

[14] Nikolov, A. N., Eyler, E. E., Wang, X. T., Li, J., Wang, H., Stwalley, W. C. & Gould, P. L. Observation of Ultracold Ground-State Potassium Molecules. *Physical Review Letters* **82**, 703–706 (1999).

[15] Herbig, J., Kraemer, T., Mark, M., Weber, T., Chin, C., Nägerl, H.-C. & Grimm, R. Preparation of a pure molecular quantum gas. *Science (New York, N.Y.)* **301**, 1510–1513 (2003).

[16] Xu, K., Mukaiyama, T., Abo-Shaeer, J. R., Chin, J. K., Miller, D. E. & Ketterle, W. Formation of quantum-degenerate sodium molecules. *Physical Review Letters* **91**, 210402 (2003). arXiv:0310027.

[17] Vitanov, N., Fleischhauer, M., Shore, B. & Bergmann, K. Coherent manipulation of atoms and molecules by sequential laser pulses. *Adv. At. Mol. Opt. Phys.* **46**, 55–190 (2001).

[18] Ni, K. K., Ospelkaus, S., de Miranda, M. H. G., Pe'er, A., Neyenhuis, B., Zirbel, J. J., Kotochigova, S., Julienne, P. S., Jin, D. S. & Ye, J. A High

Phase-Space-Density Gas of Polar Molecules. *Science* **322**, 231–235 (2008). arXiv:0808.2963.

[19] Takekoshi, T., Reichsöllner, L., Schindewolf, A., Hutson, J. M., Le Sueur, C. R., Dulieu, O., Ferlaino, F., Grimm, R. & Nägerl, H. C. Ultracold dense samples of dipolar RbCs molecules in the rovibrational and hyperfine ground state. *Physical Review Letters* **113**, 205301 (2014). arXiv:1405.6037.

[20] Park, J. W., Will, S. A. & Zwierlein, M. W. Ultracold Dipolar Gas of Fermionic Na23K40 Molecules in Their Absolute Ground State. *Physical Review Letters* **114**, 205302 (2015). arXiv:1505.00473v1.

[21] Guo, M., Zhu, B., Lu, B., Ye, X., Wang, F., Vexiau, R., Bouloufa-Maafa, N., Quéméner, G., Dulieu, O. & Wang, D. Creation of an Ultracold Gas of Ground-State Dipolar Na 23 Rb 87 Molecules. *Physical Review Letters* **116**, 205303 (2016). arXiv:1602.03947.

[22] Rvachov, T. M., Son, H., Sommer, A. T., Ebadi, S., Park, J. J., Zwierlein, M. W., Ketterle, W. & Jamison, A. O. Long-Lived Ultracold Molecules with Electric and Magnetic Dipole Moments **143001**, 143001 (2017). arXiv:1707.03925.

[23] Ni, K. K., Ospelkaus, S., de Miranda, M. H. G., Pe'er, A., Neyenhuis, B., Zirbel, J. J., Kotochigova, S., Julienne, P. S., Jin, D. S. & Ye, J. A High Phase-Space-Density Gas of Polar Molecules. *Science (New York, N.Y.)* **322**, 231–235 (2008). arXiv:0808.2963.

[24] Levy, D. H. Laser Spectroscopy of cold gas-phase molecules. *Ann. Rev. Phys. Chem.* **31**, 197–225 (1980).

[25] Smalley, R. E., Wharton, L. & Levy, D. H. The fluorescence excitation spectrum of rotationally cooled NO_2. *The Journal of Chemical Physics* **63**, 4977 (1975).

[26] Maxwell, S. E., Brahms, N., DeCarvalho, R., Glenn, D. R., Helton, J. S., Nguyen, S. V., Patterson, D., Petricka, J., DeMille, D. & Doyle, J. M. High-

Flux Beam Source for Cold, Slow Atoms or Molecules. *Physical Review Letters* **95**, 173201 (2005). arXiv:0508100.

[27] Zeppenfeld, M., Motsch, M., Pinkse, P. W. H. & Rempe, G. Optoelectrical cooling of polar molecules. *Physical Review A - Atomic, Molecular, and Optical Physics* **80**, 041401 (2009). arXiv:0904.4144.

[28] Prehn, A., Ibrügger, M., Glöckner, R., Rempe, G. & Zeppenfeld, M. Optoelectrical Cooling of Polar Molecules to Submillikelvin Temperatures. *Physical Review Letters* **116**, 063005 (2016). arXiv:1511.09427.

[29] Dunseith, D. P., Truppe, S., Hendricks, R. J., Sauer, B. E., Hinds, E. a. & Tarbutt, M. R. A high quality, efficiently coupled microwave cavity for trapping cold molecules. *Journal of Physics B: Atomic, Molecular and Optical Physics* **48**, 045001 (2014). arXiv:1409.2859.

[30] DeMille, D., Sage, J. M., Sainis, S. & Bergenian, T. Optical production of ultracold polar molecules. *AIP Conference Proceedings* **869**, 284–291 (2006). arXiv:0501008.

[31] Aikawa, K., Akamatsu, D., Hayashi, M., Oasa, K., Kobayashi, J., Naidon, P., Kishimoto, T., Ueda, M. & Inouye, S. Coherent transfer of photoassociated molecules into the rovibrational ground state. *Physical Review Letters* **105**, 1–4 (2010). arXiv:1008.5034.

[32] Haimberger, C., Kleinert, J., Dulieu, O. & Bigelow, N. P. Processes in the formation of ultracold NaCs. *Journal of Physics B: Atomic, Molecular and Optical Physics* **39**, S957–S963 (2006).

[33] Deiglmayr, J., Grochola, A., Repp, M., Mörtlbauer, K., Glück, C., Lange, J., Dulieu, O., Wester, R. & Weidemüller, M. Formation of ultracold polar molecules in the rovibrational ground state. *Physical Review Letters* **101**, 1–4 (2008). arXiv:0807.3272.

[34] Nemitz, N., Baumer, F., Münchow, F., Tassy, S. & Görlitz, A. Production of heteronuclear molecules in an electronically excited state by photoassociation

in a mixture of ultracold Yb and Rb. *Physical Review A - Atomic, Molecular, and Optical Physics* **79**, 21–24 (2009).

[35] Dutta, S., Lorenz, J., Altaf, A., Elliott, D. S. & Chen, Y. P. Photoassociation of ultracold LiRb * molecules: Observation of high efficiency and unitarity-limited rate saturation. *Physical Review A - Atomic, Molecular, and Optical Physics* **89**, 020702 (2014). arXiv:1311.6297.

[36] Steinecker, M. H., McCarron, D. J., Zhu, Y. & DeMille, D. Improved Radio-Frequency Magneto-Optical Trap of SrF Molecules. *ChemPhysChem* 3664–3669 (2016).

[37] Truppe, S., Williams, H. J., Hambach, M., Caldwell, L., Fitch, N. J., Hinds, E. A., Sauer, B. E. & Tarbutt, M. R. Molecules cooled below the Doppler limit (2017). arXiv:1703.00580.

[38] Stuhl, B. K., Hummon, M. T., Yeo, M., Quemener, G., Bohn, J. L. & Ye, J. Evaporative cooling of the dipolar hydroxyl radical. *Nature* **492**, 396–400 (2012). arXiv:1209.6343.

[39] Lett, P. D., Watts, R. N., Westbrook, C. I. & Phillips, W. D. Observation of Atoms Laser Cooled below the Doppler Limit. *Physical Review Letters* **61**, 169–173 (1988).

[40] Frisch, R. Experimenteller Nachweis des Einsteinschen Strahlungsrueckstosses. *Zeitschrift fuer Physik* **86**, 42–48 (1933).

[41] Hänsch, T. W. & Schawlow, A. L. Cooling of gases by laser radiation. *Optics Communications* **13**, 68–69 (1975).

[42] Wineland, D. J., Drullinger, R. E. & Walls, F. L. Radiation-Pressure Cooling of Bound Resonant Absorbers. *Physical Review Letters* **40**, 1639 (1978). arXiv:1011.1669.

[43] Andreev, S., Balykin, V., Lethokhov, V. & Minogin, V. Radiative slowing and reduction of the energy spread of a beam of sodium atoms to 1.5 K in an oppositely directed laser beam. *Zh. Eksp. Theor. Fiz* 34:463 (1981).

[44] Prodan, J. V. & Phillips, W. D. Chirping the light - fantastic? Recent NBS atom cooling experiments. *Prog. Quant. Electr.* **8**, 231–235 (1984).

[45] Phillips, W. D. & Metcalf, H. Laser deceleration of an atomic beam. *Physical Review Letters* **48**, 596–599 (1982).

[46] Chu, S., Hollberg, L., Bjorkholm, J. E., Cable, A. & Ashkin, A. Three-dimensional viscous confinement and cooling of atoms by resonance radiation pressure. *Physical Review Letters* **55** (1985).

[47] Chu, S., Bjorkholm, J. E., Ashkin, A. & Cable, A. Experimental observation of optically trapped atoms. *Physical Review Letters* **57**, 314–317 (1986).

[48] Migdall, A. L., Prodan, J. V. & Phillips, W. D. First Observation of Magnetically Trapped Neutral Atoms. *Physical Review Letters* **54**, 2596–2599 (1985).

[49] Tung, S., Lamporesi, G., Lobser, D., Xia, L. & Cornell, E. A. Observation of the Presuperfluid Regime in a Two-Dimensional Bose Gas. *Physical Review Letters* **59**, 2631–2634 (2010). arXiv:1009.2475.

[50] Anderson, M. H., Ensher, J. R., Matthews, M. R., Wieman, C. E. & Cornell, E. A. Observation of bose-einstein condensation in a dilute atomic vapor. *Science (New York, N.Y.)* **269**, 198–201 (1995).

[51] Di Rosa, M. D. Laser-cooling molecules: Concept, candidates, and supporting hyperfine-resolved measurements of rotational lines in the A-X(0,0) band of CaH. *European Physical Journal D* **31**, 395–402 (2004).

[52] Stuhl, B. K., Sawyer, B. C., Wang, D. & Ye, J. Magneto-optical trap for polar molecules. *Physical Review Letters* **101**, 243002 (2008). arXiv:0808.2171.

[53] Shuman, E. S., Barry, J. F., Glenn, D. R. & Demille, D. Radiative force from optical cycling on a diatomic molecule. *Physical Review Letters* **103**, 223001 (2009). arXiv:0909.2600.

[54] Shuman, E. S., Barry, J. F. & Demille, D. Laser cooling of a diatomic molecule. *Nature* **467**, 820–823 (2010). arXiv:1103.6004.

[55] Barry, J. F., Shuman, E. S., Norrgard, E. B. & Demille, D. Laser radiation pressure slowing of a molecular beam. *Physical Review Letters* **108**, 103002 (2012).

[56] Zhelyazkova, V., Cournol, A., Wall, T. E., Matsushima, A., Hudson, J. J., Hinds, E. a., Tarbutt, M. R. & Sauer, B. E. Laser cooling and slowing of CaF molecules. *Physical Review A - Atomic, Molecular, and Optical Physics* **89**, 053416 (2013). arXiv:1308.0421.

[57] Smallman, I., Wang, F., Steimle, T., Tarbutt, M. & Hinds, E. Radiative branching ratios for excited states of ^{174}YbF: Application to laser cooling. *Journal of Molecular Spectroscopy* **300**, 3–6 (2014). arXiv:1401.4882.

[58] Hendricks, R. J., Holland, D. A., Truppe, S., Sauer, B. E. & Tarbutt, M. R. Vibrational branching ratios and hyperfine structure of ^{11}BH and its suitability for laser cooling. *Frontiers in Physics* **2**, 1–8 (2014). arXiv:1404.6174.

[59] Nasyrov, K., Biancalana, V., Burchianti, A., Calabrese, R., Marinelli, C., Mariotti, E. & Moi, L. Magneto-optical trap operating on a magnetically induced level-mixing effect. *Physical Review A. Atomic, Molecular, and Optical Physics* **64**, 023412 (2001).

[60] Hummon, M. T., Yeo, M., Stuhl, B. K., Collopy, A. L., Xia, Y. & Ye, J. Magneto-optical trapping of diatomic molecules. *Physical Review Letters* **110**, 063004 (2012). arXiv:1209.4069.

[61] Barry, J. F., Mccarron, D. J., Norrgard, E. B., Steinecker, M. H. & Demille, D. Magneto-optical trapping of a diatomic molecule. *Nature* **512**, 286–289 (2014). arXiv:1404.5680.

[62] Mccarron, D. J., Norrgard, E. B., Steinecker, M. H. & Demille, D. Improved magneto-optical trapping of a diatomic molecule. *New Journal of Physics* **17** (2015). arXiv:1404.5680.

[63] Tarbutt, M. R. Magneto-optical trapping forces for atoms and molecules with complex level structures. *New Journal of Physics* **17**, 15007 (2015).

[64] Norrgard, E. B., McCarron, D. J., Steinecker, M. H., Tarbutt, M. R. & DeMille, D. Sub-millikelvin dipolar molecules in a radio-frequency magneto-optical trap. *Physical Review Letters* **116**, 063004 (2016). arXiv:1511.00930.

[65] van der Straten, P. & Metcalf, H. Atoms and Molecules interacting with light. *Cambridge Press* .

[66] Zhelyazkova, V. Laser Cooling of CaF Molecules. *PhD Thesis, Imperial College London* (2014).

[67] Childs, W. J., Goodman, S., Nielsen, U. & Pfeufer, V. Electric-dipole moment of CaF ($X^2\Sigma^+$) by molecular beam, laser-rf, double resonance study of Stark splittings. *The Journal of Chemical Physics* **80(6)**, 2283–2287 (1984).

[68] Pelegrini, M., Vivacqua, C. S., Roberto-Neto, O., Ornellas, F. R. & Machado, F. B. C. Radiative transition probabilities and lifetimes for the band systems $A\Pi$ - $X\Sigma^+$ of the isovalent molecules BeF, MgF and CaF. *Brazilian Journal of Physics* **35**, 950–956 (2005).

[69] Zhuang, X. *et al.* Franck-Condon factors and radiative lifetime of the $A^2\Pi_{1/2} - X^2\Sigma^+$ transition of ytterbium monofluoride, YbF. *Phys. Chem. Chem. Phys. Phys. Chem. Chem. Phys* **13**, 19013–19017 (2011).

[70] Tarallo, M. G., Iwata, G. Z. & Zelevinsky, T. BaH molecular spectroscopy with relevance to laser cooling. *Physical Review A - Atomic, Molecular, and Optical Physics* **93** (2016). arXiv:1512.06316.

[71] Chen, T., Bu, W. & Yan, B. Structure, branching ratios, and a laser-cooling scheme for the ^{138}BaF. *Physical Review A* **94**, 063415 (2016).

[72] Hunter, L. R., Peck, S. K., Greenspon, A. S., Alam, S. S. & DeMille, D. Prospects for laser cooling TlF. *Physical Review A* **85**, 012511 (2012). arXiv:1110.3748.

[73] Wells, N. & Lane, I. C. Electronic states and spin-forbidden cooling transitions of AlH and AlF. *PCCP* **13**, 19018–25 (2011).

[74] Langhoff, S. R., Bauschlicher, C. W. & Taylor, P. R. Theoretical studies of AlF, AlCl, and AlBr. *The Journal of Chemical Physics* **88**, 5715–5725 (1988).

[75] Kirste, M., Wang, X., Meijer, G., Gubbels, K. B., van der Avoird, A., Groenenboom, G. C. & van de Meerakker, S. Y. T. Communication: Magnetic dipole transitions in the OH A 2Σ+ X 2Π system. *The Journal of chemical physics* **137**, 101102 (2012). arXiv:1208.4939.

[76] Tarbutt, M. R. & Steimle, T. C. Modeling magneto-optical trapping of CaF molecules. *Physical Review A* **92**, 053401 (2015).

[77] Bransden, B. & Joachain, C. Physics of Atoms and Molecules. *Prentice Hall* .

[78] Kaledin, L. A., Bloch, J. C., McCarthy, M. C. & Field, R. W. Analysis and Deperturbation of the $A^2\Pi$ and $B^2\Sigma^+$ States of CaF. *Journal of Molecular Spectroscopy* **197**, 289–296 (1999).

[79] Verges, J., Effantin, C., Bernard, A., Topouzkhanian, A., Allouche, A., D'Incan, J. & Barrow, R. The B^2 Delta state of CaF. *J. Phys. B: At. Mol. Opt. Phys* **26**, 279–284 (1993).

[80] Wall, T. E., Kanem, J. F., Hudson, J. J., Sauer, B. E., Cho, D., Boshier, M. G., Hinds, E. A. & Tarbutt, M. R. Lifetime of the A (v'=0) state and Franck-Condon factor of the A-X (0-0) transition of CaF measured by the saturation of laser-induced fluorescence. *Physical Review A - Atomic, Molecular, and Optical Physics* **78**, 062509 (2008). arXiv:0809.1150.

[81] Metcalf, H. J. & van der Straten, P. Laser cooling and trapping of atoms. *Journal of Optical Society of America* **20**, 887–908 (2003).

[82] Truppe, S., Williams, H. J., Fitch, N. J., Hambach, M., Wall, T. E., Hinds, E. A., Sauer, B. E. & Tarbutt, M. R. An intense, cold, velocity-controlled molecular beam by frequency-chirped laser slowing. *New Journal of Physics* **19**, 022001 (2017). arXiv:1605.06055.

[83] Doyle, J. M., Friedrich, B., Kim, J. & Patterson, D. Buffer-gas loading of atoms and molecules into a magnetic trap. *Physical Review A* **52** (1995).

[84] Patterson, D. & Doyle, J. M. Bright, guided molecular beam with hydrodynamic enhancement. *The Journal of Chemical Physics* **126**, 154307 (2007). arXiv:0703025.

[85] Hutzler, N. R., Parsons, M., Gurevich, Y. V., Hess, P. W., Petrik, E., Spaun, B., Vutha, A. C., DeMille, D., Gabrielse, G. & Doyle, J. M. A cryogenic beam of refractory, chemically reactive molecules with expansion cooling 18976–18985 (2011). arXiv:1101.4217.

[86] Hutzler, N. R., Lu, H.-I. & Doyle, J. M. The Buffer Gas Beam: An Intense, Cold, and Slow Source for Atoms and Molecules. *Chemical Reviews* **112**, 4803–4827 (2011). arXiv:1111.2841.

[87] Patterson, D. Buffer Gas Cooled Beams and Cold Molecular Collisions. *Phd Thesis, Harvard University* (2010).

[88] Barry, J. F. Laser cooling and slowing of a diatomic molecule. *PhD thesis, Yale University* (2013).

[89] Wall, T. E. Preparation of cold molecules for high-precision measurements. *Journal of Physics B: Atomic, Molecular and Optical Physics* **49**, 243001 (2016).

[90] Bumby, J. S. Progress towards a source of cold, slow molecules for tests of fundamental physics. *PhD Thesis, Imperial College London* (2016).

[91] Bulleid, N. E., Skoff, S. M., Hendricks, R. J., Sauer, B. E., Hinds, E. a. & Tarbutt, M. R. Characterization of a cryogenic beam source for atoms and molecules. *Physical chemistry chemical physics : PCCP* **15**, 12299–307 (2013). arXiv:1306.0241.

[92] Barry, J. F., Shuman, E. S. & DeMille, D. A bright, slow cryogenic molecular beam source for free radicals. *Physical Chemistry Chemical Physics* **13**, 18936 (2011). arXiv:1101.4229.

[93] Bulleid, N. E. Slow, cold beams of polar molecules for precision measurements. *PhD Thesis, Imperial College London* (2013).

[94] Sedgley, D. W., Tobin, A. G., Batzer, T. H. & Call, W. R. Characterization of charcoals for helium cryopumping in fusion devices. *J. Vac. Sci. Tech. A* **5**, 2572 (1987).

[95] Tarbutt, M. R., Hudson, J. J., Sauer, B. E. & Hinds, E. A. Preparation and manipulation of molecules for fundamental physics tests 22 (2008). arXiv:0803.0967.

[96] Eibenberger, S., Gerlich, S., Arndt, M., Mayor, M. & Tüxen, J. Matter-wave interference with particles selected from a molecular library with masses exceeding 10000 amu. *Physical Chemistry Chemical Physics* **15**, 14696 (2013). arXiv:1310.8343.

[97] Bassi, A., Lochan, K., Satin, S., Singh, T. P. & Ulbricht, H. Models of wave-function collapse, underlying theories, and experimental tests. *Reviews of Modern Physics* **85**, 471–527 (2013). arXiv:1204.4325.

[98] Gerlich, S., Eibenberger, S., Tomandl, M., Nimmrichter, S., Hornberger, K., Fagan, P. J., Tüxen, J., Mayor, M. & Arndt, M. Quantum interference of large organic molecules. *Nature communications* **2**, 263 (2011).

[99] Talbot, H. LXXVI. Facts relating to optical science. No. IV. *Philosophical Magazine Series 3* **9**, 401–407 (1836).

[100] Lau, E. Beugungserscheinungen an Doppelrastern. *Annalen der Physik* **437**, 417–423 (1948).

[101] Hornberger, K., Gerlich, S., Haslinger, P., Nimmrichter, S. & Arndt, M. Colloquium: Quantum interference of clusters and molecules. *Reviews of Modern Physics* **84**, 157–173 (2012). arXiv:1109.5937.

[102] Schwarz, H. The reflection of electrons from standing light waves. *Zeitschrift fuer Physik* **204**, 276–289 (1967).

[103] Even, U. The Even-Lavie valve as a source for high intensity supersonic beam. *EPJ Techniques and Instrumentation* **2**, 17 (2015).

[104] Juffmann, T., Milic, A., Müllneritsch, M., Asenbaum, P., Tsukernik, A., Tüxen, J., Mayor, M., Cheshnovsky, O. & Arndt, M. Real-time single-molecule imaging of quantum interference. *Nature Nanotechnology* **7**, 297–300 (2012).

[105] Eibenberger, S., Cheng, X., Cotter, J. P. & Arndt, M. Absolute Absorption Cross Sections from Photon Recoil in a Matter-Wave Interferometer. *Physical Review Letters* **112**, 250402 (2014). arXiv:1402.5307.

[106] Eibenberger, S., Gerlich, S., Arndt, M., Tuexen, J. & Mayor, M. Electric moments in molecule interferometry. *New Journal of Physics* **13**, 043033 (2011).

[107] Tanaka, K., Waki, H., Ido, Y., Akita, S., Yoshida, Y., Yoshida, T. & Matsuo, T. Protein and polymer analyses up tom/z 100 000 by laser ionization time-of-flight mass spectrometry. *Rapid Communications in Mass Spectrometry* **2**, 151–153 (1988).

[108] Dash, J. G. & Sommers, H. S. A High Transmission Slow Neutron Velocity Selector. *Review of Scientific Instruments* **24**, 91 (1953).

[109] Truppe, S., Juffmann, T., Geyer, P., Major, A., Ulbricht, H. & Arndt, M. Molecular lithography - A quantum optical approach. *CLEO/Europe - EQEC 2009 - European Conference on Lasers and Electro-Optics and the European Quantum Electronics Conference* (2009).

[110] Mokkapati, S. & Chennupati, J. *Wiley Encyclopedia of Electrical and Electronics Engineering, Chapter III-V* (2014).

[111] Wieman, C. E. & Hollberg, L. Using diode lasers for atomic physics. *Review of Scientific Instruments* **62**, 1–20 (1991).

[112] Ricci, L., Weidemüller, M., Esslinger, T., Hemmerich, A., Zimmermann, C., Vuletic, V., König, W. & Hänsch, T. W. A compact grating-stabilized diode laser system for atomic physics. *Optics Communications* **117**, 541–549 (1995).

[113] Pearman, C. P., Adams, C. S., Cox, S. G., Griffin, P. F., Smith, D. A. & Hughes, I. G. Polarization spectroscopy of a closed atomic transition: applica-

tions to laser frequency locking. *J. Phys. B: At. Mol. Opt. Phys* **35**, 5141–5151 (2002).

[114] Shirley, J. H. Modulation transfer processes in optical heterodyne saturation spectroscopy. *Optics Letters* **7**, 537 (1982).

[115] McCarron, D. J., King, S. A. & Cornish, S. L. Modulation transfer spectroscopy in atomic rubidium. *Measurement Science and Technology* **19**, 105601 (2008). arXiv:0805.2708.

[116] Bethlem, H., Berden, G. & Meijer, G. Decelerating Neutral Dipolar Molecules. *Physical Review Letters* **83**, 1558–1561 (1999).

[117] Wall, T. E., Kanem, J. F., Dyne, J. M., Hudson, J. J., Sauer, B. E., Hinds, E. a. & Tarbutt, M. R. Stark deceleration of CaF molecules in strong- and weak-field seeking states. *Phys. Chem. Chem. Phys.* **13**, 18991–18999 (2011). arXiv:1104.3976.

[118] Vanhaecke, N., Meier, U., Andrist, M., Meier, B. H. & Merkt, F. Multistage Zeeman deceleration of hydrogen atoms. *Physical Review A - Atomic, Molecular, and Optical Physics* **75**, 031402 (2007).

[119] van den Berg, J. E., Mathavan, S. C., Meinema, C., Nauta, J., Nijbroek, T. H., Jungmann, K., Bethlem, H. L. & Hoekstra, S. Traveling-wave deceleration of SrF molecules. *Journal of Molecular Spectroscopy* **300**, 22–25 (2014). arXiv:1402.2800.

[120] Quintero-Perez, M., Jansen, P., Wall, T. E., Van Den Berg, J. E., Hoekstra, S. & Bethlem, H. L. Static trapping of polar molecules in a traveling wave decelerator. *Physical Review Letters* **110**, 133003 (2013). arXiv:1301.2113.

[121] Chervenkov, S., Wu, X., Bayerl, J., Rohlfes, A., Gantner, T., Zeppenfeld, M. & Rempe, G. Continuous Centrifuge Decelerator for Polar Molecules. *Physical Review Letters* **112**, 013001 (2014). arXiv:1311.7119.

[122] Narevicius, E., Libson, A., Parthey, C. G., Chavez, I., Narevicius, J., Even, U. & Raizen, M. G. Stopping supersonic oxygen with a series of pulsed elec-

tromagnetic coils: A molecular coilgun. *Physical Review A* **77**, 051401 (2008). arXiv:0804.0219.

[123] Osterwalder, A., Meek, S. A., Hammer, G., Haak, H. & Meijer, G. Deceleration of neutral molecules in macroscopic traveling traps. *Physical Review A - Atomic, Molecular, and Optical Physics* **81**, 1–4 (2010). arXiv:0911.3324.

[124] Gupta, M. & Herschbach, D. A Mechanical Means to Produce Intense Beams of Slow Molecules. *The Journal of Physical Chemistry A* **103**, 10670–10673 (1999).

[125] Trottier, A., Carty, D. & Wrede, E. Photostop: Production of zero-velocity molecules by photodissociation in a molecular beam. *Molecular Physics* **109**, 725–733 (2011). arXiv:1002.3698.

[126] Chieda, M. A. & Eyler, E. E. Prospects for rapid deceleration of small molecules by optical bichromatic forces. *Physical Review A* **84**, 063401 (2011). arXiv:1108.3543.

[127] Elioff, M. S., Valentini, J. J. & Chandler, D. W. Subkelvin cooling NO molecules via "billiard-like" collisions with argon. *Science (New York, N.Y.)* **302**, 1940–1943 (2003).

[128] Breeden, T. & Metcalf, H. Stark acceleration of Rydberg atoms in inhomogeneous electric fields. *Physical Review Letters* **47**, 1726–1729 (1981).

[129] Hudson, E. R. Deceleration of continuous molecular beams. *Physical Review A* **79**, 061407 (2009). arXiv:0901.4164.

[130] Comparat, D. Molecular cooling via Sisyphus processes. *Physical Review A - Atomic, Molecular, and Optical Physics* **89**, 043410 (2014). arXiv:1404.2689v1.

[131] Riedel, J., Hoekstra, S., Jäger, W., Gilijamse, J. J., Van De Meerakker, S. Y. T. & Meijer, G. Accumulation of Stark-decelerated NH molecules in a magnetic trap. *European Physical Journal D* **65**, 161–166 (2011).

[132] Fitch, N. J. & Tarbutt, M. R. Principles and Design of a Zeeman-Sisyphus Decelerator for Molecular Beams. *ChemPhysChem* **17**, 3609–3623 (2016). arXiv:1609.05823.

[133] Norrgard, E. Magneto-Optical Trapping of Diatomic Molecules .

[134] CCD Signal to Noise Ratio. URL http://www.andor.com/learning-academy/ccd-signal-to-noise-ratio-calculating-the-snr-of-a-ccd.

[135] Truppe, S., Williams, H. J., Fitch, N. J., Hambach, M., Wall, T. E., Hinds, E. A., Sauer, B. E. & Tarbutt, M. R. An intense, cold, velocity-controlled molecular beam by frequency-chirped laser slowing. *New Journal of Physics* **19**, 022001 (2017). arXiv:1605.06055.

[136] Williams, H. J., Truppe, S., Hambach, M., Caldwell, L., Fitch, N. J., Hinds, E. A., Sauer, B. E. & Tarbutt, M. R. Characteristics of a magneto-optical trap of molecules (2017). arXiv:1706.07848.

[137] Dalibard, J. & Cohen-Tannoudji, C. Laser cooling below the Doppler limit by polarization gradients: simple theoretical models. *Journal of the Optical Society of America B* **6**, 2023 (1989).

[138] Devlin, J. A. & Tarbutt, M. R. Three-dimensional Doppler, polarization-gradient, and magneto-optical forces for atoms and molecules with dark states. *New Journal of Physics* **18**, 123017 (2016). arXiv:1608.04645.

[139] Grimm, R., Weidemüller, M. & Ovchinnikov, Y. Optical dipole trap for neutral atoms. *Adv. At. Mol. Opt. Phys.* **42**, 95 (2000). arXiv:9902072.

[140] Earnshaw, S. On the nature of the molecular forces which reg ulate the constitution of the luminiferous ether. *Trans. Camb. Phil. Soc.* **7**, 97–114 (1842).

[141] Tokunaga, S. K., Skomorowski, W., Zuchowski, P. S., Moszynski, R., Hutson, J. M., Hinds, E. A. & Tarbutt, M. R. Prospects for sympathetic cooling of molecules in electrostatic, ac and microwave traps. *European Physical Journal D* **65**, 141–149 (2011). arXiv:1012.5029.

[142] DeMille, D., Glenn, D. R. & Petricka, J. Microwave traps for cold polar molecules. *European Physical Journal D* **31**, 375–384 (2004). arXiv:0407038.

[143] J. Almond. Laser cooling of YbF molecules for an improved measurement of the electron electric dipole moment. *PhD Thesis, Imperial College London* (2017).

[144] Lu, H.-I., Rasmussen, J., Wright, M. J., Patterson, D. & Doyle, J. M. A Cold and Slow Molecular Beam. *PCCP* **13**, 18986–18990 (2011). arXiv:1104.3901.

[145] Zhang, X., Smith, K. A., Worsnop, D. R., Jimenez, J. L., Jayne, J. T., Kolb, C. E., Morris, J. & Davidovits, P. Numerical Characterization of Particle Beam Collimation: Part II Integrated Aerodynamic-LensNozzle System. *Aerosol Science and Technology* **38**, 619–638 (2004).